Evaluation of Bio-Inspired Composite Structures for Impact Materials

by
Christoffel Johannes Neethling

Thesis presented in partial fulfilment of the requirements for the degree of Master of Engineering (Mechanical) in the Faculty of Engineering at Stellenbosch University

Supervisor: Prof. Albert Groenwold
Co-supervisor: Mr Sa-aadat Parker

March 2016

DECLARATION

By submitting this thesis electronically, I declare that the entirety of the work contained therein is my own, original work, that I am the sole author thereof (save to the extent explicitly otherwise stated), that reproduction and publication thereof by Stellenbosch University will not infringe any third party rights and that I have not previously in its entirety or in part submitted it for obtaining any qualification.

ABSTRACT

Composites have been used in engineering applications for quite some time. This is in large part due to the fact that their properties can be tailored to meet requirements in a specific direction. An additional benefit of composites is that they have a high strength to weight ratio. They have been used in several types of engineering such as aerospace, marine and ground transport. However they typically have a low impact resistance which hinders their use in such environments.

Engineered ceramic-based impact resistant materials are designed to prevent penetration; however they tend to lack the ability to withstand successive blows. This is due to the brittle nature of these materials. These ceramics such as silicon carbides can withstand compressive stresses of up to 3.5 GPa. When compared to the bio-structure of a stomatopod's (mantis shrimp) club, they are inferior. The bio-structure can compressive stresses of up to 4 GPa in addition to being able to withstand thousands of high energy impacts before being replaced.

Relatively new research into the stomatopod's biological hammer's structure has revealed several strengthening characteristics that could be applicable to composite structures. Being able to take advantage of these properties with synthetic materials could provide a composite structure that has a higher impact resistance while maintaining low weight.

The primary goals of this project were to identify which strengthening characteristics of the stomatopod's bio-hammer can be applied to composites and then to test the effect these characteristics have on the impact resistance of a composite sample. The key characteristic identified for testing was that the fibre layers are helicoidal. From this it was decided that the effect of varying the offset angle between layers should be evaluated as well the effect of making the helicoidal structure continuous instead of enforcing symmetry about the mid-plane. Both characteristics were found to alter performance.

The secondary objectives for this project were as follows: Firstly, to determine whether it is possible to produce a continuous sample that is free of warpage; Secondly, to compare the failure modes of the experimental results to simulation results and Computed Tomography Scans of the samples post-failure in order to determine any key differences that influences performance and whether simulations can be used to predict performance increases based on offset angle. While the simulations slightly underestimated the performance of the samples they were able to predict performance tendencies. Additionally some internal performance altering characteristics were identified.

OPSOMMING

Saamgestelde materiale word vir ’n redelike tydperk al in ingenieurstoepassings gebruik. Dit is grotendeels as gevolg van die feit dat hulle eienskappe ontwerp kan word om aan nodige vereistes te doen in ’n spesifieke rigting. Nog ’n groot voordeel van saamgestelde materiale is dat hulle ’n baie hoë sterkte tot gewig verhouding het. Hulle word in verskeie velde van ingenieurswese gebruik byvoorbeeld lugvaart, mariene toepassings en grondvervoer. Hulle het egter tipies ’n lae impak weerstand wat hulle algemene gebruik hinder in die velde.

Bestaande keramiek gebaseerde impak bestande materiale word ontwerp om penetrasie te verhoed. Hulle het egter ’n gebrek aan die vermoë om verskeie impakte te weerstaan as gevolg van die bros natuur van die materiale. Die keramiese materiale byvoorbeeld silikonkarbiede kan drukspanning van 3.5 GPa weerstaan. Wanneer dit vergelyk word met die bio-struktuur van die stomatopod se hammer is dit inferieur. Die bio-struktuur kan drukspannings van tot en met 4 GPa weerstaan en kan boonop duisende hoë energie impakte weerstaan voor dit vervang moet word.

Relatiewe nuwe navorsing in die aard van die stomatopod se biologiese hammer se struktuur het verskeie versterkende eienskappe geïdentifiseer wat van toepassing kan wees tot saamgestelde materiale. As daar van hierdie eienskappe kan benut word met sintetiese materiale kan dit ’n saamgestelde materiaal produseer wat ’n baie hoër impak weerstand het terwyl ’n lae gewig gehandhaaf word.

Die primêre doel van hierdie projek is om te identifiseer watter versterkende eienskappe van die stomatopod se bio-hammer toegepas kan word op saamgestelde materiale. Die effek van hierdie eienskappe op die impak weerstand van die saamgestelde materiale sal dan getoets word. Die kerneienskap wat geïdentifiseer was vir toetsing is dat die fiber lae helicoïdaal is. Dit was toe besluit om die effek van die verrekenings hoek tussen die lae te wissel. Daarbenewens is daar besluit om effek te toets van die helicoïdale struktuur kontinu te maak inplaas van om simmetrie te dwing om die middel-vlak.

Die sekondêre doele van die projek was soos volg: Eerstens om te bepaal of dit moontlik is om ’n kontinue proefmonster te maak wat nie geworp is nie; Tweedens om die valings modes van die proefmonsters van die eksperimentele resultate te vergelyk met die simulasies en Berekende Tomografie skanderings na valing om te bepaal of enige spesifieke eienskappe resultate affekteer. Alhoewel die simulasies die vermoëns van die saamgestelde materiale onderskat het, was dit in staat om die neigings in die impak weerstandigheid te voorspel. Die interne werkinge van die proefmonsters het ook getoon om ’n effek te hê op impak weerstand.

TABLE OF CONTENTS

Page

LIST OF FIGURES:

1. INTRODUCTION

1.1 Project Background

Engineered ceramic-based impact resistant materials are designed to prevent penetration; however they tend to lack the ability to withstand repeated collisions. This is due to their brittle nature. These ceramics such as silicon carbides can withstand compressive stresses of up to 3.5 GPa. The bio-structure of a stomatopod's (mantis shrimp) club can withstand higher compressive stresses of up to 4 GPa in addition to being able to tolerate thousands of high energy impacts without failing. [1] [2] [3] [4]

1.2 Project Motivation

Multi-layered composites have seen an increase in variety industries in aerospace, terrestrial and marine transport. The properties that make composites useful in these industries are that they are lightweight, have a high stiffness, high static strength and can be custom made for use. They do however suffer from having a low impact resistance. For use in armour a high impact resistance is a necessity in order to prevent catastrophic material failure. For this purpose a new class of composites have emerged in order to satisfy the need that consists of Kevlar composite impact surface with a carbon fibre inner surface in order to stiffen the structure. Most of these composites are of the sandwich design with the same material on both of the surfaces. [5]

Relatively new research into the stomatopod's biological hammer's structure has revealed several strengthening characteristics that could be applicable to composite structures. Being able to exploit these properties with synthetic materials could provide a composite structure that has a much higher impact resistance while maintaining a low weight. The most obvious benefit of this would be to create lighter body armour for infantry, which in turn will make them more mobile and thus increase their survivability. Other potential applications may vary depending on the results obtained during the course of the project.

1.3 Problem Statement

Current impact resistant materials can only withstand a few blows before failing, making them expensive to use. Additionally, since they are used in high energy conditions, material failure under load usually has drastic consequences.

1.4 Project Objectives

The project will attempt to meet the following objectives by testing the helicoidal structure seen in the orientation of the chitin fibres using synthetic materials. Note optimal in the following context means highest impact resistance.

1.4.1 Primary Objectives

The primary goals of this project are to identify which strengthening characteristics of the stomatopod's bio-hammer can be applied to composites and then to test the effect these characteristics have on the impact resistance of a composite sample. The key characteristic identified for testing was that the fibre orientations are helicoidal. From this it was decided that the effect of varying the offset angle between layers should be evaluated as well the effect of making the helicoidal structure continuous instead of enforcing symmetry about the mid-plane. The material used is a carbon fibre reinforced composite.

1.4.2 Secondary Objectives

The secondary objectives for this project were as follows: Firstly, to determine whether it is possible to produce a continuous sample that is free of warpage; Secondly, to compare the failure modes of the experimental results to simulation results and CT scans of the samples post-failure in order to determine any key differences that influences performance.

1.5 Study Approach and Methodology

A literature study on the structure of the stomatopod's biological hammer was done in order to determine what factors improve its strength and which of those factors can be tested experimentally and included in the project. The literature study also includes work that has been done in the bio-inspired structures field of material science. Additionally the student needed to upgrade the original laboratory equipment by designing a test rig that is in accordance with an ASTM testing standard. The experiments consisted out of drop-weight tests which were designed to ensure complete sample failure in order to capture the entire impact response. The impact response forces were recorded and processed in order to determine the energy absorbed for each sample.

Results of the experiments were compared to those of the simulations in order to determine whether simulations can be used to predict the effect of varying the offset angle and the difference between continuous vs. symmetrical samples. The failure modes of the experimental results were compared to the results obtained from the CT scans of the samples post-failure in order to evaluate the difference between the visible and non-visible damage. The failure modes of the simulation results were compared to the results obtained from the CT scans of the samples

post-failure in order to determine whether the simulations can be used to predict the change in failure modes based on the offset angle and whether the sample is continuous or symmetrical. The simulation software that was used is LS-DYNA.

1.6 Project Scope and Limitations

The scope of this project will be limited to testing characteristics of the stomatopod's biological hammer's structure that can be tested with existing laboratory equipment. Thus the effect the striated region has on the structure will not be addressed in this project. Additionally all results that are obtained can only be used comparatively with other materials tested on the same setup.

2. LITERATURE STUDY

This chapter covers the relevant strengthening characteristics of the stomatopod's biological hammer and some work done on helicoidal composites.

2.1 Biological Hammer

Mantis shrimps, also known as stomatopods, are a type of predatory crustacean. They are highly aggressive and have a second pair of modified thoracic appendages that are structurally adapted for close-range combat. The type of modifications divide them into two distinctive groups which are spear-like that impales their prey and hammer-like that crushes their prey. [6] This study will focus on the characteristics of the hammer-like group. Since the mantis shrimp typically feeds on other crustaceans with mineralized biological structures which are tough and damage tolerant, the hammer structure must not only be able to exceed the force required to break the shell, it must be able to survive the impact repeatedly.

Studies into the characteristics of the clubs have shown that they are capable of sustaining incredible accelerations of up to 10 400g and speeds of 23m/s from a stationary position. Blows can generate instantaneous forces larger than 700 N during impact, yet the clubs can withstand thousands of these blows before being replaced during moulting process. [2] [3]

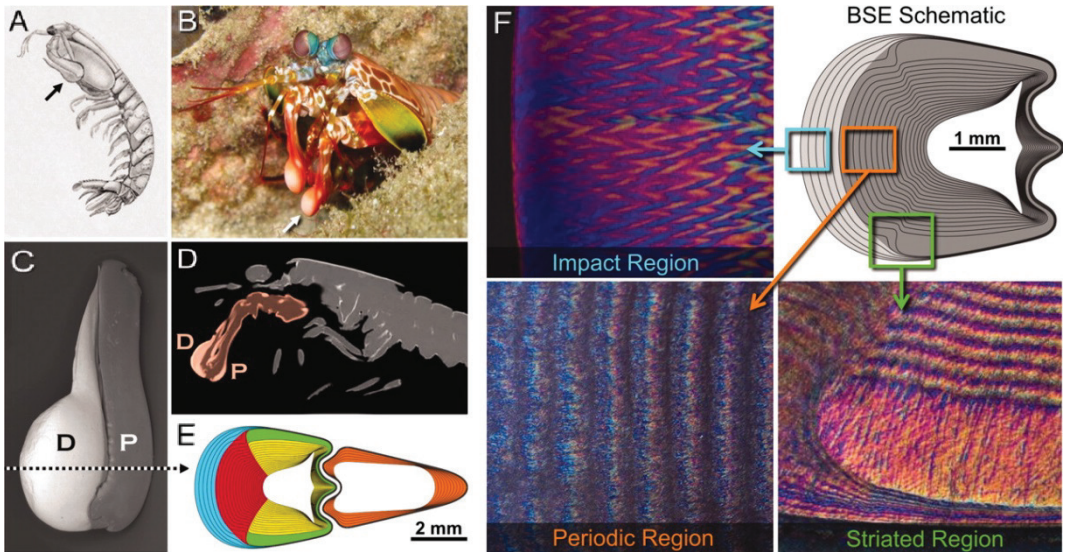

Figure 1: A-B: Images of Stomatopod, C-E: Biological Hammer, F: Impact, Periodic, Striated Regions [2]

Figure 1A illustrates the body of a mantis shrimp. Figure 1B is a magnified view of a mantis shrimp that clearly shows the striking appendages. Figures 1C, which was taken with an electron micrograph, and 1D, which is a microcomputed tomographic section, are cross-sections of the biological hammer. As can be seen in Figure 1E above, the impact is on the club is in the direction P indicated by the arrow. Further from 1F, which are optical micrographs, it can be seen that the club is composed of three separate regions. These are namely the impact region, the periodic region and the striated region. Their differences in material properties can be mostly attributed to the mineral content found within them. As seen in Figure 3, calcium and phosphor concentrations are highest and magnesium at its lowest within the impact region. In the periodic region however these values change with calcium concentrations falling with a step-like fashion, phosphor in a gradient-like fashion while magnesium rises as the regions cross over. Thus there is a clear correlation between the mineral content and the hardness of the layers when this data is compared to that of Figure 2. From these values three regions can be identified in terms of their hardness namely, the outermost impact region with a modulus value of up to 70 GPa for both dry and hydrated conditions, a transitional region within the impact region is characterized by a sharp decrease in modulus values that go up to 45 GPa and 35 GPa for dry and hydrated conditions respectively and the periodic region with modulus values that oscillate between 25 GPa and 10 GPa for dry conditions and 8 GPa to 3 GPa for hydrated conditions. It is important to note that the outermost impact region is approximately only 50 µm to 70 µm thick. [2]

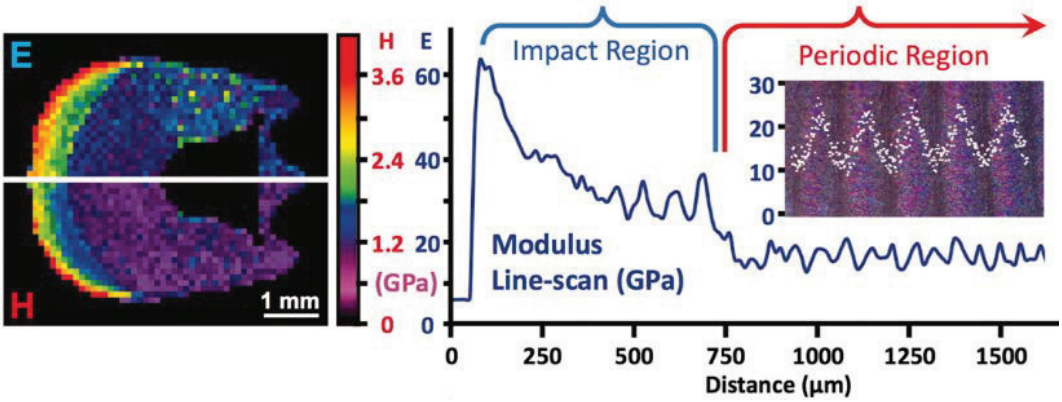

Figure 2: Stress Concentrations and Elastic Modulus Values vs. Distance from Impact Location [2]

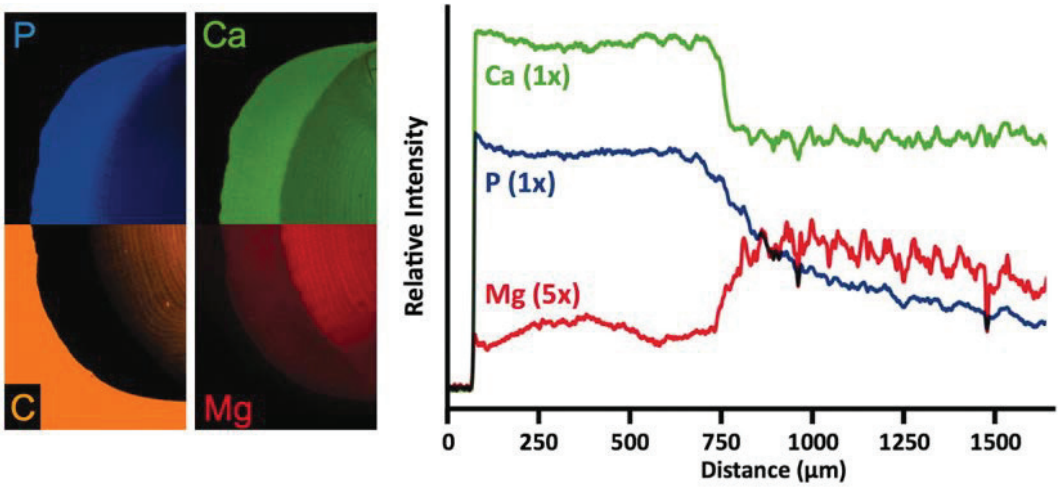

Figure 3: Mineral Concentrations vs. Distance from Impact Location [2]

The important structural characteristics to draw from this information are that there are three regions in the club with reducing modulus values and varying mineral compositions and that these regions increase in thickness as distance from the impact region increases.

All of the regions of the club are however consists of a chitin helicoidal organic matrix as seen in Figure 4. The matrix consists out of sheets of parallel fibres that are stacked with each layer's angle slightly rotated from the previous on a periodic basis. These periodic stacks are referred to as superlayers, which decrease linearly in thickness from the exterior to the interior of the club. The helicoidal structure causes the cracks due to impacts to propagate with a rotating crack front parallel to the fibres in the layers without causing the fibres to be severed. This, in turn, causes the cracks to have a relatively large surface area per unit length, which enhances energy dissipation during crack propagation. However if a crack does not have a rotating front, but travels straight, it is inhibited by the oscillating elastic modulus values in the region. As demonstrated by Fratzl et al. oscillation of the elastic modulus value provides additional damage resistance [7]. As a result most of the cracks are contained volumetrically within the periodic region of the club.

Another mechanism that the found within the club that improves impact resistance is the elastic modulus mismatch within the impact region. A crack originating from a material with a lower modulus of elasticity can either reflect at the interface or continue through to the material with the higher modulus value. This effect is governed by Dundurs' parameter and the ratio of the fracture toughness of the interface (G_{IF}) vs. the fracture toughness of the stiff material (G_{C1}). The Dundur parameter is calculated as shown below in equation 1: [8]

$$\alpha = \frac{E_1 - E_2}{E_1 + E_2} \quad (1)$$

where:

α is the Dundurs' parameter,
E_1 is the modulus of elasticity of the stiffer material
E_2 is the modulus of elasticity of the more compliant material.

The G_{IF}/G_{C1} ratio is then plotted against α in order to yield a critical curve. At the interface within the impact region just beneath the impact surface, the α value is approximately 0.33 with a corresponding critical G_{IF}/G_{C1} value of approximately 0.35. Thus if the fracture toughness of the interface is less than 35% of the stiffer, outer material crack deflection will take place, in effect containing the crack within the periodic region. If the interface fracture toughness is more than 35% of the stiffer material the crack will propagate through to the hard outer shell, which would be severely detrimental to structural integrity. As mentioned earlier studies have shown that cracks are in fact mostly contained within the periodic region, but there is also evidence that crack deflection takes place within the impact region at the interface with the outer shell. Thus the toughness ratio found in the club's impact region is sufficient to prevent cracks from reaching the hard outer surface.

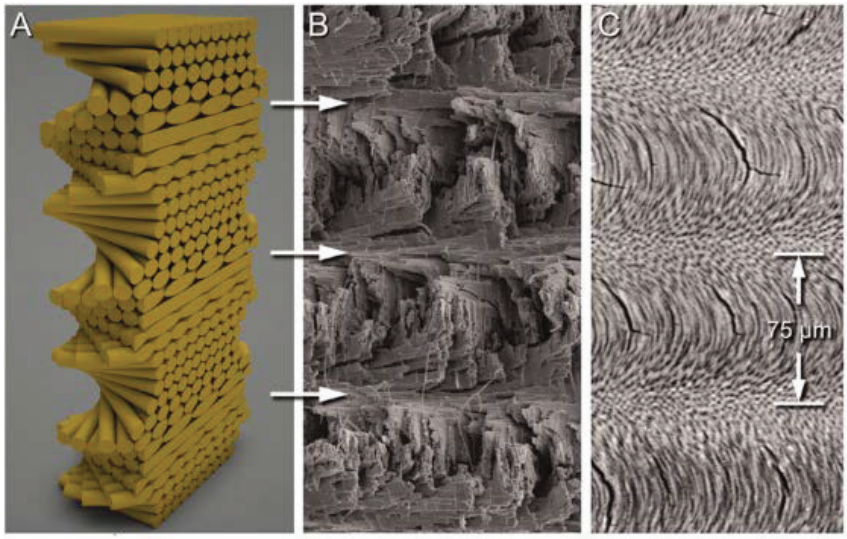

Figure 4: A: Graphical Representation of a Helicoidal Structure, B: SEM-Fractograph, C: Polished surface of a Cross-section [2]

2.2 Composite Materials

2.2.1 Overview of Composites

Four basic groups make up structural materials namely polymers, metals, ceramics and composites. The defining characteristic of composites is that they are composed of two or more materials with different properties into a single structural unit. The structural material then exhibits material properties different from the original materials.

Initially composite structures were simply macroscopic with slabs of material being bonded to each other. However with advancements in technology over the decades and the emergence of nanotechnology, composite materials have been revolutionised. By using nanofibres, nanotubes and nanoparticles researchers were able to work with the microstructure of composite materials and thus refine the material properties much further.

Ashby [9] discussed how the decrease in use of metal is due to the rise in use of composites, ceramics and polymers. This is because they tend to be lighter and cheaper than most metals which is driving the industry to find new ways for using the former three where metals had been used. Within the composites category, the most commonly used type is a matrix or epoxy material that is reinforced with fibre. Fibres can be substituted with flake or particle reinforcing materials; however they do not exhibit the same level of reinforcing properties.

It was demonstrated by Griffith [10] that when some materials are in fibre form they have increased stiffness and strength than when compared to their bulk form. He did this by testing the tensile strength of glass in both fibre and rod form in varying diameters. He discovered that as the diameter of the fibres and rods decreased, the tensile strength increased as seen in Figure 5. This effect is caused by the fact that the reduced diameter reduces the likelihood of surface cracks that could cause failure. Researchers have applied similar tests to a large range of other materials and have been met with similar results. However the reasons for these properties are not necessarily the same for other materials. An example of this is polymeric fibres that have this property because the fibres have highly aligned polymer chains whereas the bulk form is random. Another example occurs in crystalline structures, a solid polycrystalline structure has a higher dislocation density than a single crystal. Thus the same material can demonstrate different strength properties when the single-crystal form is compared to the polycrystalline form. Up until the development of nanotechnology, single-crystal materials were considered to be the stiffest and strongest materials available. However since then they have been replaced by carbon nanotubes with this regard. [11][12]

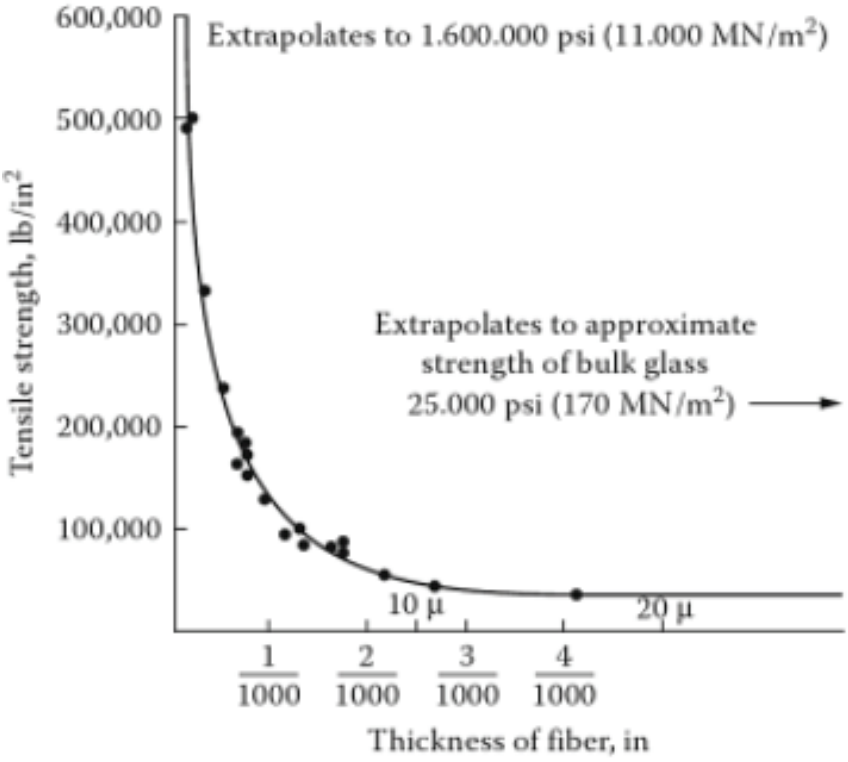

Figure 5: Tensile Strength vs. Fibre Thickness [13]

It is clear that utilising the fibre form of a material allows the user to obtain the maximum tensile strength and stiffness from the material. However, making use of composites does have some limiting drawbacks. They cannot support compressive loading in the longitudinal direction nor are their transverse properties of the same standard as their longitudinal mechanical properties. Thus fibres are always used with some form of matrix material or binder in order to hold them together in a structural form. The matrix material also serves the secondary purpose of shielding the fibres from damage due to external sources. Additionally filler material can be used in composites and are indeed quite common. Their functions range from cost and weight reduction, smoke and flame suppression to protection against ultra violet degradation. [14]

Fibre orientations can be used in order to provide transverse reinforcement by adjusting them to manage the stress field in the composite. The need to address different stress fields has led to various types of fibre alignments and as such various composite types. In Figure 6A an example is shown of a continuous fibre composite. They are made by manipulating individual continuous fibre/matrix laminae into the necessary orientations and are then subjected to bonding conditions until the laminate is set. Although this composite is in common use it is plagued by the risk of delamination due to the matrix properties dominating the interlaminar strength. Woven fibre composite as, as seen in Figure 6B, have reduced stiffness and strength due to fibres being less aligned as in the continuous fibre composites. However they exhibited a much higher resistance to

delamination. Chopped fibre composites, as seen in Figure 6C, have short fibres distributed haphazardly within the matrix material. Although their properties are significantly poorer than those of continuous fibre composites, they are widely used in high quantity production due to their low cost. Hybrid composites, as seen in Figure 6D, can be a mix of continuous and chopped or a mix of different types of fibre materials such as carbon and glass. Another widely used type of composite is the sandwich layup, an example of which can be seen in Figure 7. Sandwich layups have the benefit of having very large stiffness-to-weight ratio and as such are extensively used in the aerospace industry. [14]

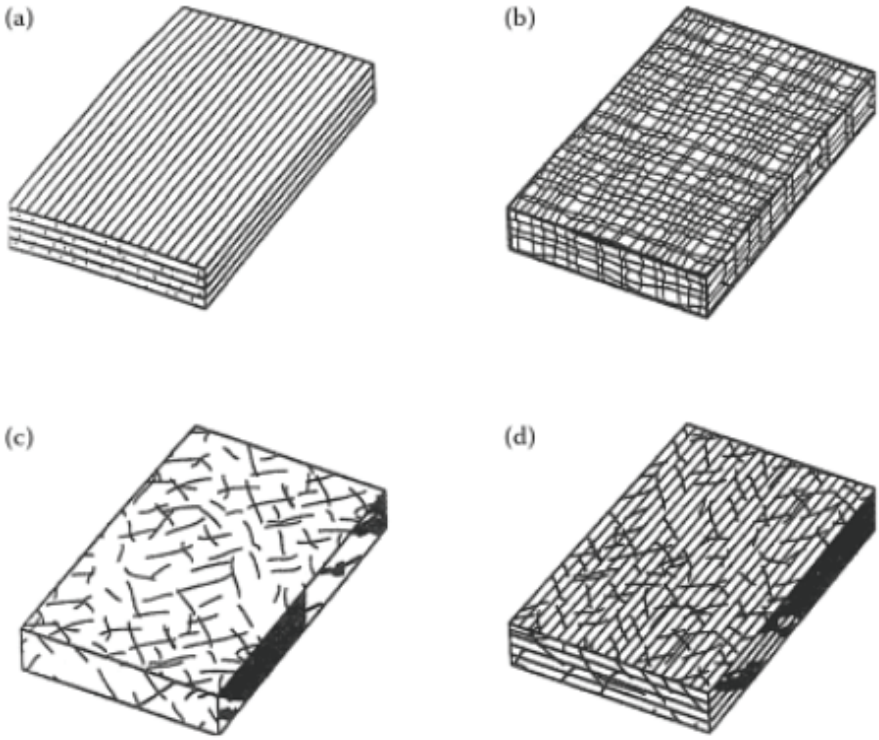

Figure 6: A: Continuous Fibre Composite, B: Woven Composite, C: Chopped Fibre Composite, D: Hybrid Composite [14]

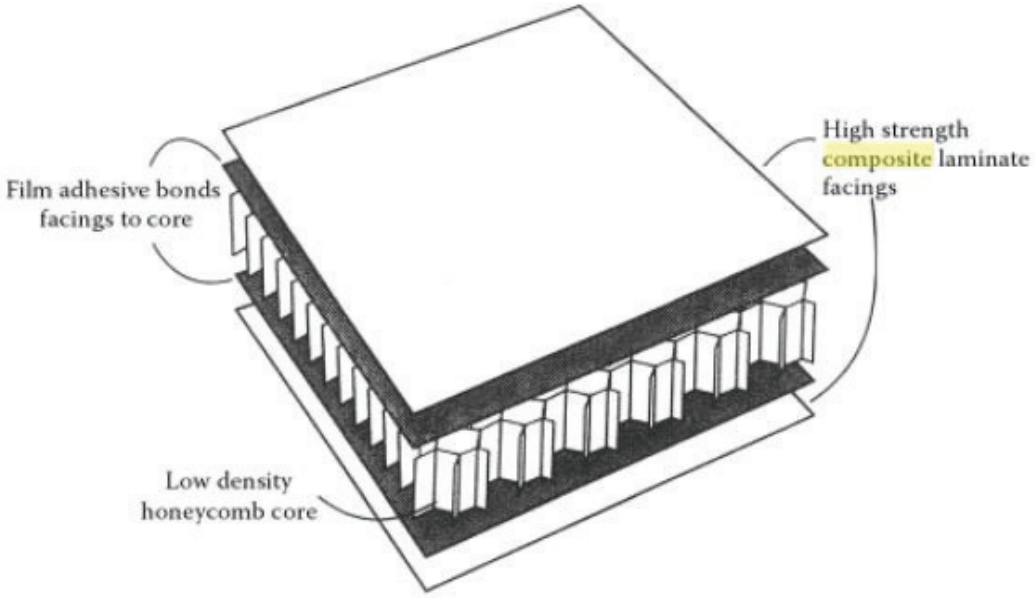

Figure 7: Sandwich Composite Layup [14]

Carbon composites, such as the ones used in this project, typically have their stiffness defined in the warp and weft directions. The warp defines the primary direction of the fibres which is also referred to as the 0° axis. The weft is defined to be perpendicular to the to the primary fibre orientation which also referred to as the 90° direction.

2.2.2 Fibre Composites Mechanics [15]

While the laminate is under tensile loading in the direction of the fibres, the fibres carry the bulk of the load due being much stiffer than the matrix material. During compressive loading the matrix carries the bulk of the load by binding the fibres which would otherwise buckle much more easily. During loads applied in the transverse and out of plane directions the load is distributed across the fibres and matrix material.

For a unidirectional sample during tensile loading, damage to the matrix material has a small effect on the stiffness due to the fibres carrying the bulk of the load. However undamaged fibres that straighten due to the tensile load may aggravate matrix material damage. Damage to the matrix material severely compromises the ability of the laminate to withstand compressive loads due to the matrix being the principle source of stiffness. When the compressive load is in the fibre direction the kinking and buckling will also cause further matrix damage. However the bonding areas between the fibres and matrix material are usually weaker than the components and tend to become pathways for crack propagation.

The above mentioned material damage characteristics are inherently difficult to incorporate into a material model. [16] Thus in order to create viable solutions the following assumptions was made for models capable of representing damage. [15]

- In order to maintain the orthotropic nature of the laminate during damage, defects are handled as disk shaped cracks running perpendicular and tangential to the fibres.
- For the model, linear elasticity is assumed to hold if the state of defects do not change. However the stress-strain response from experimental data is typically highly non-linear. The implication of this is that since the laminate remains linear initially before damage all of the non-linear effects are caused by damage to the sample.

There are four modes of failure for fibre-epoxy based composite materials. The first mode is the fibre rupturing mode. This is caused by tensile stress in the σ_{11} direction which is the fibre direction. As mentioned earlier the fibres carry the most of the load in this direction and thus the tensile strength X_t is predominantly fibre dependant. It is however a function of the fibre/matrix ratio within the sample. This failure mode is characterised by a groups of fibres failing and debonding from the matrix material which creates voids between fibres. It is possible, depending on the level of strain, that the matrix material is still intact in these regions despite the fibres failing. This is due to the matrix material being able to withstand higher levels of strain than the fibres.

The second mode of failure is the fibre buckling and kinking mode. This mode of failure occurs when a compressive load is applied to the laminate in the σ_{11} direction. This mode of failure is characterised by matrix failure and is typically initiated by the failure of a single fibre which allows matrix damage to propagate. The compressive strength X_c is determined by the compressive strength of the fibres and the matrix material as well as the shear strength and elastic stiffness of the matrix material.

The third failure mode is matrix cracking during tensile loading in the transverse or shear directions. This failure mode is typically governed by the shear and tensile strengths of the matrix material.

The fourth failure mode is matrix cracking during compressive loading in the transverse or shear directions. This failure mode is also typically governed by the shear and tensile strengths of the matrix material.

An additional failure mode is delamination. Delamination is characterised by the individual laminas within the laminate separating from each other. Delamination drastically compromises the strength of the sample but it often not visible on the outside surface. Advanced scanning methods can be used to evaluate a sample for delamination.

2.2.3 Failure Criteria for Composites

Composite materials has several failure criteria which can be categorised into in-plane and delamination failure criteria

2.2.3.1 In-plane Failure

In-plane failure denotes the damage sustained to the laminate's fibres or matrix material due to pure in-plane tensile, compressive or shear loads. The failure criteria for in-plane failure can be categorised into two groups. The first group treats all of the failure modes together and the second group handles them separately.

An example of the first group is the Tsai-Hill failure criteria where they attempt to quantify all of the failure modes into a single formula as seen in equation (1): [17]

$$\frac{\sigma_{11}^2}{X^2} - \frac{\sigma_{11}\sigma_{22}}{X^2} + \frac{\sigma_{22}^2}{Y^2} + \frac{\tau_{12}^2}{S^2} \geq \mathbf{1} \tag{1}$$

where:

σ_{11} = longitudinal stress
σ_{22} transverse stress
τ_{12} = shear stress
X = longitudinal strength
Y = transverse strength
S = shear strength.

An example of the second group is the Hashin criteria which formulate separate modes of failure for tension, compression, fibre and matrix failure. Specifically the 2D-Hashin criteria for example separate them into four modes as seen in equations (2)-(5). [18]

Tensile fibre failure ($\sigma_{11}>0$)

$$\left(\frac{\sigma_{11}}{X_T}\right)^2 + \left(\frac{\tau_{12}}{S_{12}}\right)^2 = \mathbf{1} \tag{2}$$

Compressive Fibre Failure ($\sigma_{11}<0$)

$$\frac{|\sigma_{11}|}{X_c} = \mathbf{1} \tag{3}$$

Tensile matrix failure ($\sigma_{22}>0$)

$$\left(\frac{\sigma_{22}}{Y_T}\right)^2 + \left(\frac{\tau_{12}}{S_{12}}\right)^2 = \mathbf{1} \tag{4}$$

Compressive matrix failure ($\sigma_{22} < 0$)

$$\left(\frac{\sigma_{22}}{2S_{23}}\right)^2 + \left[\left(\frac{Y_c}{2S_{23}}\right)^2 - 1\right]\frac{\sigma_{22}}{Y_c} + \left(\frac{\tau_{12}}{S_{12}}\right)^2 = 1 \quad (5)$$

The advantage of this group of failure criteria is that they tend to consider interlaminar stresses which in turn yield a more accurate result.

2.2.3.2 Delamination Failure

As mentioned earlier, delamination severely compromises the structural integrity of a laminate. Energy and stress based theories have both been developed for evaluating delamination. However this section will focus more on the stress based theories.

An example of the energy based models is the Bending Strain Energy Density model which is based on the failure mechanics of a simply supported beam during pure bending. This method is useful in two dimensional analyses due to absence of the stress term in the normal direction. [19]

An example of the stress based theories is the Brewer and Lagace method which takes into account normal and shear stresses in the laminate as seen in equation (6): [20]

$$\left(\frac{\sigma_{33}}{Z_T}\right)^2 + \left(\frac{\sigma_{23}}{S_{23}}\right)^2 + \left(\frac{\sigma_{31}}{S_{31}}\right)^2 = 1 \quad (6)$$

Where:

σ_{33} = through thickness stress,
Z_T = through thickness tensile strength.

Additionally Zhang determined a way to estimate whether failure will occur based on delamination based on equations (7) and (8).[21]

$$\sqrt{\tau_{13}^2 + \tau_{23}^2} \geq \textbf{Interlaminar Shear Strength} \quad (7)$$

$$\sigma_{peel} > Z_T \quad (8)$$

where:

σ_{peel} = stress required for layers to peel off.

2.2.4 Damage Characterisation

The damage types according to which the samples are to be sorted can be classified as externally visible and internal types, as can be seen in Figure 8. The externally visible types include: dents/depressions, splits/cracks, combined splits and delamination and combined large cracks with fibre breakage and

indentation/puncture. Internal damage types consist of delamination and splits/cracks. However since the experiments were designed to ensure complete sample failure all of the samples displayed large cracks combined with fibre breakage caused by puncture. As can be seen in Figure 9 the damage can also further be quantified by the maximum diameter of the damaged area.

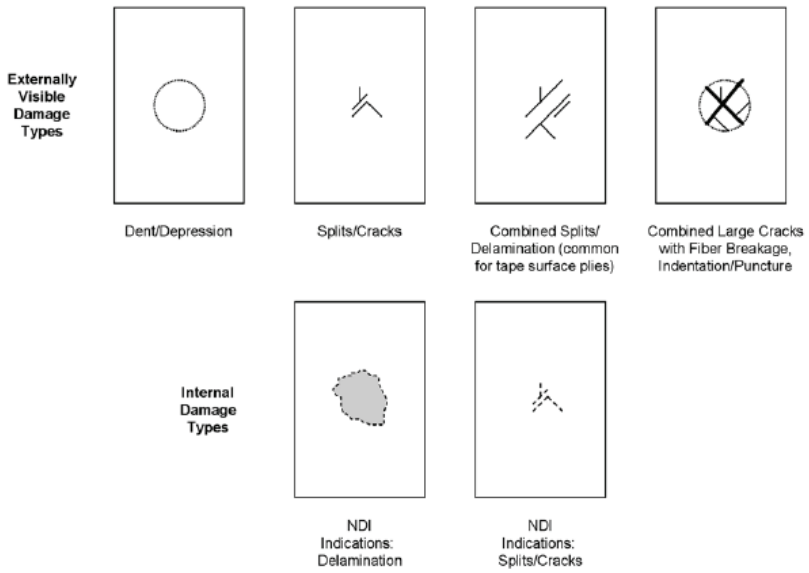

Figure 8: Potential Damage Types [30]

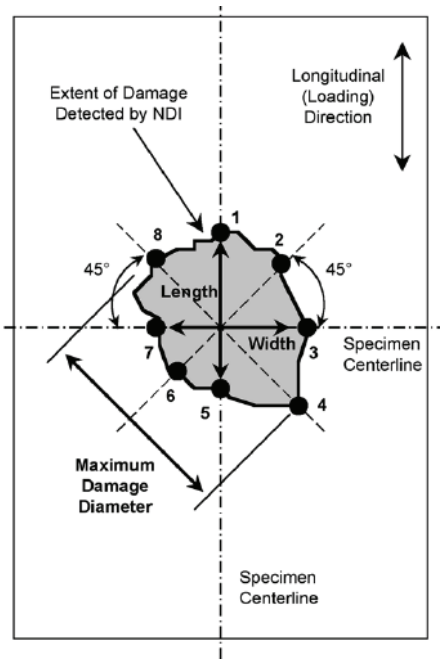

Figure 9: Analysis of Example Damage [30]

There is another testing setup that makes use of a square sample secured with a round clamp which produces slightly different sample damage. An example of this can be seen in the work done by Sevkat et al. as seen in Figure 10. [22]

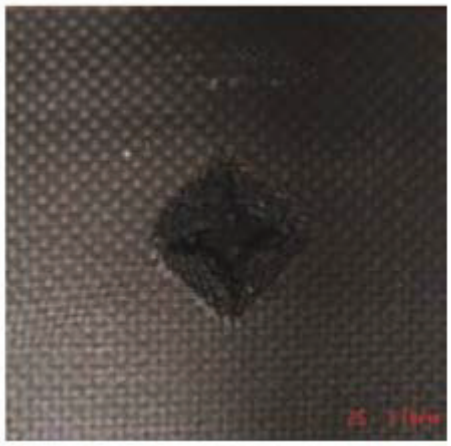

Figure 10: Post-Impact Photo of Backside of Square Sample [36]

Although numerous papers have been published on the topic of low velocity impact response of composite materials, the vast majority of them utilise impact energies of less than 40J with some going to 80J. Due to the large difference in impact energy the impact response from these papers could not be compared to those in this project. [23] [24] [25] [26]

2.2.4 Helicoidal composites

In a study performed by Apichattrabrut and Ravi-Chandar, helicoidal composites were compared to unidirectional composites with regards to debonding resistance, damage tolerance and penetration resistance. It was tested by methods of tensile test, a circular plate load test and impact testing. The testing was done with carbon fibre/epoxy matrix composites that were 40 layers thick. The stacking sequence of the helicoidal composites was: $[180/170/160/150/140/130/120/110/100/90/80/70/60/50/40/30/20/10/0/0]_S$. This angle displacement of 10 degrees is taken from naturally occurring helicoidal structures, although the paper does not disclose which one. The above mentioned sequence can be seen in Figure 5. [5]

The manufacturing process the researchers used was a standard hand lay-up and vacuum process cured in an autoclave. Curing was done according to manufacturer specifications. They also discovered that a very good alignment was necessary in order to ensure that the potential benefits of a helicoidal structure would not be compromised. In this case an accuracy of $\pm 2^{o}$ was required.

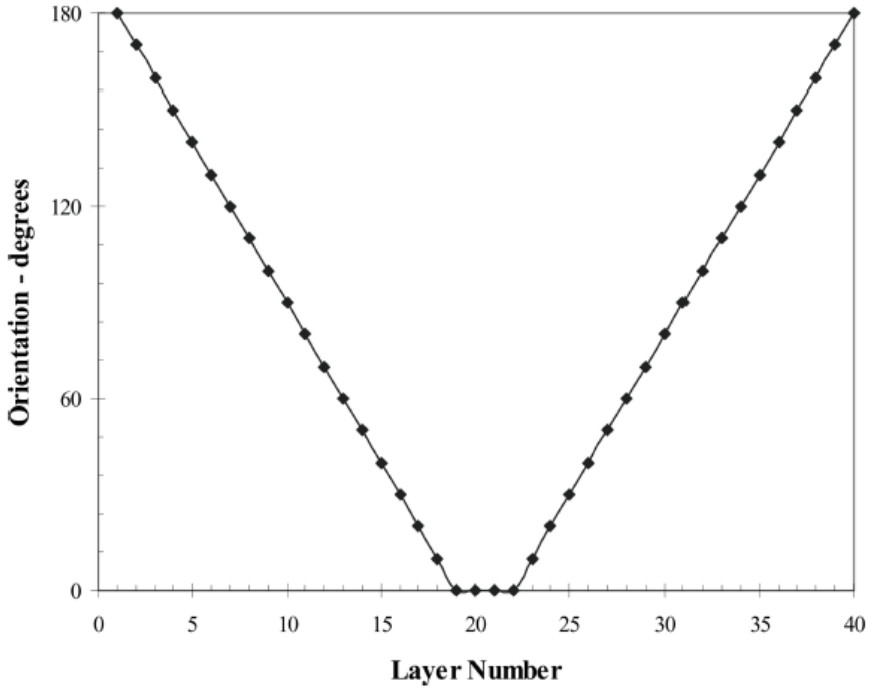

Figure 11: Orientation Angles of Layers in Helicoidal Composites [5]

The researchers discovered that the helicoidal specimens had a higher damage tolerance as well as a higher debonding resistance. The tensile test revealed that that the helicoidal structure is improves energy absorption due to the better containment of transverse cracks. The helicoidal composites were capable of sustaining higher loads than the unidirectional composites. They also exhibited the highest penetration resistance.

The researchers also reinforced some of the composites with stainless steel staples, with the staples being inserted prior to curing as seen in Figure 9. The reinforced composites exhibited improved delamination resistance and carrying capacity as well as not failing catastrophically as soon as the first damage occurs.

Thus the helicoidal structure composites surpassed unidirectional composites on the entire test series that were performed, clearly proving that they are superior.

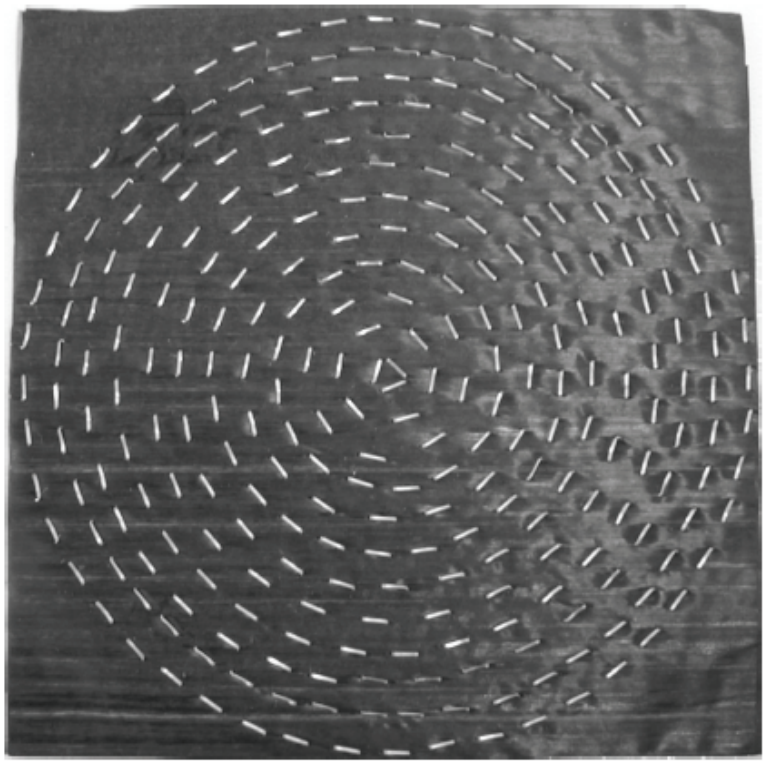

Figure 12: Staple Reinforced Composite Layup

2.3 Modelling

Numerical modelling was used in this project in order to determine whether it is possible to predict the experimental results and to provide some understanding of the results. The modelling technique used was Finite Element Method (FEM).

2.3.1 Principles of Modelling

FEM is a method used in order to solve field problems, such as deformation of a structure under load or temperature distribution in a component. These field problems can be represented mathematically by differential equations or integral statements. FEM programs such as Nastran, Dytran or LS-DYNA contain several ready-to-use Finite Element (FE) formulations which make them easy to use. The problem with FEM software being easy to use is that someone with very limited knowledge of the method can obtain feasible looking results that are not necessarily accurate.

For a FEM analysis the structure under evaluation is broken up into smaller components, also known as elements. These elements are connected at nodes and combined they form the finite element structure of the component. The way the elements fit together is referred to as the mesh of the structure. The FE mesh is what generates the field problem to be solved with the unknown values at the nodes. The FEM software then solves the field problem element by element. It is

important to note that FEM is only perfectly accurate when the problem is very trivial in which case a hand calculation would probably be better.

Another factor to take into consideration is discretization. Discretization is the process of dividing the mathematical model that was established into a mesh of smaller finite elements. Representing a continuous field by using a discrete field obviously also introduces an approximation. Thus FEM in general is only an approximation that increases in accuracy as the resolution of the mesh is refined.

There are several benefits to using FEM as opposed to other types of numerical analysis techniques. These are: [27]

- FEM is universally applicable to all types of field problems. These include component stress, heat transfer, magnetic fields etc.
- The structure being modelled can assume any shape, the user only needs to ensure the mesh is fine enough to properly analyse the component.
- Any boundary condition and/or load can be applied to any node.
- Material properties are not constrained to be isotropic.
- Different types of components can be combined even though they have different mathematical descriptions.
- A properly defined FEM model is a good approximation of the actual body.
- Accuracy can be regionally scaled by refining the mesh at specific areas of interest in order to improve the approximation.

There are however several disadvantages to using FEM. These are: [27]

- As mentioned earlier, FEM is an approximate solution.
- Heavily depends on the quality of the elements for the quality of the answer.
- Errors in input data are not necessarily discovered.

In order to start the FE analysis of a problem, the problem first needs to be classified. This is done be evaluating the nature of the problem with regards to dominant phenomena, time-dependency, linearity, type of results desired, level of accuracy required, etc. The answers to these questions determine the amount of information needed as well as the method of analysis required.

The next step in FEM is to build a model of the problem. This is done by first understanding the actual problem and then recreating it, mathematically. However the recreated version is stripped of all information that is not important to the result. This simplifies the model while retaining all of the important information, which allows the problem to be evaluated more easily while maintaining a high level of accuracy. Thus a component is broken down into a geometric model with boundary conditions, material properties etc. which is then described by a mathematical model. The mathematical model is then analysed and simulated in order to determine the behaviour of the actual component. This again stresses the importance of a good mathematical model.

Before the full FE analysis is performed however a preliminary analysis should first be done. This analysis can be an experiment, established formulas or hand calculations. This evaluation could help to improve the mathematical model before a lot of time is spent on it during simulation. Additionally it can be used to great effect in answer verification since it should correspond to the answer obtained from the FE analysis.

The actual use of FEM software typically requires pre-processing, numerical analysis and post-processing. Pre-processing is essentially the implementation of the mathematical model into the software. Numerical analysis is the phase where the software solves the matrices that are generated by the implemented model. It should be noted that time-dependant problems require significantly more calculations than time-independent problems. Post-processing is when the FEM software interprets the results obtained from the numerical analysis into graphical information for the user.

Following the execution of the FEM software the results have to be checked to see if they are accurate. The first check is typically referred to as the sanity-check which is to see if the results make sense and are not obviously wrong. Secondly the results are compared to the preliminary analysis to check for correspondence. The preliminary analysis consists of testing the most basic version of the system and comparing it to the simulation results. If errors are detected, the model should be adjusted and analysed again. [27]

The simulation was designed with a low impact velocity damage modelling approach. These can be categorised into four main groups namely: fracture mechanics, failure criteria, damage mechanics or yield surface approach. [28]

Fracture mechanics is relatively accurate at simulating matrix damage and delamination; however, it is difficult to model progressive failure using this approach. Failure criteria are typically used only in static load cases. They can be categorised into the group that handles all of the failure mechanisms at once, like Tsai-Wu, and the group that treats each mechanism separately. Damage mechanics scales the constitutive model instead of making use of specific cracks in the laminate. When used to simulate composite damage it has shown generally good results. There have been some proposals using the yield surface approach but they have not been widely implemented into FE codes. [28][29]

3. EXPERIMENTAL PROCEDURE AND EQUIPMENT

This chapter will explain the equipment used for the experiments as well as the experimental procedure used in order to obtain experimental results.

3.1 Testing Standard

For this project the testing standard D7136/D 7136M-05: "*Standard Test Method for Measuring the Damage Resistance of a Fibre –Reinforced Polymer Matrix Composite to a Drop-Weight Impact Event*" of ASTM International will be used. The primary scope of the standard is as follows: "*This test method covers the damage resistance of multidirectional polymer matrix composite laminated plates subject to a drop-weight impact event. The composite material forms are limited to continuous-fibre reinforced polymer matrix composites, with the range of acceptable test laminates and thicknesses.*" [30]

The standard prescribes that a rectangular composite specimen is to be clamped to a supporting plate with a rectangular hole for the specimen to expand into. Using a drop-weight mechanism the specimen is to be subjected to an impact with a hemispherical impactor perpendicular to its plane. The resulting damage is then analysed in terms of size and type in order to determine the damage resistance of the specimen. The impact force was also measured over time in order to calculate the energy absorbed. There are several factors that influence the quantifiable damage resistance of the specimens namely, impact force, boundary conditions, impact energy, impactor geometry, specimen geometry, impactor mass and the layup of the specimen itself. Thus results obtained on one setup are typically not scalable to another due to the high level of influence of these factors. [30]

3.2 Experimental Equipment

This section discusses the all of the equipment used in the experimental setup as well as how the differ from the testing standard.

3.2.1 Impact Fixture

This section specifically covers all of the components involved with the actual impact of the experiment. This includes the support fixture, the impactor, the trolley, and the clamping mechanism.

Figure 13: Support Fixture Secured to Load Cell

The supporting baseplate of the support fixture is bolted to the load cell as seen in Figure 10. This is done in order to reduce resonance vibrations.

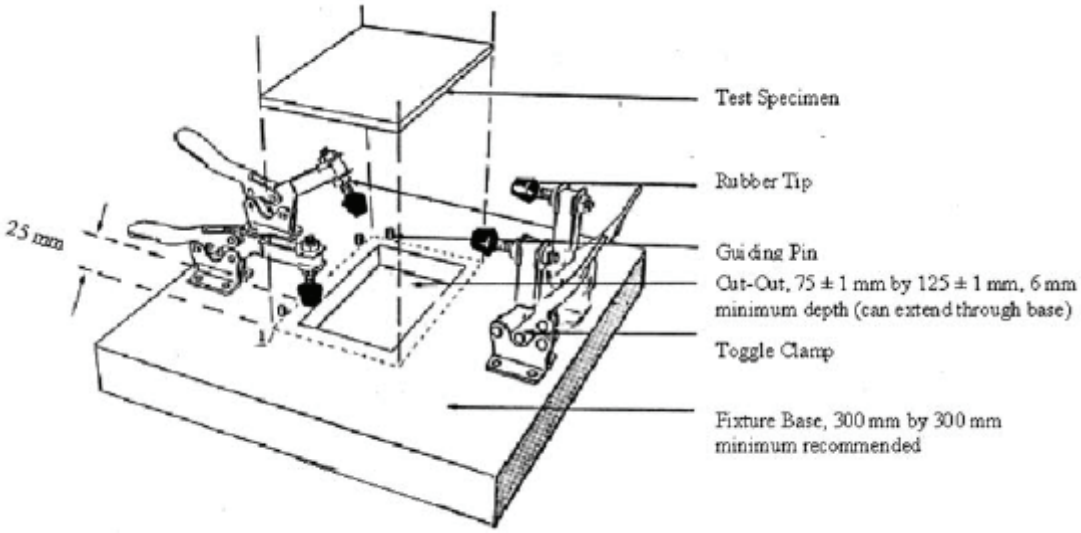

Figure 14: Illustration of Fixture Base [30]

The illustration in Figure 11 depicts an example of the clamping mechanism required in order to keep the sample in place during impact. However a bolting clamp mechanism was designed and implemented for securing the sample as seen in Figure 12. The design of the bolted clamp system can be seen in Appendix A.2 and A.3. This was done in order to have a much flatter surface protruding above the sample to prevent interference with the trolley which has a broad surface as seen in Figure 17 on page 24.

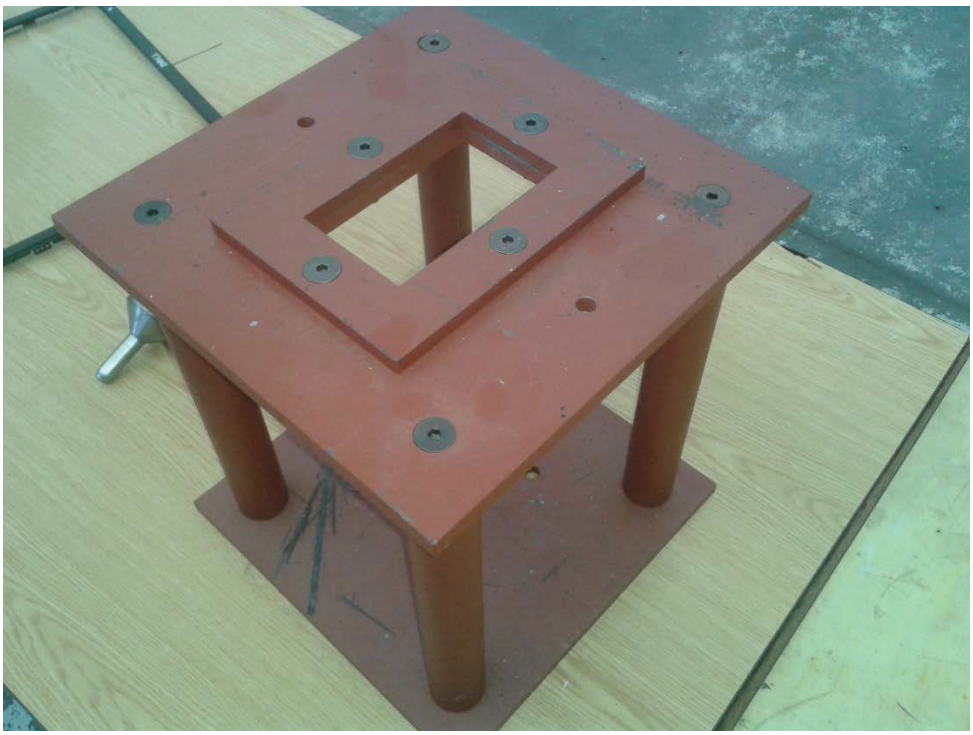

Figure 15: Actual Assembled Support Rig

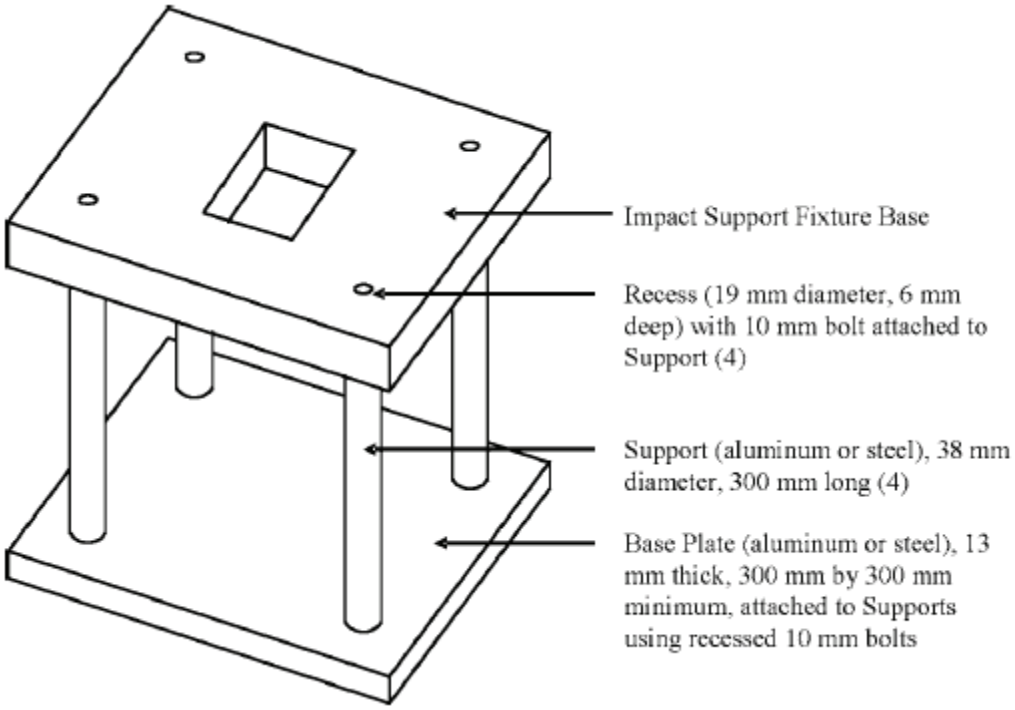

Figure 16: Illustration of Assembled Support Rig [30]

Figure 17: Trolley with Impactor Attached

The prescribed support rig shown in Figure 13 on page 23 was designed exactly to specification with the exception of adding six 12 mm holes. Four of these holes are spaced around the impact opening for the clamping mechanism that secures the sample. The spacing of these holes also serves to ensure consistent sample placement by being 0.5 mm away from the required edges of the samples. Thus when the bolts are inserted the sample is automatically aligned to within ±0.5 mm. The two extra holes on the sides are for securing cushioning materials to stop the trolley after the impactor penetrates the sample. The cushioning material is to prevent the trolley from destroying itself from repeated impacts.

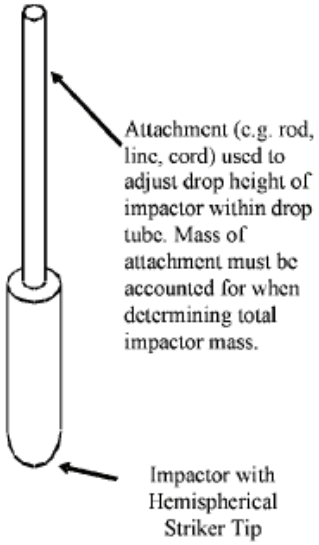

Figure 18: Illustration of Impactor [30]

The standard prescribes a cylindrical impactor as seen in Figure 15. However due to the use of the guided trolley system, an impactor had to be designed with a cylindrical impact feature with the specified dimensions in the standard as seen in Figure 16. However the experimental setup also differed from the testing standard in the impact weight. Due to the weight of the trolley the impact weight was 11.84 kg. This prompted the design modification to have a reinforced base in order to withstand the higher level of force caused by the additional weight.

Figure 19: Designed Impactor

3.2.2 Measurements: Hardware and Software

This section covers the hardware and software used to record and capture the impact force date generated by the experiments. This includes the load cell, the Quantum and the software catman.

The hardware used for measuring the impact forces was a C6 load cell as seen in Figure 17 manufactured by HBM, the technical sheet of which can be seen in Appendix A.1.

Figure 20: C6 Load Cell Installed in Testing Setup

Additionally for recording the data a QuantumX MX410 (Quantum), as seen in Figure 18, was used which was also produced by HBM. The maximum recording rate that the Quantum is capable of recording at is 96 000 Hz. Since the testing standard requires 100 data points at a sampling rate of 100 000 Hz and the tests produced 300-400 data points at 96 000 Hz it was deemed an acceptable discrepancy. The technical sheet of the Quantum can be seen in Appendix A.2.

An additional point of importance is with the natural frequency of the impact support structure. The ASTM standard D7136 reference the standard D3763 in terms of performance requirements. Standard D3763 states that typically a setup with a natural frequency greater than 6 kHz is required, however this requirement is set typically for plastics which fail at approximately 0.5 ms and with relatively low forces. The standard then stipulates that if a much tougher material is used with a longer impact time and high impact forces that a natural frequency of less than 6kHz will not adversely affect the results of the test data. This is due to damping effect of the sample itself and as well as the large magnitude of the loading forces.

Figure 21: QuantumX MX410B [31]

The software used in the data capturing process was catman Easy 3.4. Catman is the data acquisition software which is developed by HBM. The software can be used to define a sensor and assign it to a channel, thus ensuring that the correct forces are being measured and recorded.

3.3 Testing Samples

The specimen dimensions are specified to be 100 mm × 150 mm as seen in Figure 19. They were stacked to 20 layers which produced a sample thickness of 5 mm with a variance of ± 0.1 mm as seen in Figure 20. The material used for the experiments was a Unidirectional (UD) epoxy Carbon Fibre pre-impregnated (prepreg) material with a fibre areal mass of 200 g/m^2 with a resin content of 42%. The prepreg areal mass of the material totals to 345 g/m^2. The list of mechanical properties can be found in appendix C.1. The testing standard requires 5 samples per orientation set, however since a higher confidence level was desired each set consisted of 10 samples per set. [30]

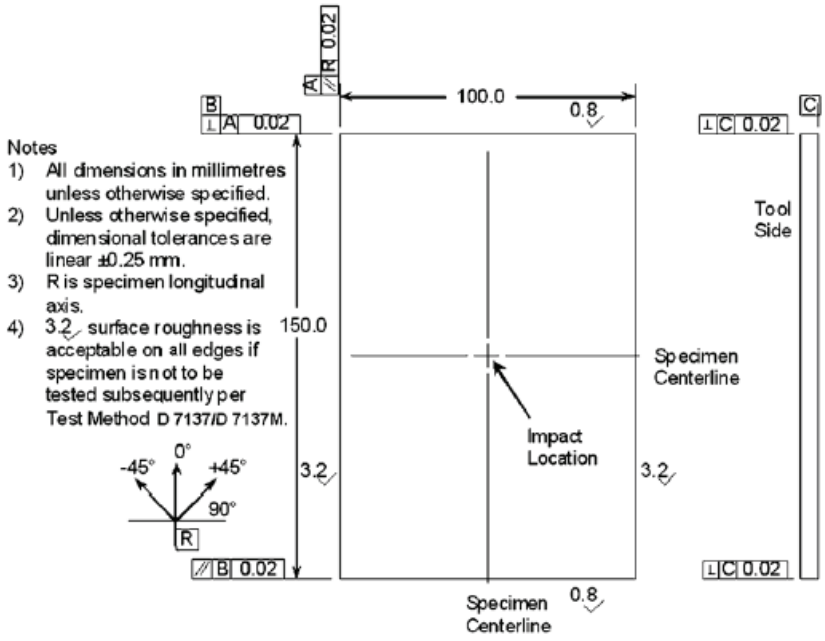

Figure 22: Specimen Dimensions [30]

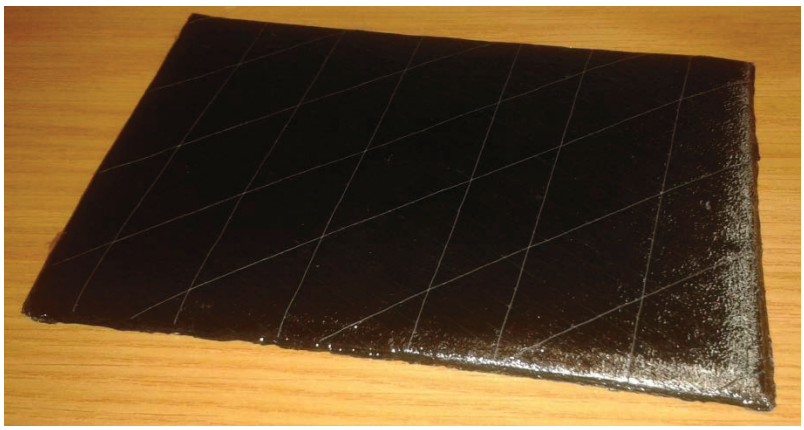

Figure 23: 20 Ply Carbon Fibre Sample

The first samples sets that were made for this project were uniform 0° and 90°. Their purpose was to determine whether fibre length plays a role in the impact resistance of samples tested on the available experimental setup. It was necessary to determine this characteristic since it would determine the starting orientations of later sample sets and because the test samples were not square.

Sample sets with layup angles of $[0,30,60,90,-60,-30,0,30,60,90]_s$ (30° symmetrical) and $[0,45,90,-45,0,45,90,-45,0,45]_s$ (45° symmetrical) were made to start off with. This was to confirm on the available equipment what has been found in literature; that decreasing the offset angle will improve impact resistance even on larger offset angles.

The next sample sets that were made was the $[0,15,30,45,60,75,90,-75,-60,-45]_s$ (15° symmetrical) and $[0,10,20,30,40,50,60,70,80,90]_s$ (10° symmetrical) sets. These were made in order to evaluate whether the effect observed in the first tests would also apply to the smaller offset angles.

Lastly the continuous samples were created starting with [0,15,30,45,60,75,90,-75,-60,-45,-30,-15,0,15,30,45,60,75,90,-75] (15° continuous) and [0,10,20,30,40, 50,60,70,80,90,-80,-70,-60,-50,-40,-30,-20,-10,0,10] (10° continuous). These samples were made to test the effect of whether making a sample continuous makes is more impact resistant. These two sets were the only planned continuous sample sets, however after they displayed interesting characteristics sets with the orientations of [0,30,60,90,-60,-30,0,30,60,90,-60,-30,0,30,60,90,-60,-30,0,30] (30° continuous), and [0,45,90,-45,0,45,90,-45,0,45, 90,-45,0,45,90,-45,0,45,90,-45] (45° continuous) were also made in order to determine if the characteristics extended beyond the smaller offset angles.

The samples were cured for 2 hours in a vacuum seal in an oven at 120°C as per the technical instructions seen in appendix C.1. An autoclave would have been preferable; however the available autoclave was out of commission.

3.4 Energy Absorption

This section covers the calculations involved with calculating the energy absorption of the test samples based on the recorded impact forces. The formulas for the calculations were obtained from the testing standard. It should be noted that large force spikes after complete sample failure were ignored for analysis. These force spikes were caused by the bulk of the trolley impacting the support fixture.

3.4.1 Velocity vs. Time

The method of measurement is a load cell capable of measuring contact force with the Quantum giving each measurement a timestamp. By applying numerical integration to the force vs. time data a nominal velocity vs. time curve can be generated by using equation (9) shown below:

$$\boldsymbol{v(t) = v_i + g\,t - \int_0^t \frac{F(t)}{m}\,dt} \tag{9}$$

where:

v = impactor velocity at time t in m/s, a positive value indicates downward velocity,

v_i is initial velocity at moment of impact in m/s at t = 0. Experiment was designed to have a consistent impact velocity calculated to be 5.72 m/s which was done by controlling the drop height

t= time during test in s, t = 0 is initial contact between impactor and sample,

F = force in N at time t,

m = impact mass in kg,

dt = time step in s, inverse of sampling rate = 1/ 96 000 s,

g = gravitational acceleration = 9.81m/s^2.

The impactor velocity at the moment of impact is calculated from the force history plot and drop height. This is possible due to the fact that there is a large spike in the data at the moment of release accurate to within 1/48000 of a second. This coupled with exact drop height of the impactor can be translated into the impact velocity through basic motion equations. The drop height was 1.67 m, the drop time was 0.611s and the initial velocity 0 m/s^{-1}.

3.4.2 Impactor Displacement vs. Time

The impactor displacement vs. time curve is generated by using numerical integration and equation (10) shown below: [30]

$$\boldsymbol{\delta(t) = \delta_i + v_i\,t + \frac{g\,t^2}{2} - \int_0^t \left(\int_0^t \frac{F(t)}{m}\,dt\right) dt} \tag{10}$$

where:

δ = impactor displacement at time t in m,
δ_i = initial impactor displacement from reference location in m, since the reference location is the sample surface δ_i = 0 m.

3.4.3 Absorbed Energy vs. Time

By using the curves generated by equations 1 and 2 the absorbed energy vs. time curve can be calculated by using equation (11) shown below:

$$E_a(t) = \frac{m(v_i^2 - v(t)^2)}{2} + m\,g\,\delta(t) \tag{11}$$

where

E_a = energy absorbed in J at time t

3.5 Statistical Significance

The statistical significance test was done on the impact energy absorption of each sample set. A confidence level of 95% was selected for the experiments. An initial 5 samples were tested per set in order to get initial statistical values. Additionally a standard deviation of less than 5% of the average was considered acceptable. A margin of error of less than 4% of the sample set average was considered acceptable as well. [32]

The sample standard deviation was obtained by using equation (12) as seen below:[33]

$$\sigma = \sqrt{\frac{1}{N-1}\sum_{i=1}^{N}(x_i - \bar{x})^2} \tag{12}$$

where:

N = number of samples tested
σ = standard deviation of current samples
x_i = test value
$\bar{x}$ = sample set average

Based on these values the number of samples required to be tested in order to establish the 95% confidence level was determined by using equation (13) shown below:[33]

$$N = \left(\frac{z_{\alpha/2}\,\sigma}{E}\right)^2 \tag{13}$$

where:

N = minimum number of samples to be tested

$z_{\alpha/2}$ = critical value from the normal distribution.

E = margin of error

3.6 Warping

Warpage in composites occur during the curing cycle and is typically caused by out-of-plane stresses due to the difference in how the fibres and matrix change volume due to the temperature during the curing process. The difference is due to the fact that the fibres are not affected by the change in temperature, but the matrix goes through large changes in volume. However when the sample is stacked symmetrically about the mid-plane these stress cancel each other out and thus eliminates warpage. The characteristics of composite warpage can by calculated by the three stiffness matrices namely: the extensional compliance matrix ([A]), the coupling compliance matrix([B]) and the bending compliance matrix([D]). The reduced stiffness matrix ([Q]) is given by the equations (14) to (18) as seen below: [34]

$$\boldsymbol{v_{12}} = \frac{\boldsymbol{E_2 v_{12}}}{\boldsymbol{E_1}} \tag{14}$$

$$\boldsymbol{Q_{11}} = \frac{\boldsymbol{E_1}}{\boldsymbol{(1-v_{12}v_{21})}} \tag{15}$$

$$\boldsymbol{Q_{12}} = \frac{\boldsymbol{E_2 \times v_{12}}}{\boldsymbol{(1-v_{12}v_{21})}} \tag{16}$$

$$\boldsymbol{Q_{22}} = \frac{\boldsymbol{E_2}}{\boldsymbol{(1-v_{12}v_{21})}} \tag{17}$$

$$\mathbf{Q_{33}} = \boldsymbol{G_{12}} \tag{18}$$

where:

E_1 = Young's modulus in fibre direction in MPa,

E_2 = Young's modulus in normal direction in MPa,

ν_{12} = Major Poisson's ratio,

ν_{21} = Minor Poisson's ratio,

G_{12} = In-plane shear modulus in MPa.

Which were obtained from the technical sheet in Appendix C.3 and research done by Feraboli et al. who made use of a similar material. [35]

And $Q_{13} = Q_{23} = Q_{31} = Q_{32} = 0$

This yields the [Q] matrix:

$$[\boldsymbol{Q}] = \begin{bmatrix} \boldsymbol{Q_{11}} & \boldsymbol{Q_{12}} & \boldsymbol{0} \\ \boldsymbol{Q_{12}} & \boldsymbol{Q_{22}} & \boldsymbol{0} \\ \boldsymbol{0} & \boldsymbol{0} & \boldsymbol{Q_{33}} \end{bmatrix} \tag{19}$$

From this the transform matrix [$\bar{Q}$] can be calculated by equations (20) to (25): [34]

$$\bar{\boldsymbol{Q}}_{\boldsymbol{11}} = \boldsymbol{Q_{11}c^4 + Q_{22}s^4 + 2(Q_{12} + 2Q_{33})s^2c^2} \tag{20}$$

$$\bar{\boldsymbol{Q}}_{\boldsymbol{12}} = \boldsymbol{(Q_{11} + Q_{22} - 4Q_{33})s^2c^2 + Q_{12}(s^4 + c^4)} \tag{21}$$

$$\bar{\boldsymbol{Q}}_{\boldsymbol{22}} = \boldsymbol{Q_{11}s^4 + Q_{22}c^4 + 2(Q_{12} + 2Q_{33})s^2c^2} \tag{22}$$

$$\bar{\boldsymbol{Q}}_{\boldsymbol{13}} = \boldsymbol{(Q_{11} - Q_{12} - 2Q_{33})sc^3 - (Q_{22} - Q_{12} - 2Q_{33})s^3c} \tag{23}$$

$$\bar{\boldsymbol{Q}}_{\boldsymbol{23}} = \boldsymbol{(Q_{11} - Q_{12} - 2Q_{33})cs^3 - (Q_{22} - Q_{12} - 2Q_{33})c^3s} \tag{24}$$

$$\bar{\boldsymbol{Q}}_{\boldsymbol{33}} = \boldsymbol{(Q_{11} - Q_{22} - 2Q_{12} - 2Q_{33})c^2s^2 + Q_{33}(s^4 + c^4)} \tag{25}$$

where:

c = cos(θ),

s = sin(θ),

θ = Angle of rotation of the layer.

Which yields the [$\bar{Q}$] matrix:

$$[\bar{\boldsymbol{Q}}] = \begin{bmatrix} \bar{\boldsymbol{Q}}_{\boldsymbol{11}} & \bar{\boldsymbol{Q}}_{\boldsymbol{12}} & \bar{\boldsymbol{Q}}_{\boldsymbol{13}} \\ \bar{\boldsymbol{Q}}_{\boldsymbol{12}} & \bar{\boldsymbol{Q}}_{\boldsymbol{22}} & \bar{\boldsymbol{Q}}_{\boldsymbol{23}} \\ \bar{\boldsymbol{Q}}_{\boldsymbol{13}} & \bar{\boldsymbol{Q}}_{\boldsymbol{23}} & \bar{\boldsymbol{Q}}_{\boldsymbol{33}} \end{bmatrix} \tag{26}$$

From [$\bar{Q}$] the stiffness matrices [A], [B] and [D] can be calculated by using equations (27) to (29): [34]

$$\boldsymbol{A_{ij} = \sum_{k=1}^{n} \left[\left(\bar{Q}_{ij}\right)\right]_k (h_k - h_{k-1}), \quad i = 1,2,3; \quad j = 1,2,3} \tag{27}$$

$$\boldsymbol{B_{ij} = \frac{1}{2} \sum_{k=1}^{n} \left[\left(\bar{Q}_{ij}\right)\right]_k \left(h_k^2 - h_{k-1}^2\right), \quad i = 1,2,3; \quad j = 1,2,3} \tag{28}$$

$$\boldsymbol{D_{ij} = \frac{1}{3}\sum_{k=1}^{n}\left[\left(\bar{Q}_{ij}\right)\right]_k\left(h_k^3 - h_{k-1}^3\right),\ \ i = 1,2,3;\ \ \ j = 1,2,3} \qquad (29)$$

The effects of the different coupling mechanisms can be seen in Figure 23.

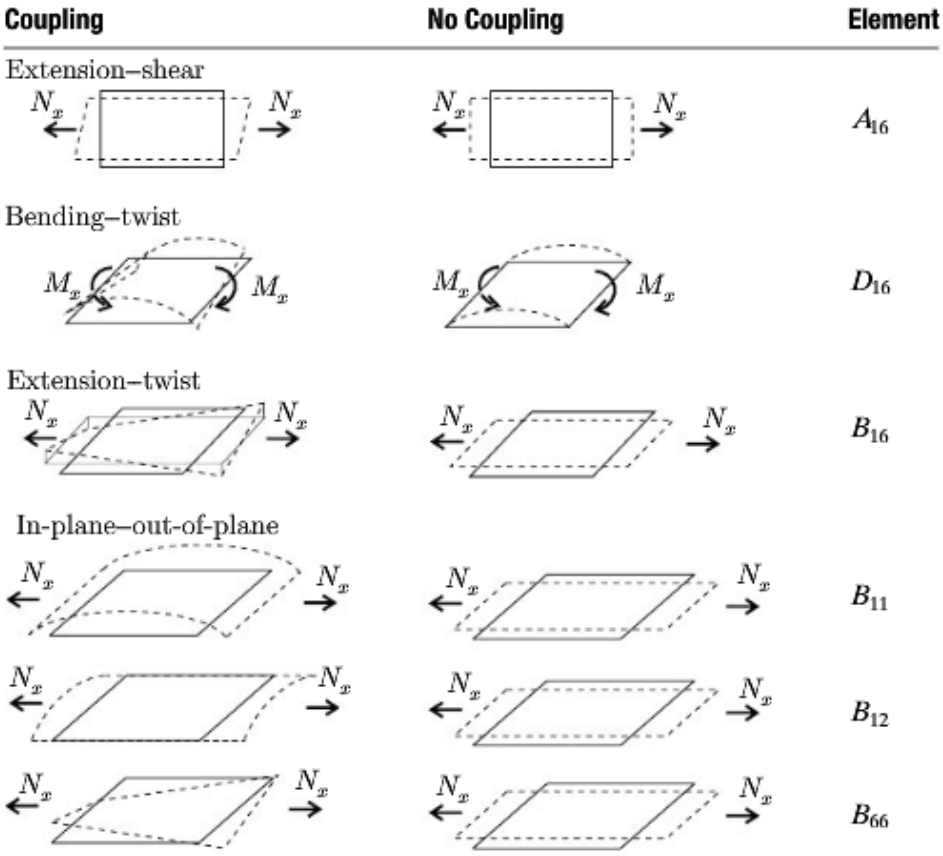

Figure 24: Different Coupling Modes And Their Effects [36]

Thus based on the warpage that occurs the relevant factors can be evaluated.

3.7 CT Scans

Computed Tomography scans (CT scans), is a technology known by many different names that varies depending on the field that it is used such as X-ray tomography, microCT, X-ray microscopy, 3D scanning and industrial CT. The technology is based on projecting low intensity X-rays through the sample and recording the resulting X-rays that pass through. When a material is denser, meaning it has a higher atomic mass, less X-rays pass through to the receptors and thus different materials can be differentiated. In CT scanning the sample is rotated while being scanned continuously which allows the computer to compile a 3D image of the sample. The level of detail obtainable is determined by the size of the scanned sample. Thus it is a non-destructive method of investigating internal damage within the samples.

3.8 Experimental procedure

Prior to each experiment a pre-experiment checklist is conducted with the following items:

- Ensure software loaded properly and is functioning normally
- Ensure a stable connection between load cell and Quantum exist
- Ensure a stable connection between Quantum and laptop exist
- Ensure that correct experimental settings are selected which include:
    - Sensor settings
    - Sample rate – 96 000 Hz
    - Storage format – ASCII double precision
    - Record data types – force and time
- Calibrate the sensor
- Test load cell response to a temporary weight to ensure the system is responsive to input

Following the checklist the test sample is secured to the support fixture. Next the impact cage is closed and secured with protective screens before the trolley is raised to 1.67 m. After raising the trolley the data recording is switched on and the trolley is released. Once impact is complete the data recording is switched off and the data is saved to ASCII text file. The samples are then removed and the damaged area evaluated and measured. The data was then converted from ASCII to an Excel format in order to make it easier to process. ASCII storage was selected due to the software not being capable of storing more than 75000 data points in Excel format and each test typically yielded 200000 data points. The data was then filtered in order to find the impact data points which was then processed by using equations (9) through (11).

The apparatus used in this experiment will be:

- Micrometers and callipers, used for measuring the damaged area.
- Support fixture, used for clamping the specimen and transferring the force to the load cell.
- Impact device, consist out of the impactor (weighted trolley) and guide mechanism (dual rails).
    - Impactor should have a weight of 5.50 kg ± 0.25 kg.
    - However the impactor has a weight of 11.84 kg.

- Data acquisition equipment:
    - C6 load cell was used to measure force.
    - QuantumX MX410B was used to record the data from the load cell.
- Weighing scale, used for determining the impact weight.

The following is a list of factors that could potentially affect the results and was thus carefully controlled: [30]

- Laminate thickness
- Epoxy used
- Ply thickness
- Stacking sequence
- Geometry
- Impactor mass
- Striker tip geometry
- Impact velocity
- Impact energy
- Boundary conditions
- Material and specimen preparation
- Impact location
- Support fixture characteristics
- Impact device characteristics
- Force oscillations
- Dent depth might reduce with time

The thicker a laminate is the higher the impact resistance will be. The epoxy used will affect the interlaminar material properties and thus crack propagation. If ply thickness varies then certain fibre orientations could have a more pronounced affect than others. Stacking sequence can affect crack propagation within the sample. The geometry of the sample can introduce stress concentrating factors. The impactor mass and impact velocity determines the impact energy as well as the type of impact. The type of impact is either low weight with high speed or high weight with low speed. The striker tip geometry influences the ratio of

internal damage vs. external damage. The boundary conditions can inhibit crack propagation into the clamped region. Material and sample preparation has an effect on sample consistency between experiments. The impact location has an effect on stress concentration and the way cracks are allowed to propagate. Support fixture and impact device characteristics have an effect on force oscillations due to natural harmonics. Dent depth reducing due to time is not a concern due to samples failing completely.

By using prepreg material subjected to a consistent curing cycle laminate thickness, epoxy used and ply thickness was made constant. The stacking sequence of each sample was determined by the sample set it belonged to and great care was put into ensuring the correct placement of each ply. The geometry of each sample was ensured by making each sample slightly larger than necessary and after curing cutting them to exact size. The impactor mass and impact device characteristics were kept constant due to no changes being made between experiments. The integrity of the striker tip geometry was ensured by designing it to specification which included hardening it in order to prevent deformation. Impact velocity and energy were kept constant by raising the impactor to an exact height for each test. The boundary conditions, support fixture characteristics and impact locations were controlled by the design of the support fixture which ensured consistent sample placement.

4. SIMULATION

Composites have several failure mechanisms such as matrix cracking, fibre matrix debonding, interlaminar damage, delamination and fibre breakage. [37][38] Additionally, as mentioned in section 3.7 there are several other factors that influence the response of the structure.

Due to this complex nature of composite behaviour most of the available Finite Element (FE) software packages are not capable of correctly simulating all of these characteristics. It is generally considered in the FE community that the current failure criteria for composite materials are not sufficient for simulating composite damage. Because of the importance of being able to simulate a composite model there has been extensive international research efforts and thus literature on composite crash simulation during the past 20 years. [38][39][40][41][42][43]

The current FE packages capable of composite damage modelling on a dynamic basis which are considered to be state-of-the-art are ABAQUS EXPLICIT, LS-DYNA, RADIOSS, SOLID WORKS and PAM-CRASH. LS-DYNA being the package generally considered being the golden standard by the aerospace and automotive industries for composite crash simulations. [44][45][46][47][48] All of these FE packages however use an explicit integration formulation for dynamic analysis which is computationally expensive. Thus, whenever possible 2 dimensional shell elements are used over the much more computationally expensive 3 dimensional brick elements. The approach that has been adopted by the FE industry in order to simulate composites is to use orthotropic shell elements with smeared material properties. By using smeared material properties it reduces the mathematically complex material model to a simplified approximation. The approximation is much cheaper computationally albeit slightly less accurate due to losing certain characteristics. In order to save additional computational cost all of the layers of the composite are simulated by utilizing a single shell element. The shell simulates a composite by addressing each layer as an integration point. This allows for different layers to have different material properties as well as different fibre angle orientations. [36]

The FE packages mentioned above make use of material models which characterise the elastic, plastic, failure and post-failure properties. These characteristics include material properties such as stiffness, strength, density, Poisson's ratio, etc. They also contain fine tuning parameters which cannot be determined experimentally. These properties require extensive calibration through trial and error in order to match simulation and experimental results. The Composite Materials Handbook-17 (CMH-17) crashworthiness and Worldwide Failure Exercise round robins concluded that due to these shortcomings current FE simulations of composites are not predictive.

For this project LS-DYNA was used for simulation purposes. The purpose of the simulations was to determine whether changing the offset-angle in the simulation would yield similar results as in reality and if it did whether the simulation could

determine the energy absorption mechanisms. The simulation consisted out of the impactor being simulated by a 3D solid sphere and the test samples simulated by a 2D shell plate. The following sections explain the detail of each simulation choice.

4.1 Elements

Two types of elements were used in the design of the simulations namely shell and solid elements. Shell elements were used in order to simulate the test sample and solid elements were used in order to simulate the impactor.

4.1.1 Shell

A shell plate was meshed in order to simulate the test sample. The dimensions of the sample were 150 mm by 100 mm as mentioned in section 3.3 with a thickness of 5 mm. The elements were meshed to be square with 150 elements across the x-direction and 100 elements across the y-direction which yielded a mesh of 15000 elements. A denser mesh of 300 by 200 elements was considered however it proved to be counterproductive as this made the simulation break from reality in terms of shattering completely as soon as contact is made with the impactor.

In order to define the material coordinate system and the initial material angle orientation there are three options. It can be defined from the material definition, the shell section definition and the element definition itself which will override any other existing and conflicting orientations. Following this there are two methods of declaring the individual fibre orientations. There first option is to define INTEGRATION_SHELL cards which can be linked to its own material definition and angle orientation to connect this card with the SECTION_SHELL for each individual layer. This method is very useful and the only viable option when different materials are used for different layers. However it is the computationally more expensive option. The second option is to make use of the beta angles that can be activated in the SECTION_SHELL card. This option is not capable of simulating several materials in a single section. However this project made use of it is due to it being considerably cheaper computationally, much simpler to use and due to the fact there was no need for multiple materials. The number of integration points and their angles were setup to have 2 integration points per layer in order to better simulate failure.

Shell element formulation type 16 was used which it the typically recommended shell element. It is a fully integrated shell element with a high level of predictability however it is fairly computationally expensive. The shell cards can be found in Appendix C.5.

4.1.2 Solid

A solid sphere was meshed in order to simulate the impactor. A sphere was selected because the radius of 8 mm of the impactor is larger than the thickness of the test samples which is 5 mm. Thus by the time the maximum width of the sphere passes through the sample full failure will have already occurred. The

sphere was meshed to have a density of 10 elements from the centre to the radius in order to ensure that the resolution of the impact is fine enough to detect all necessary factors.

4.2 Material Models

Two types of material models were used in the design of the simulations. MAT54 was used for the modelling of the composites and MAT20 was used for the modelling of the impactor.

4.2.1 MAT54_ Enhance Composite Damage

LS-DYNA has several composite material damage models which include: MAT22, MAT54/55, MAT58, MAT158 and MAT162. MAT22 and MAT54/55 are material models based on progressive failure that makes use of a ply discount method in order to simulate elastic material property degradation. MAT58, MAT158 and MAT162 utilize continuum damage mechanics in order to simulate the degradation of elastic properties.

The MAT54 material model is comparatively easier to use requiring fewer configuration parameters. While this does mean the computational cost of the model is lower and less testing is required to find all of the material properties, it also means it sacrifices accuracy by over-simplifying the system. In spite of this shortcoming caused by smeared properties, MAT54 is still a commonly used material model when simulating composites. Since it is designed for simulating unidirectional layered composite materials MAT54 was chosen to simulate the composite samples. The properties required to simulate the carbon fibre with the use of MAT54 was obtained from the technical sheet supplied by the manufacturers, through experimental results and information obtained from literature. [36] The MAT54 material card and input parameter definitions can be found in Appendix C.3. The values for tensile strength, elastic modulus and density were obtained from the technical sheet. The majority of the remaining factors were obtained from literature. [35] To test the validity of the values obtained the tensile test was performed with a thinner unidirectional sample of 4 plies with the results given in table 1, which found that the ultimate tensile strength, Young's modulus and maximum strain were within 5% of specified values.

Table 1: Tensile Test Parameters

Width (mm)	Thickness (mm)	Gage Length (mm)	Peak Load (N)	Peak Stress (MPa)	Peak Strain (mm/mm)	Modulus (GPa)
20	1	50	39983	1995	0.0154	129.8

4.2.2 MAT20_Rigid Material

The stiffness of the impactor is sufficiently larger than that of the test material and is considered to be rigid. Thus the MAT20 the rigid material model was used to

simulate the impactor due to fact that it cannot deform, to decrease computational cost and provides model stability.

4.3 Implementing Multiple Layers

Composite materials are typically made of multiple layers in a laminate. When no delamination is expected or if the laminate fails under tensile loads a simple constitutive model based on material parameters and angles will model damage to a satisfying degree for both single and multilayer laminates. However, while this type of model only accounts for ply failure within the sample, it cannot account for delamination and as such is flawed for multi layered composites.

In FEM shell elements are designed on plane stress conditions which means that the through thickness stress is assumed to be zero. This then requires that alternative methods of modelling interlaminar stresses be used. Three methods have been offered in literature that attempts to model delamination. The first method is to use stacked layers of solid elements with each layer representing a ply and tied in contact to the layers above and below it. The problem with this approach is that it is computationally expensive. The second approach is the same except shell elements are used. This is much less computationally expensive. For both of these approaches failure occurs between layers when the specified stress has been exceeded. The third approach is to use a single layer of shell elements that has integration points added for the resin rich layers between the plies. This is done in order to decrease the high computational costs of the stacked solid and shell element methods.

This project made use of the second approach. After defining the 20 shell layers as separated by the width of the shell the contact conditions were defined. It was implemented by using the CONTACT_TIEBREAK_SURFACE_TO_SURFACE data card. The data card requires the user to create a master-slave relationship between two layers and then stipulate the tensile and shear stress failure points which are matrix dominated. The maximum friction force is limited by the VC value on the tiebreak contact card. The LS-DYNA manual suggests a value seen in equation (30)

$$\boldsymbol{VC} = \frac{\boldsymbol{\tau_{yield}}}{\sqrt{\boldsymbol{3}}} \qquad 30$$

The shell layers were connected in a staggered format, for example layers 1-2, 2-3, 3-4, etc. It was decided to create different material models for each layer of orientation since the beta offset-angles on the shell element card can only be recorded 8 at a time which in turn means 8 integration points. This increases the computational costs considerably.

4.4 Loads and Boundary Conditions

The test sample has a band of 12 mm around the edges which has fixed translational degrees of freedom but have free rotational degrees of freedom in order to simulate the clamp that secures it. The entire sphere has all of its degrees of freedom fixed except for its movement in the z-direction. The entire sphere has an initial velocity of -5.72 m/s. Negative z-direction is considered to be the direction of gravity, with the sample defined in the x-y plane as can be seen in Figure 24.

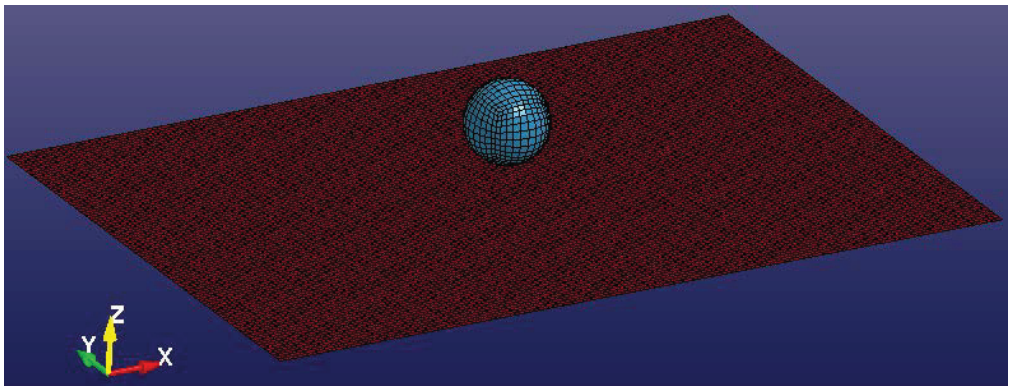

Figure 25: Axis System Used of Simulations

4.5 Miscellaneous Simulation Settings

The contact model used in the simulations was automatic surface-to-surface. It was selected due to ease of use and the fact that LS-DYNA uses explicit calculations and time steps being small enough that it was able to capture the contact satisfactorily. The impactor was selected to be the master component and the test sample was selected as slave. Termination time was selected to be 0.004 s in order to ensure enough time for the impact to complete yet not too long to unnecessarily increase computational cost.

4.6 Simulation results

The results of the simulations were compiled and tabulated into the graph seen in Figure 26 below. It should be noted however that the results of the preliminary experiments could not be used to fine tune the model. This is due to the failure mode that was observed in the experimental results, as seen in section 5.2, which could not reproduced in the simulations. As a result of this the simulation could not be calibrated to match the experimental results and the system had to be used as-is. In spite of this however it should be noted that simulation results did confirm that fibre length does not affect the impact resistance since the 0° and 90° unidirectional samples had the same results.

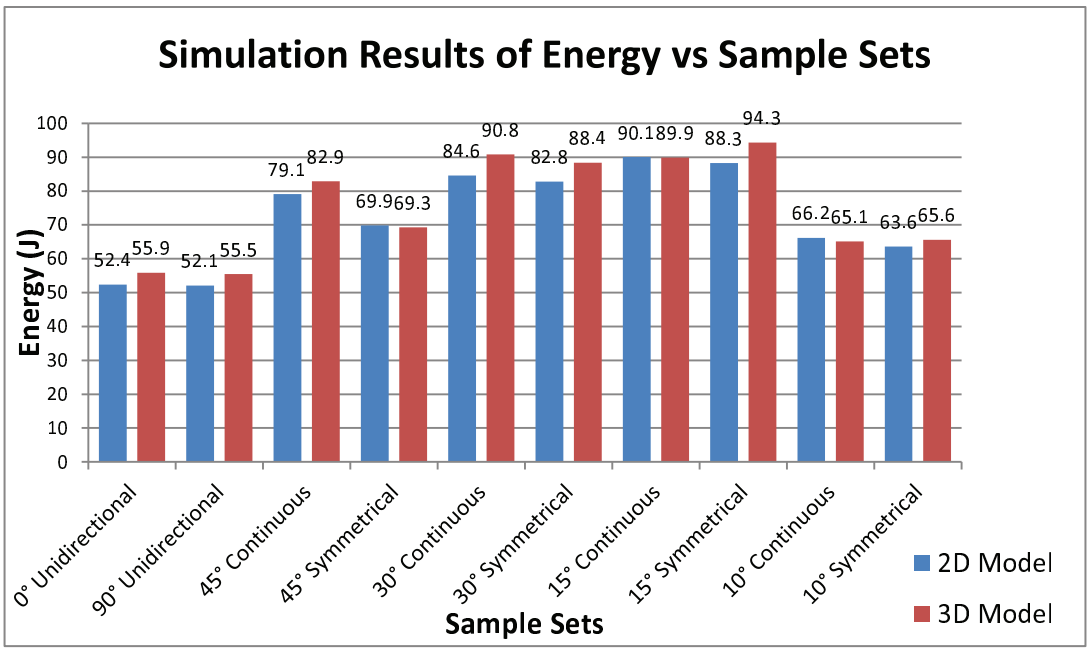

Figure 26: Simulations Results of Kinetic Energy Converted Into Internal and Hourglass Energy for Each Sample Set

As can be seen Figure 26 both the three dimensional and two dimensional simulations indicate that there will be a performance increase observed by reducing the offset angle size till 15° with a sharp drop off predicted for the 10° sample sets. The simulations also indicate a slight performance increase from symmetrical samples to continuous samples.

A slight performance increase can be observed from the single shell model to the stacked shell model with up to 7% separating the two sets. This implies that delamination is a relatively small percentage of the energy absorption mechanism, which corroborates with what Van der Westhuizen found in his work.

Figures 27 and 28 shown on page 43 are images of the two and three dimensional simulations respectively after impact is completed. The single shell sample is represented by the red sheet as viewed from above with the impactor represented by blue sphere. The faded region in the centre of the sample that is visible is the area that has already fully failed and the elements of the region have thus been deleted. For all of the images in Appendix F the same description will be valid as laid out for Figure 27. The stacked shell model is represented by multiple sheets of varying colours with damage being visible as the multicolour region at the centre of the sample. The 0° direction is along the length of the sample.

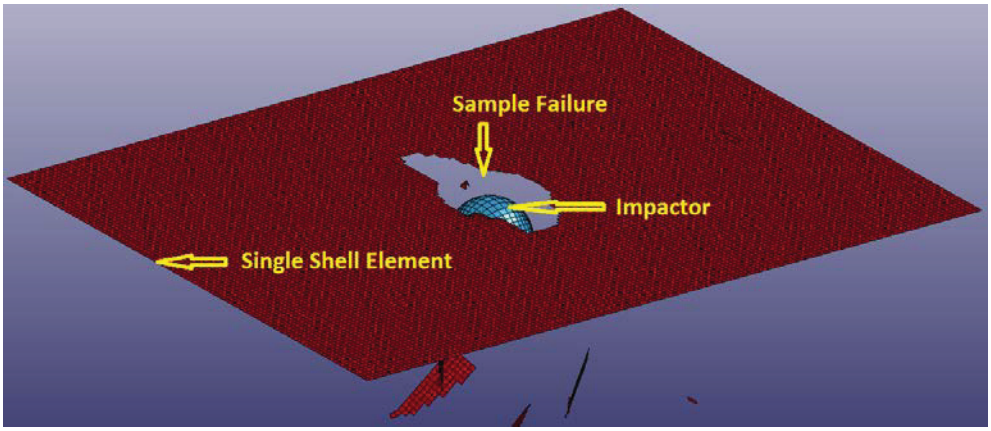

Figure 27: Example of a Two dimensional Simulation

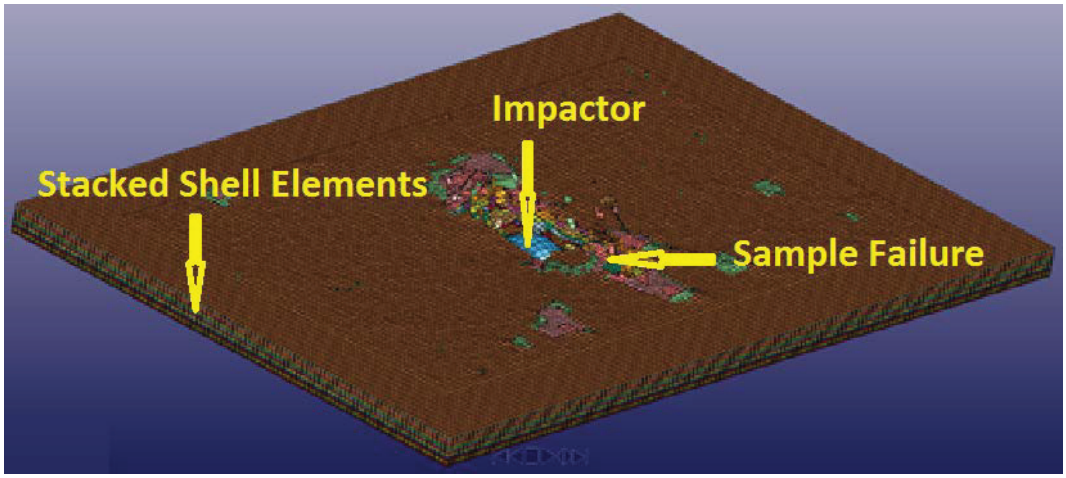

Figure 28: Example of a Three Dimensional Simulation

Four images of each three dimensional simulation can be found in Appendix G due to the images needing to be viewed together in order to get a clearer understanding of the crack propagation. The double front crack rotation, similar to that observed by Weaver et al. [2], can be seen in most of the samples, albeit to a much smaller degree than the actual results.

After reviewing all of the three dimensional simulations' data a common response was discovered in the contact forces. It was found that the peak contact forces generated during every simulation was in or near the middle plane of the samples. Figure 29 shows a subset of data from typical force vs. time response with the Sl numbers in the image legend referring to layer numbers.

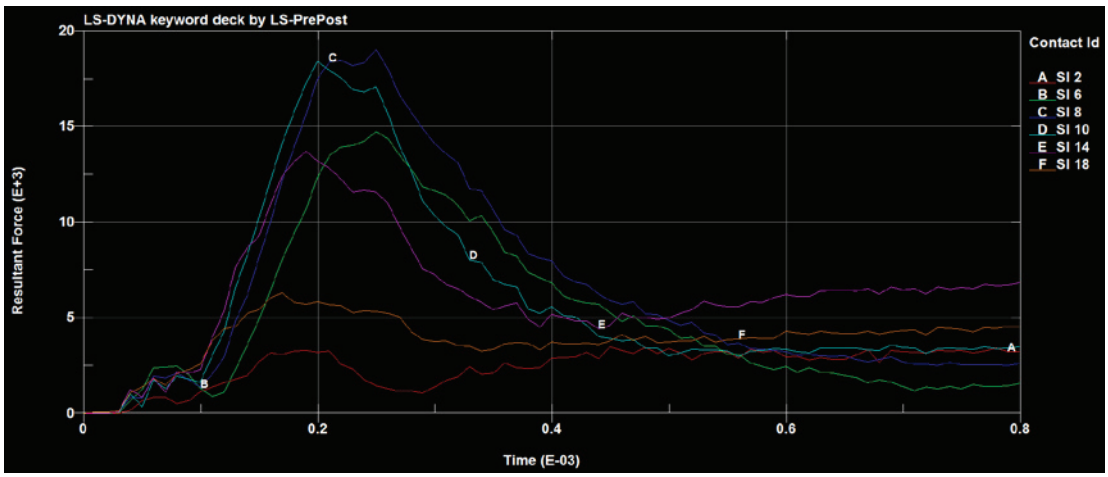

Figure 29: Typical Force vs Time Response of Three Dimensional Simulations

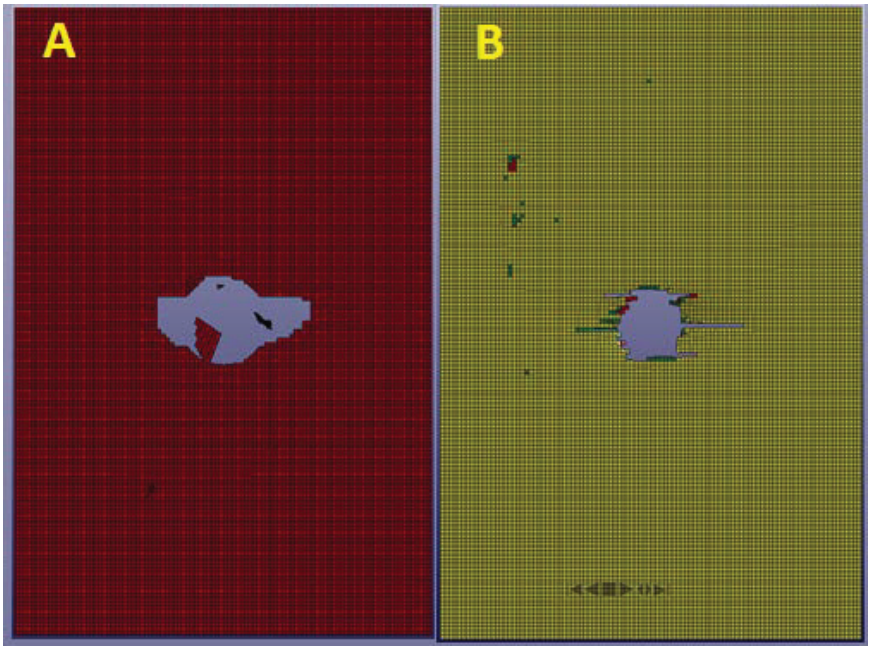

Figure 30: Simulation Result of 90° Unidirectional Sample Failure A: Single Shell, B: Mid-plane of Stacked Shell

As can be seen in Figure 30 the simulation predicts highly localised damage with fibre breakage primarily propagating along the width of the sample. This is due to the fibres running along the width of the sample.

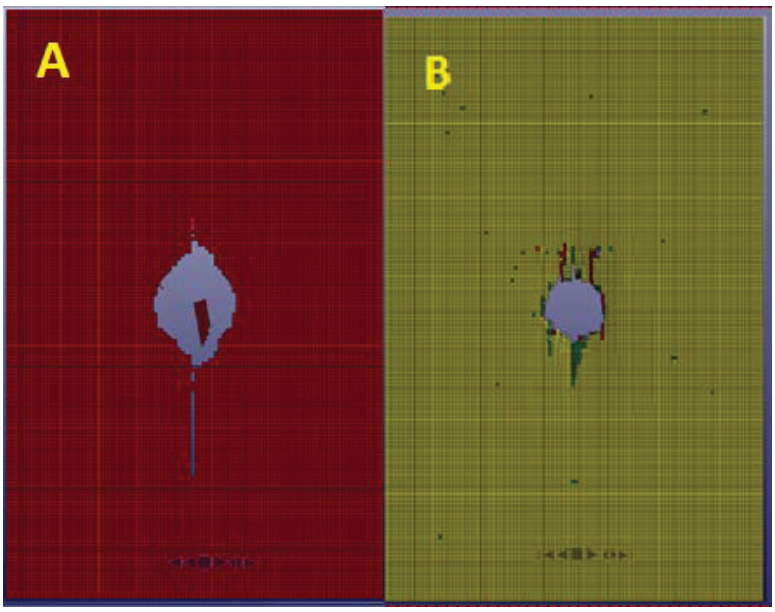

Figure 31: Simulation Result of 0° Unidirectional Sample Failure A: Single Shell, B: Mid-plane of Stacked Shell

As can be seen in Figure 31 the simulation predicts highly localised damage with fibre breakage primarily propagating along the length of the sample. This is due to the fibres running along the length of the sample.

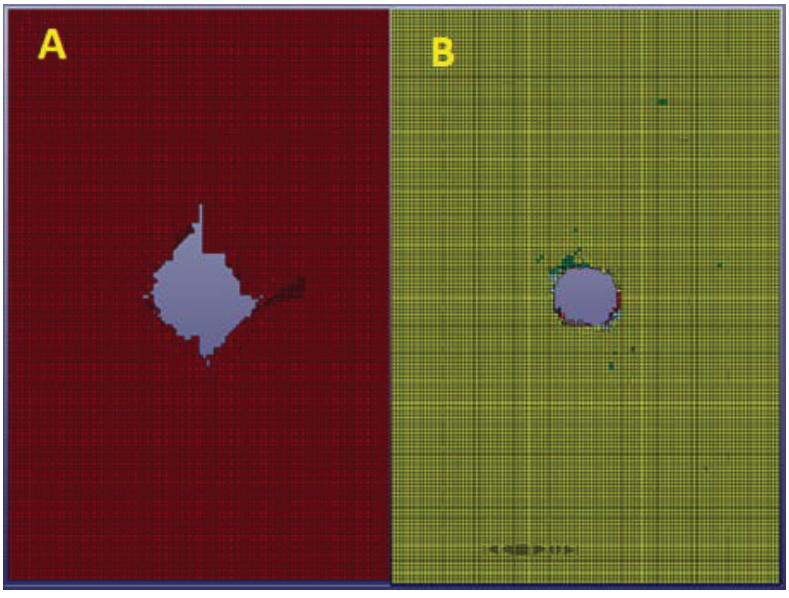

Figure 32: Simulation Result of 45° Symmetrical Sample Failure A: Single Shell, B: Mid-plane of Stacked Shell

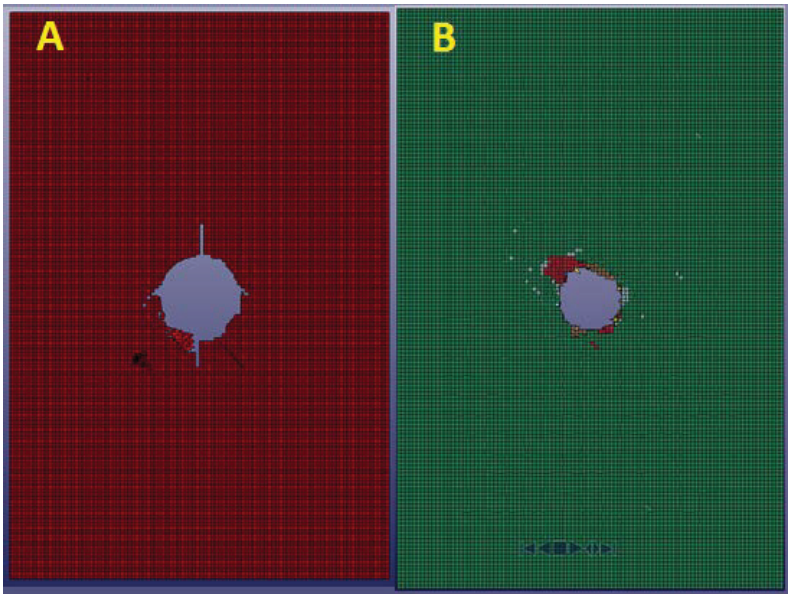

Figure 33: Simulation Result of 45° Continuous Sample Failure A: Single Shell, B: Mid-plane of Stacked Shell

As can be seen in Figure 32 and Figure 33 the simulation predicts highly localised damage. The single shell model also predicts that that the symmetrical samples will exhibit a larger puncture hole with some fibre breakage along the length of both samples.

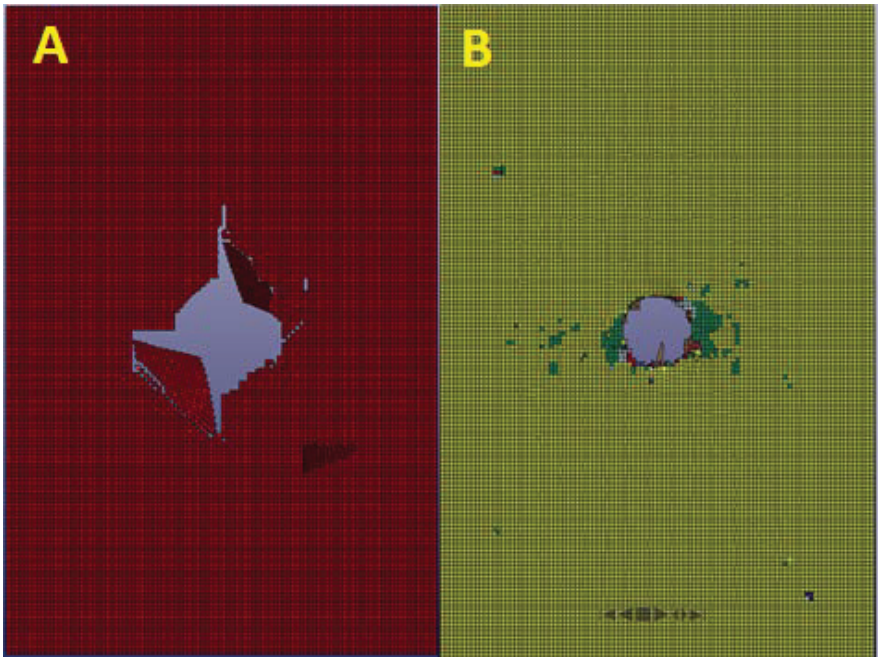

Figure 34: Simulation Result of 30° Symmetrical Sample Failure A: Single Shell, B: Mid-plane of Stacked Shell

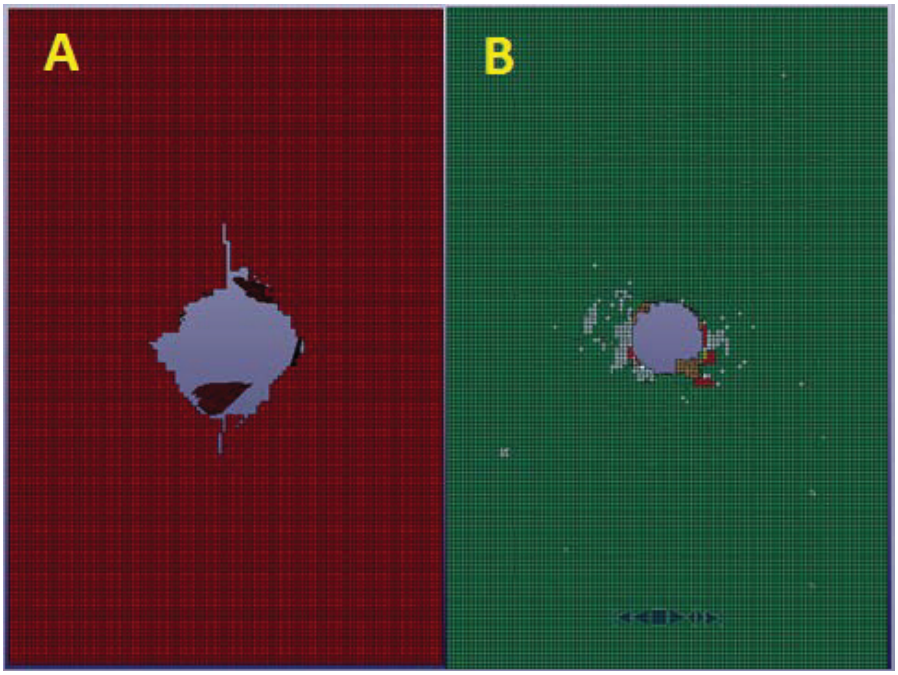

Figure 35: Simulation Result of 30° Continuous Sample Failure A: Single Shell, B: Mid-plane of Stacked Shell

As can be seen in Figure 34 and Figure 35 the simulation predicts relatively localized damage with some fibre breakage along the length of the sample. Some indications of crack rotation are visible in the simulations which can be seen further in Appendix F.

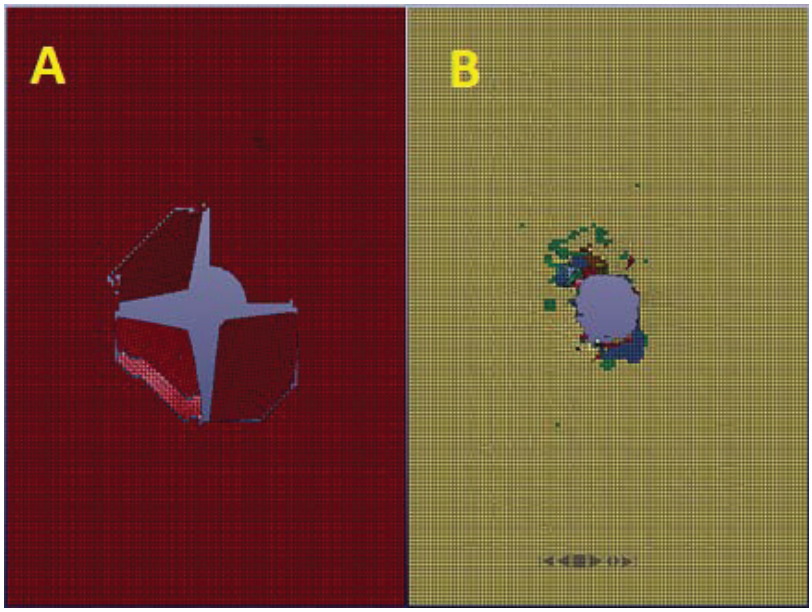

Figure 36: Simulation Result of 15° Symmetrical Sample Failure A: Single Shell, B: Mid-plane of Stacked Shell

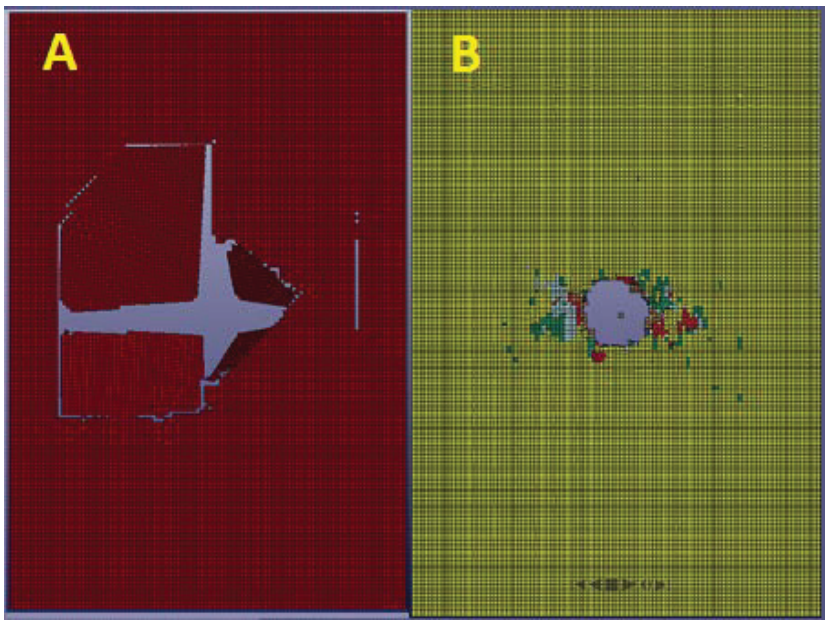

Figure 37: Simulation Result of 15° Continuous Sample Failure A: Single Shell, B: Mid-plane of Stacked Shell

As can be seen in Figure 36 and Figure 37 the simulation predicts cracks that propagate further with some fibre breakage along the length of the sample. The predicted damage extends up until the clamped boundary area. This could be the reason why the simulations suggest that the 15° sets have the highest impact resistance. Additionally the stacked shell models have higher indications of the rotating crack front than the 30° sets which can be seen further in Appendix F.

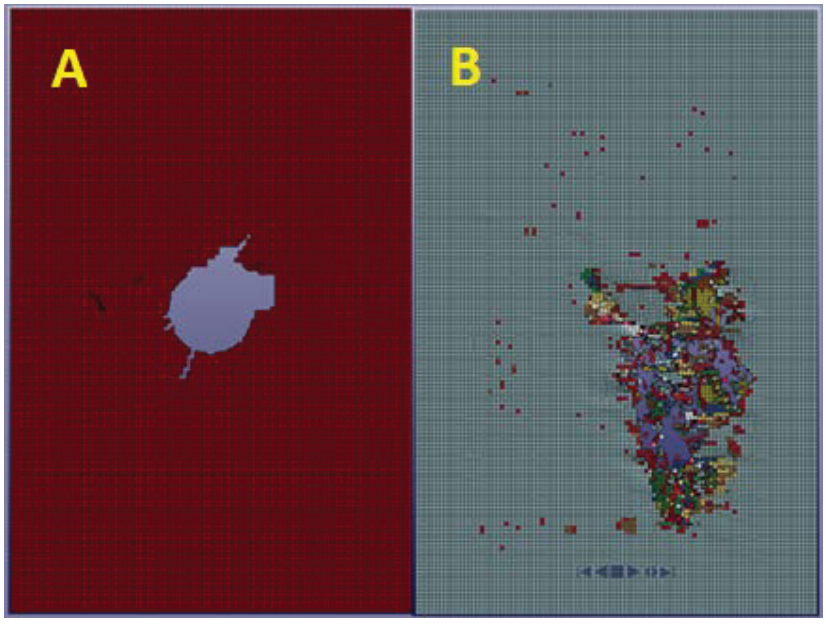

Figure 38: Simulation Result of 10° Symmetrical Sample Failure A: Single Shell, B: Mid-plane of Stacked Shell

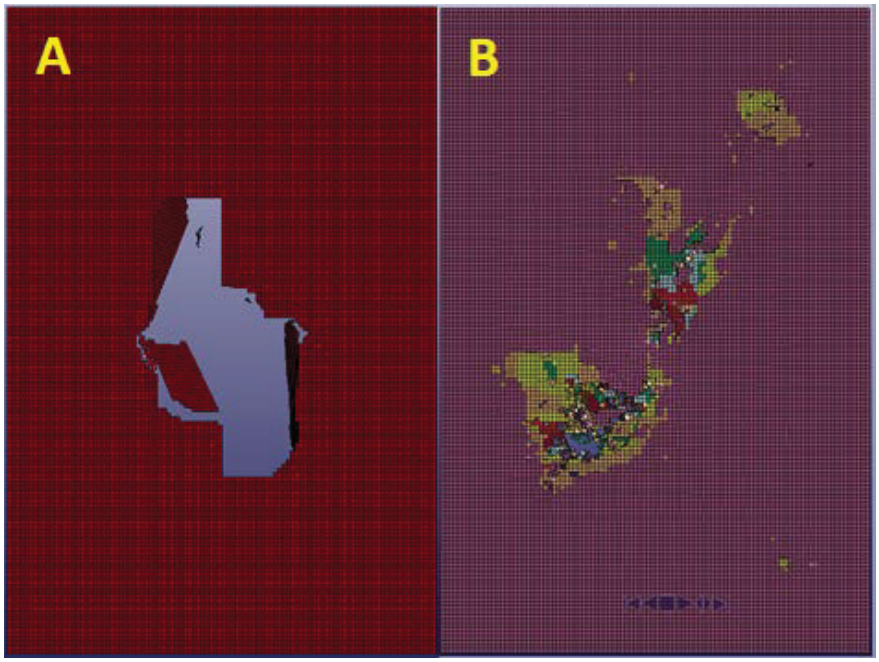

Figure 39: Simulation Result of 10° Continuous Sample Failure A: Single Shell, B: Mid-plane of Stacked Shell

As can be seen in Figure 38 and Figure 39 the simulation predicts a low level of damage propagation with some fibre breakage along the length of the sample. In the single shell simulations, the predicted damage is much smaller than the 15° sample sets. Some indications of crack rotation are visible in the symmetrical sample as well as the continuous sample simulation; however they are more prominent in the latter.

5. RESULTS

This chapter discusses all of the results obtained from the experiments as well as compares them to the results obtained from the simulations. It discusses the warpage of the continuous samples, the energy absorption of the samples along with the statistics involved with them, the force curves of the different sample sets and how they differ and CT scans of the composites.

5.1 Warping

One of the objectives of this project was to determine whether a composite sample made with a continuous offset angle could be made without it warping during the curing process. After curing the 10° continuous sample set all of the samples were found to have warped, however none of samples of the 15° continuous set were found to have warped. This prompted an investigation into the properties of the coupling stiffness matrices. Comparing the warpage observed with the coupling modes and their effect as seen in Figure 23 it was found that the factor in question is B_{13}. The amount of warpage for each sample set can be seen in Figures 36, 37, 38, 39. From equations 6 to 20 and using the properties seen in the MAT54 card seen in Appendix C.3 the [A], [B] and [D] matrices were calculated for both sets which yielded the following matrices:

For the 10° continuous set:

$$[\boldsymbol{A}] = \begin{bmatrix} 6434 & 1648 & 1075 \\ 1648 & 5200 & 1173 \\ 1075 & 1173 & 1815 \end{bmatrix} \text{GPa/mm} \quad (31)$$

$$[\boldsymbol{B}] = \begin{bmatrix} -16000 & 2590 & 20160 \\ 2590 & 10820 & 16930 \\ 20160 & 16930 & 2590 \end{bmatrix} \text{GPa/mm}^2 \quad (32)$$

$$[\boldsymbol{D}] = \begin{bmatrix} 8.869 & 1.051 & 1.195 \\ 1.051 & 1.473 & 0.4206 \\ 1.195 & 0.4206 & 1.190 \end{bmatrix} \times 10^6 \text{ GPa/mm}^3 \quad (33)$$

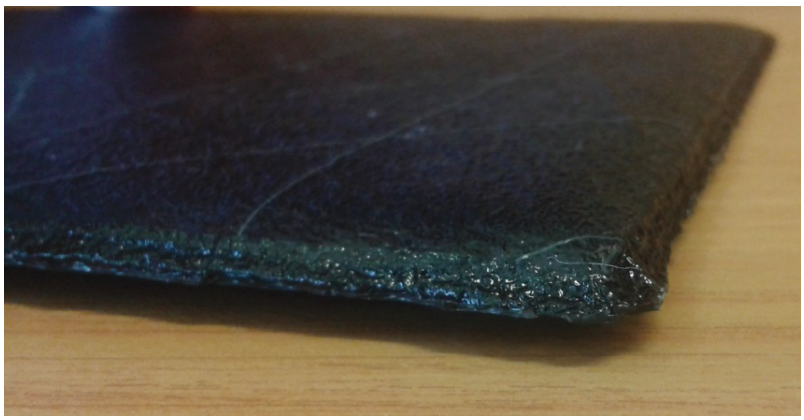

Figure 40: Warped 10° Continuous Sample

For the 15° continuous set:

$$[A] = \begin{bmatrix} 5521 & 1668 & 580.5 \\ 1668 & 6072 & 448.1 \\ 580.5 & 448.1 & 1835 \end{bmatrix} \text{GPa/mm} \quad (34)$$

$$[B] = \begin{bmatrix} 37670 & 1624 & 8077 \\ 1624 & -40920 & 2451 \\ 8077 & 2451 & 1624 \end{bmatrix} \text{GPa/mm}^2 \quad (35)$$

$$[D] = \begin{bmatrix} 4.554 & 1.175 & 1.096 \\ 1.009 & 5.537 & 0.7378 \\ 1.097 & 7.269 & 1.314 \end{bmatrix} \times 10^6 \text{ GPa/mm}^3 \quad (36)$$

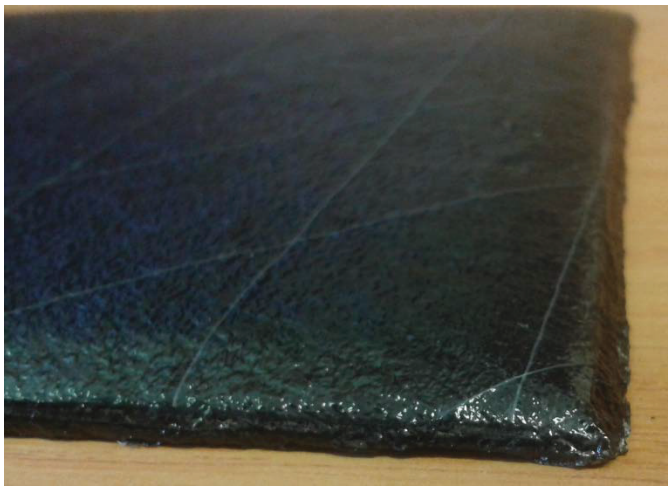

Figure 41: Warp-free 15° Continuous Sample

As can be seen the values of the two sets for B_{13} differ by an order of magnitude which is quite significant. However neither of the samples' [B] matrix is equal to 0 meaning that they should both have warped. Thus continuous samples sets were made for the 30° and 45° offset angles. All of the samples of both sets warped although significantly less than the 10° continuous set with the 30° set warping less than the 45° set.

For the 30° set:

$$[A] = \begin{bmatrix} 6198 & 1744 & 755.3 \\ 1744 & 5243 & 622.9 \\ 755.3 & 622.9 & 1912 \end{bmatrix} \text{GPa/mm} \quad (37)$$

$$[B] = \begin{bmatrix} -4756 & 2007 & 17820 \\ 2007 & 8770 & 21460 \\ 17820 & 21460 & -2007 \end{bmatrix} \text{GPa/mm}^2 \quad (38)$$

$$[D] = \begin{bmatrix} 6.120 & 1.393 & 0.8487 \\ 1.393 & 3.534 & 0.5960 \\ 0.8487 & 0.5960 & 1.533 \end{bmatrix} \times 10^6 \text{ GPa/mm}^3 \quad (39)$$

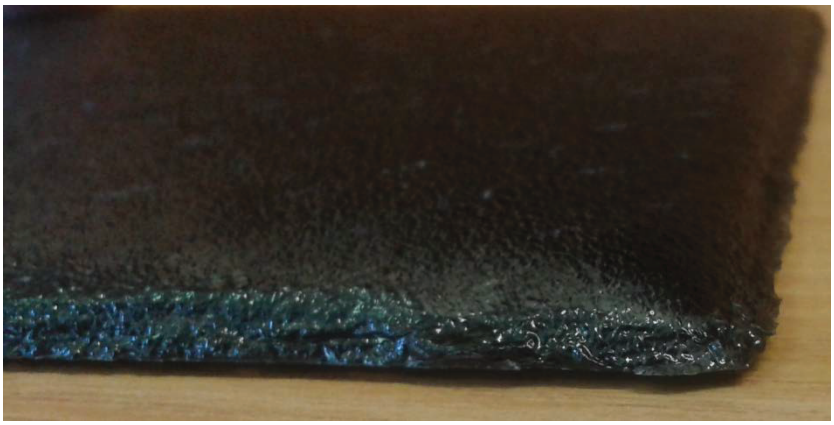

Figure 42: Warped 30° Continuous Sample

For the 45° set:

$$[A] = \begin{bmatrix} 5682 & 1783 & 636.5 \\ 1783 & 5682 & 636.5 \\ 636.5 & 636.5 & 1950 \end{bmatrix} \text{ GPa/mm} \quad (40)$$

$$[B] = \begin{bmatrix} 19730 & -3822 & 22280 \\ -3822 & -12090 & 22280 \\ 22280 & 22280 & -3822 \end{bmatrix} \text{ GPa/mm}^2 \quad (41)$$

$$[D] = \begin{bmatrix} 4.815 & 4.485 & 0.3474 \\ 4.485 & 4.656 & 0.3474 \\ 0.3474 & 0.3474 & 1.625 \end{bmatrix} \times 10^6 \text{ GPa/mm}^3 \quad (42)$$

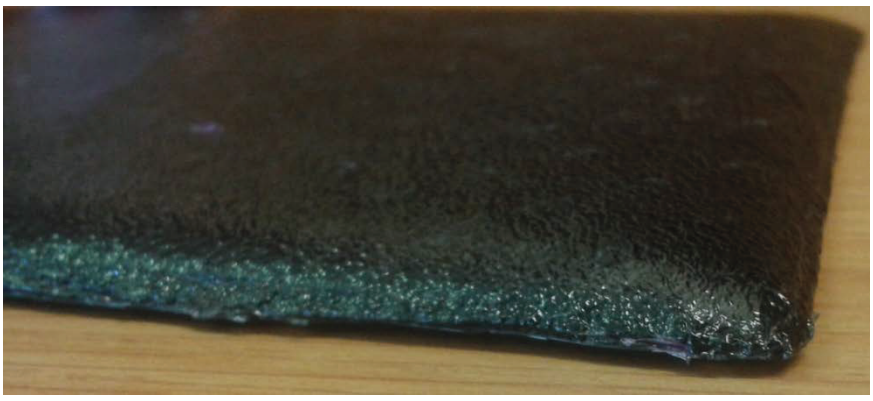

Figure 43: Warped 45° Sample

As can be seen in matrices 22, 28 and 31 the B_{13} values of the 10°, 30° and 45° sets are very similar in quantity. The 10° set has a value of 20160 GPa/mm^2, the 30° set has a value of 17820 GPa/mm^2 and the 45° set has a value of 22280 GPa/mm^2. While these values differ by several thousand, their percentage difference is relatively small and does not account for the significant difference in warpage. A possible factor is the difference in the B_{33} values. As can be seen in Figure 23 the B_{33} factor has a similar coupling factor as the B_{13} factor although slightly different. With the 30° and 45° sets having negative values for the B_{33} it might be counteracting the warping effect of the B_{13}. However this is just speculation, there could be other factors involved in warpage that is yet to be characterized since the 15° sample set did not warp at all.

5.2 Impact Results

The force vs. time data was generated from the drop-test experiments which are shown in Appendix D. It should be noted that the 45° and 30° samples were tested with the exact same equipment as all the other samples, thus the noise is unexplainable.

As can be seen in Figure 40 and in Figure 41 catastrophic failure occurs in a manner that does not lead to reproducible results. When the impactor strikes the sample, a strip roughly the same diameter is ripped loose from the one end of the sample which is then subject to the friction between the clamp and the support fixture as well as the composite material itself. The effect of this is that the impactor is allowed to move for a much longer distance and thus dissipate more energy. However an additional failure mode that exists is when the impactor simply splits the sample and almost no energy is absorbed.

When the failure modes observed in Figure 40 and Figure 41 are compared to the failure modes observed in Figure 26 and Figure 27 from the simulations the similarities and differences are easy to observe. While the simulation did correctly predict the direction of the fractures, it failed to predict the failure mode mentioned above. CT scans of these samples were not taken due to the obvious failure mode.

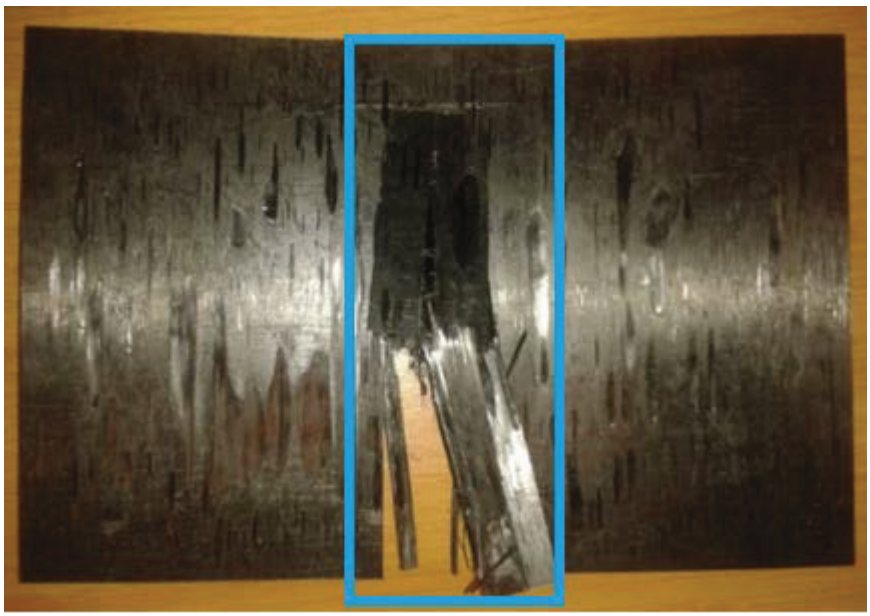

Figure 44: Backside of 90° Uniform Sample Post-Impact With Damaged Region Highlighted

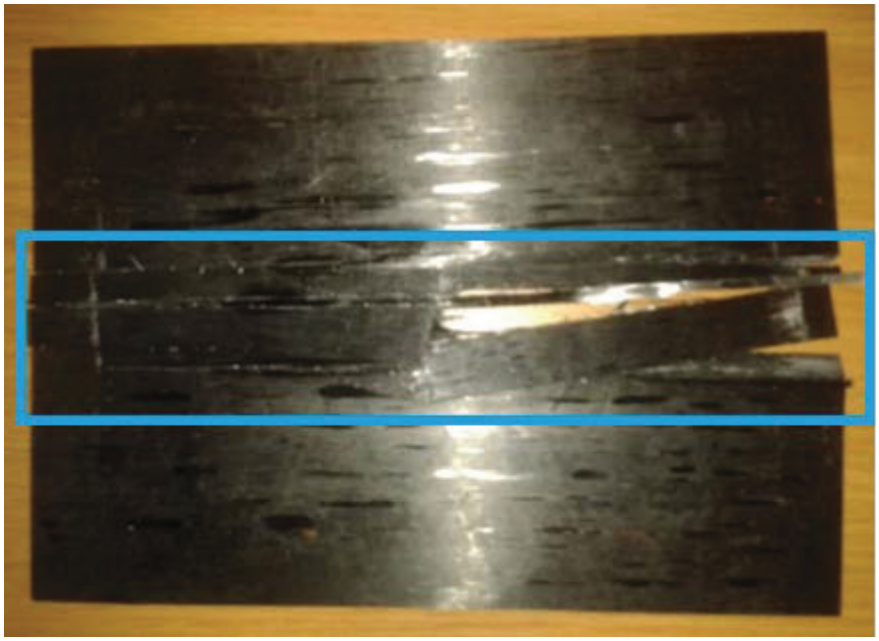

Figure 45: Backside of 0° Uniform Sample Post-Impact With Damaged Region Highlighted

Figure 46: Backside of 45° Symmetrical Sample Post-Impact With Damaged Region Highlighted

Figure 42 and Figure 43 demonstrates the effect that symmetrical stacking vs. continuous stacking has on damage diameter with the symmetrical sample having a slightly larger diameter. As can be seen in images the samples failed catastrophically with fibre breakage focused around the point of impact with some of the back layer fibres snapping at the clamping region.

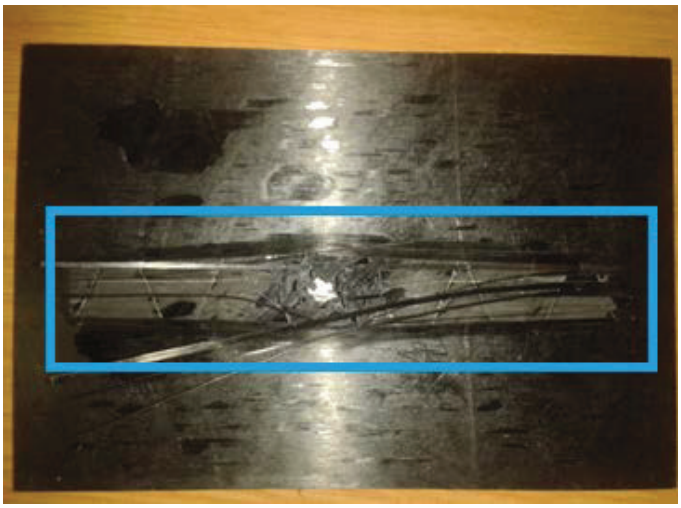

Figure 47: Backside of 45° Continuous Sample Post-Impact With Damaged Region Highlighted

When the failure modes observed in Figure 46 and Figure 47 are compared to the failure modes observed in Figure 32 and Figure 33 from the simulations the similarities and differences are easy to observe. While the simulations did correctly predict the size difference in the puncture holes and that most of the damage would be localized, it failed to predict the extensive damage to the back layers. However they did indicate some failure along the length of the samples.

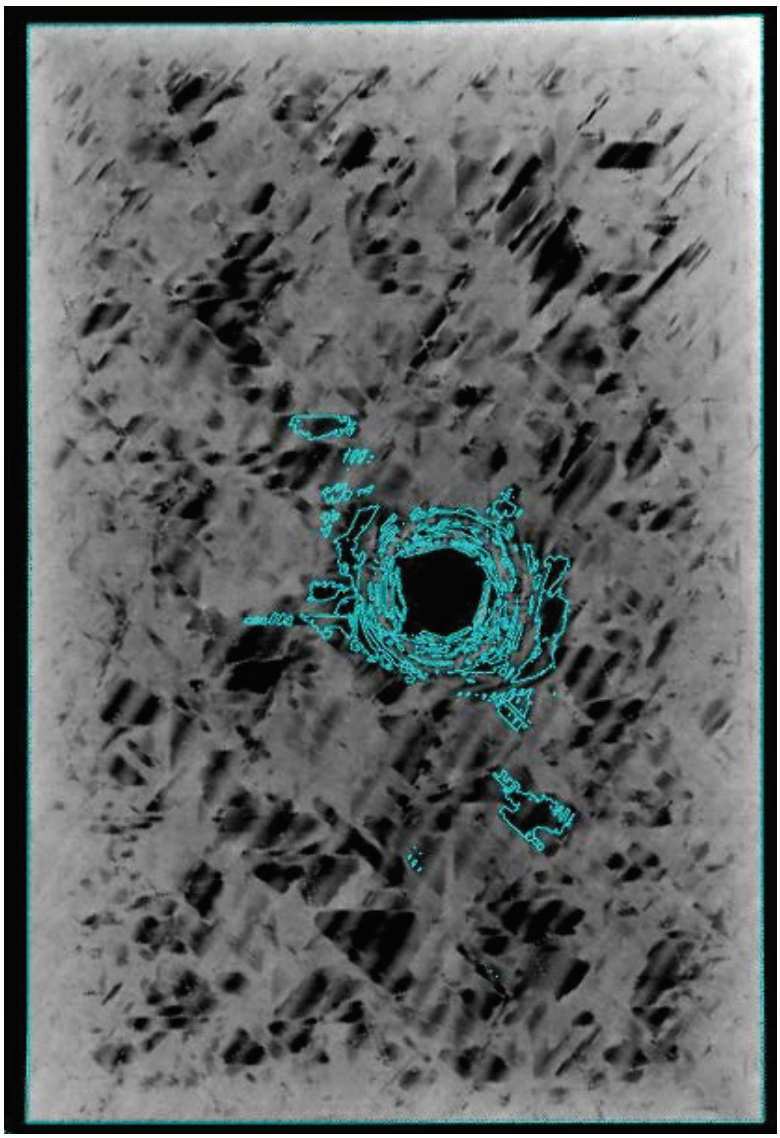

Figure 48: CT Scan of 45° Symmetrical Sample

Figure 48, shown above, is an image taken from a digital 3D representation constructed from a CT scan of a 45° symmetrical sample. The image shown is a section of the sample in a plane parallel to the surface of the sample. The section shown is the representative of the peak internal damage within the sample found at the 11^{th} ply at 2.75 mm from the back. Peak internal damage refers to the damage diameter. The turquoise section shown in the image depicts voids that are connected to the outside atmosphere, thus impact damage that reaches to the surface. When the failure mode observed in Figure 48 is compared to the simulation results as seen in Figure 32 and Figure 33 it can be observed that the CT scan confirms that the internal damage is also highly localised. Additional sections can be seen in Appendix E.1.

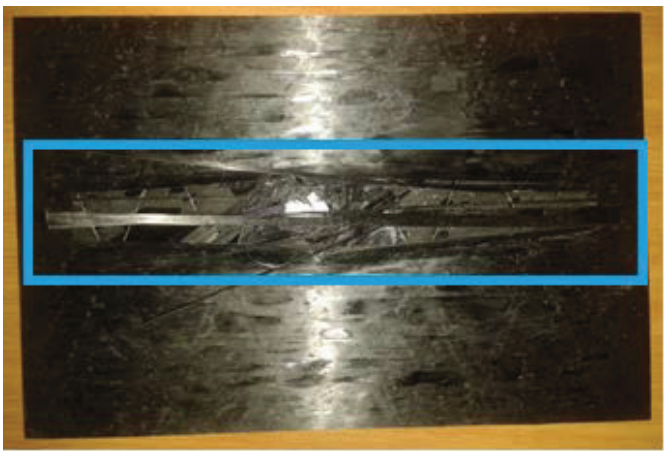

Figure 49: 30° Symmetrical Sample Post-Impact With Damaged Region Highlighted

As can be seen in Figure 49 and Figure 50 the samples failed catastrophically with fibre breakage focused around the point of impact with some of the back layer fibres snapping at the clamping region. Although it should be noted that the back layer damage for the 30° sample sets are significantly reduced when compared to the 45° sample sets. In the 30° sample sets the reduction in the puncture size is visible as well when the symmetrical layup is compared to the continuous layup.

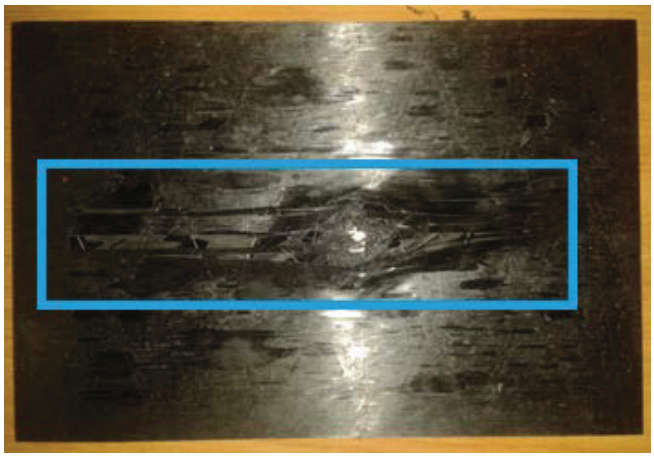

Figure 50: 30° Continuous Sample Post-Impact With Damaged Region Highlighted

When the failure modes observed in Figure 49 and Figure 50 are compared to the failure modes observed in Figure 34 and Figure 35 from the simulations the similarities and differences are easy to observe. The simulations correctly predict the size difference in the puncture holes and that the most of the damage would be localized. They also predicted the slightly extended damage around the impact area which manifested in the back layers. They also indicated some fibre failure along the length of the samples.

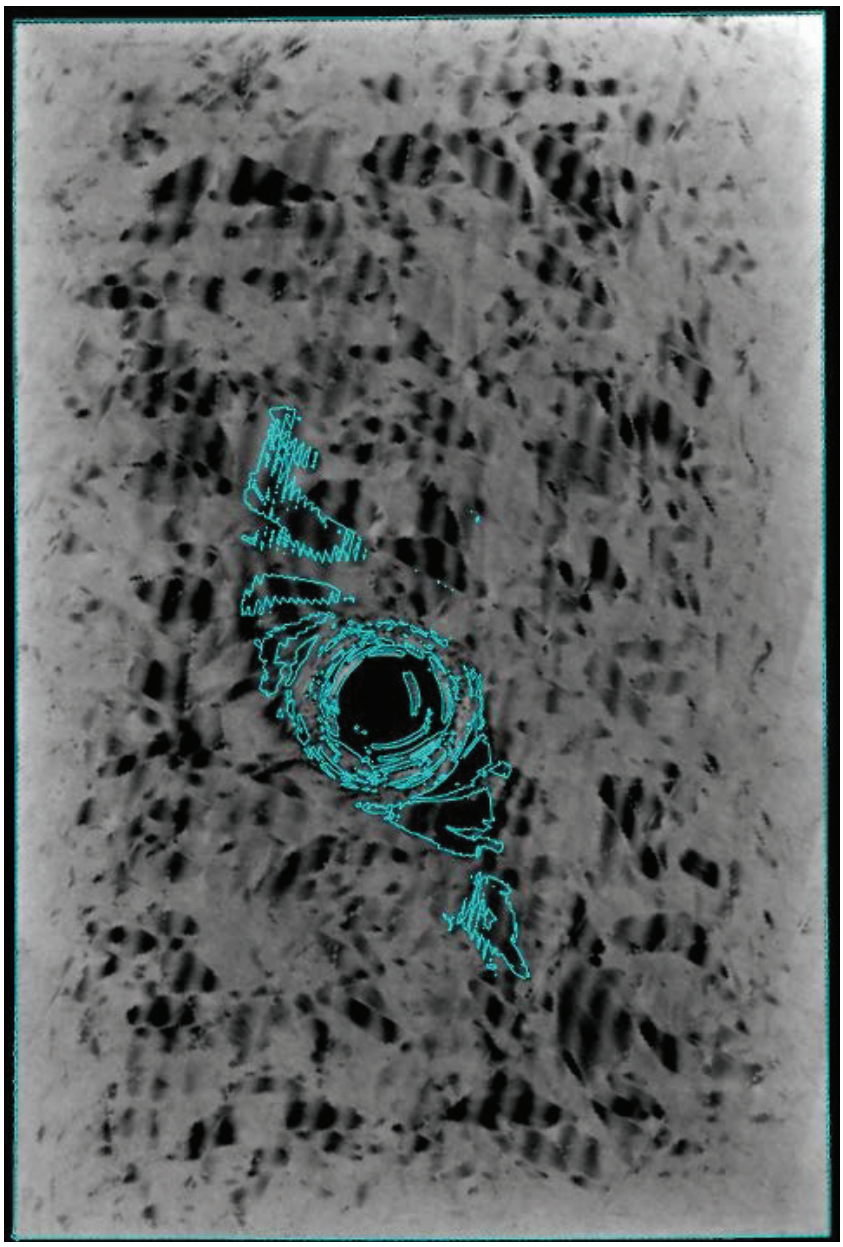

Figure 51: CT Scan of 30° Symmetrical Sample

Figure 51 is a cross-section of a 30° symmetrical. The section shown is the representative of the peak internal damage within the sample found at the 10th ply at 2.5 mm from the back. The turquoise section that depicts impact damage can now be seen rotating along with the fibre orientations although the damage does not extend much further form the impact point. When the failure mode observed in Figure 47 is compared to the simulation results as seen in Figure 34 and Figure 35 it can be observed that the CT scan confirms that the internal damage is less localised than the 45° sample sets. Additional sections can be seen in Appendix E.2.

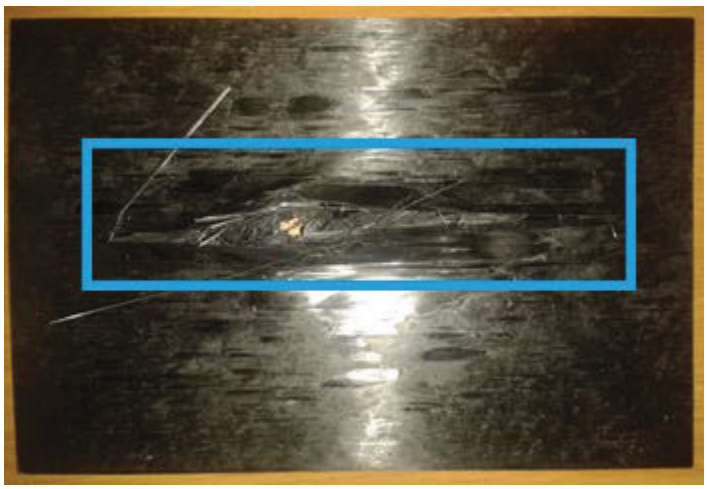

Figure 52: 15° Symmetrical Sample Post-Impact With Damaged Region Highlighted

As can be seen in Figure 52 and Figure 53 although the samples still failed catastrophically with fibre breakage focused around the point of impact the surface damage did not extend as far. Minimal back layer damage was observed when compared to the 30° and 45° sample sets. In the 15° sample sets the reduction in the puncture size is still visible as well when the symmetrical layup is compared to the continuous layup.

Figure 53: 15° Continuous Sample Post-Impact With Damaged Region Highlighted

When the failure modes observed in Figure 52 and Figure 53 are compared to the failure modes observed in Figure 36 and Figure 37 from the simulations there is a significant difference. The simulations indicated significant damage over a larger area for both sample sets and the experimental results proved to have very limited surface damage.

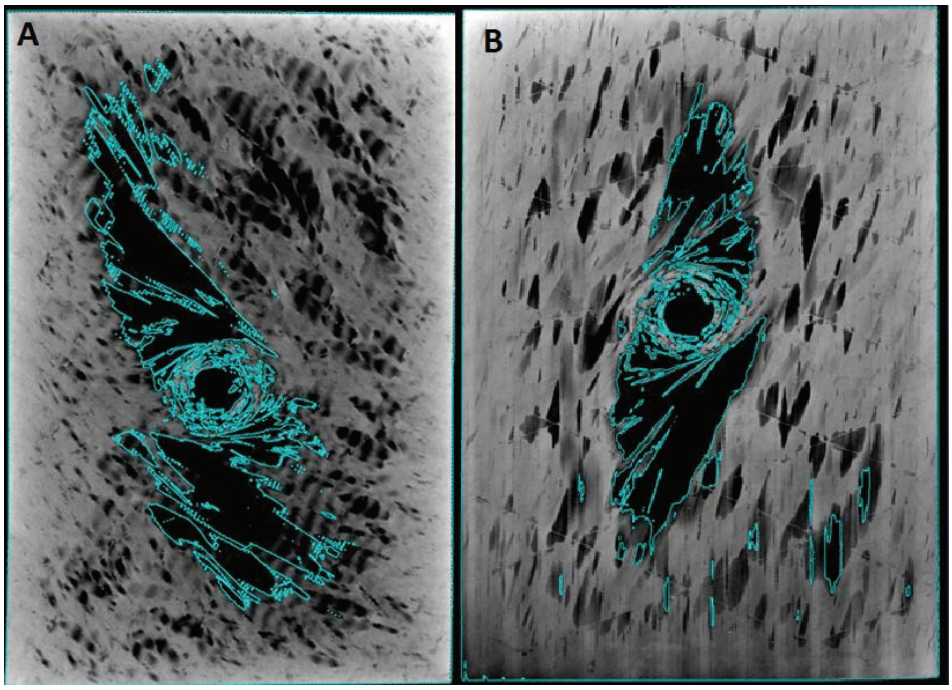

Figure 54: A: CT Scan of 15° Symmetrical Sample B: CT Scan of 15° Continuous Sample

Figure 54A is a cross-section of a 15° symmetrical sample and Figure 54B is a cross-section of a 15° continuous sample. The sections shown are representative of the peak internal damage within each sample found at the 10^{th} ply at 2.5 mm from the back. The turquoise section that depicts impact damage can be seen rotating along with the fibre orientations with highly propagating damage extending much further and wider from the impact point. It is obvious from comparing the internal scan to the external damage that the impact damage is much more extensive than what is visible. When the failure modes observed in Figure 54 is compared to the simulation results as seen in Figure 32 and Figure 33 the CT scan confirms that the internal damage is extensive, although the shape of the failure mode differs from the simulations. Although shapes of the failure modes are nearly identical, their sizes differ with the symmetrical sample exhibiting a larger damage diameter. The simulations indicated that the symmetrical sample should have a smaller damage region than the continuous sample which turned out to not be the case.

Both the 15° sample sets were scanned due to them exhibiting the highest impact resistance and because the 15° continuous set was the only continuous set that did not warp during curing.

Additional sections can be seen in Appendix E.3 and Appendix E.4.

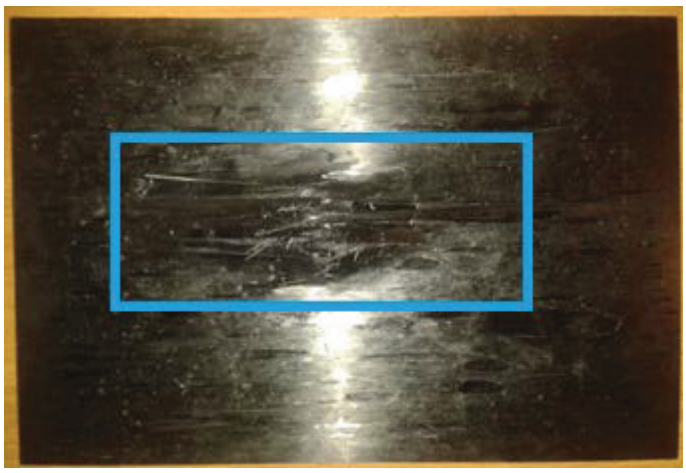

Figure 55: 10° Symmetrical Sample Post-Impact With Damaged Region Highlighted

As can be seen in Figure 55 and Figure 56 although the samples still failed catastrophically with fibre breakage focused around the point of impact the surface damage is significantly lower than any of the other sample sets. Minimal back layer damage was observed when compared to any of the other sample sets. In the 15° sample sets the reduction in the puncture size is still visible as well when the symmetrical layup is compared to the continuous layup.

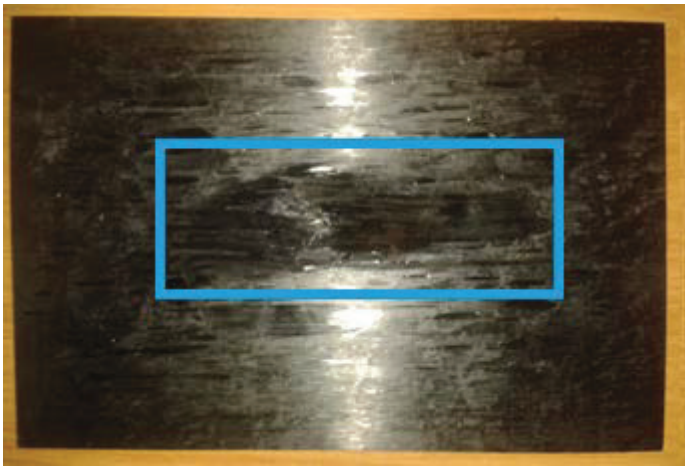

Figure 56: 10° Continuous Sample Post-Impact With Damaged Region Highlighted

When the failure modes observed in Figure 55 and Figure 56 are compared to the failure modes observed in Figure 38 and Figure 39 from the simulations there is a significant difference. While the simulations indicated damage over a larger area for the continuous sample set, it predicted a localized failure for the symmetrical sample set. However the experimental results proved to have limited surface damage for both sample sets.

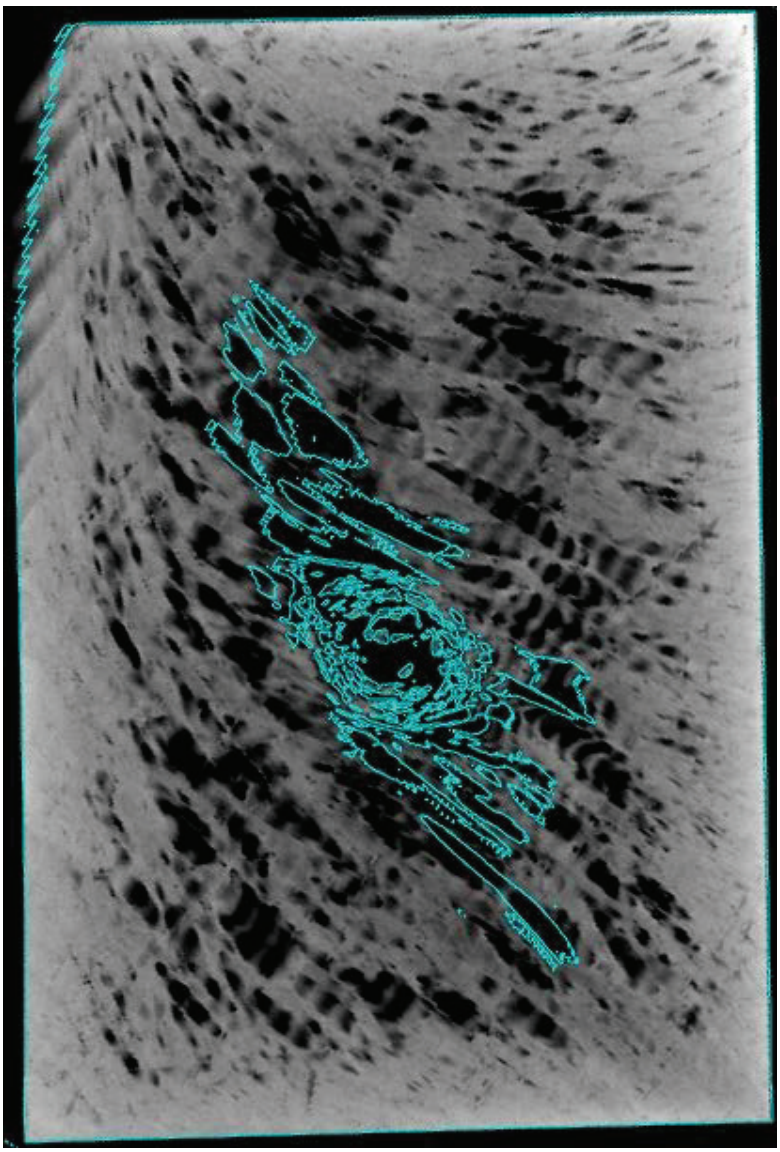

Figure 57: CT Scan of 10° symmetrical sample

Figure 57 is a cross-section of a 10° symmetrical sample. The section shown is the representative of the peak internal damage within the sample found at the 9th ply at 2.25 mm from the back. Although the turquoise section has the same pattern and shape of the crack rotating with the fibres it is smaller than the 15° symmetrical sample's damage. It is obvious from comparing the internal scan to the external damage that the impact damage is much more extensive than that which is visible with the 10° sample sets presenting the least amount of surface damage. When the failure mode observed in Figure 54 is compared to the simulation results as seen in Figure 38 and Figure 39 it can be observed that the CT scan differs from the simulations with regards to the simulations predicting that the symmetrical sample would have highly localised damage. Additional sections can be seen in Appendix E.5.

After evaluating the samples post-impact it was decided that since some of the fibre breakages continued to the clamped area that the measurements across the diameter of the impact damage would be taken across the peak internal damage. The measurements were taken across the largest distance between two opposing turquoise sections visible in Figure 48, 51, 54A, 54B and Figure 57. The results can be seen in the graph in Figure 58.

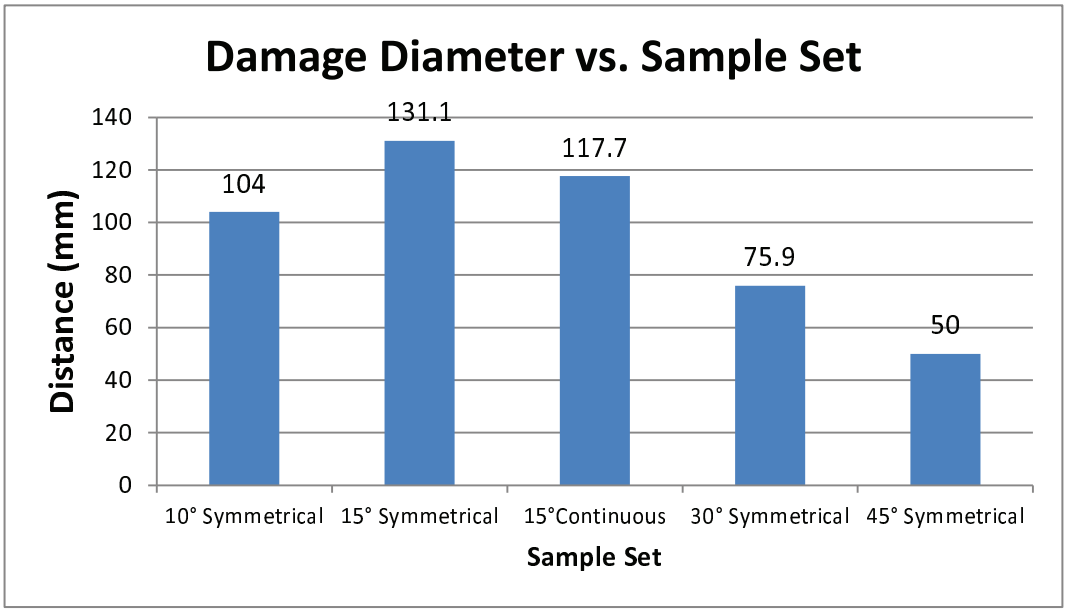

Figure 58: Damage Diameter vs. Sample Set for Unwarped Samples

As can be seen in Figure 58 the 45° sample with the localised damage has the smallest damage diameter. The 30° sample which starts to exhibit rotating crack behaviour has a slightly larger damage diameter. The 15° samples have the largest damage diameter which reaches almost across the entire sample with the symmetrical sample having a slightly larger damage diameter than the continuous sample. However it is not clear whether this is the case for all of the samples in these sample sets. The 10° symmetrical sample has a damage diameter almost as large as the 15° samples due to the similar failure mode. However it has much smaller internal crack propagation than the 15° samples.

5.3 Force History and Energy Absorption

The energy absorption of each sample made was calculated by using equations (9) to (11). Based on this the averages and standard deviations for the sample sets were calculated. Additionally the total number of samples needed to maintain the confidence level was calculated for each sample set. Since some samples were lost during the curing cycle due to loss of vacuum some sample sets contained less than the originally intended 8 samples.

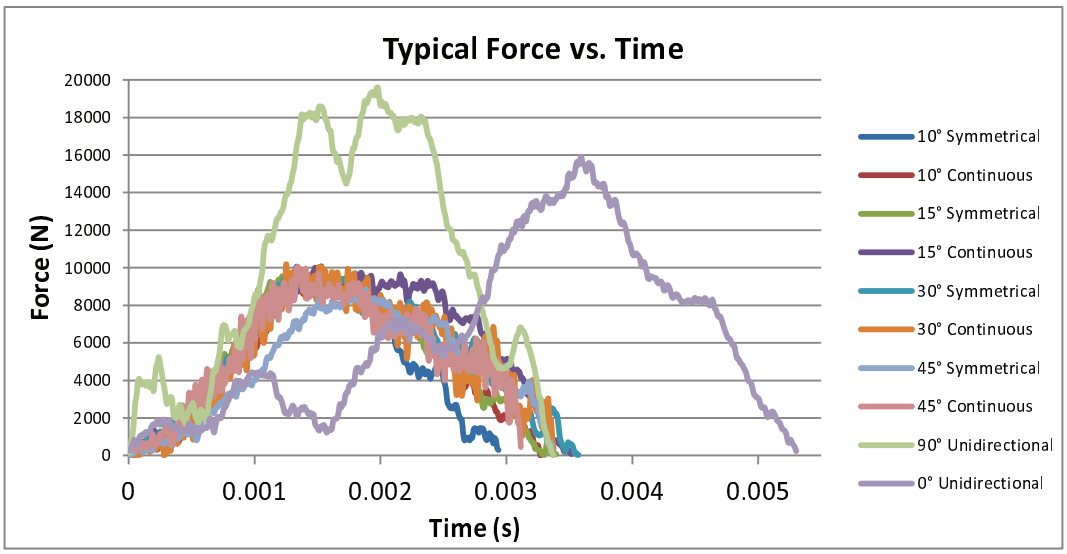

Figure 59: Typical Force vs Time Plot for Each Sample Set

Figure 59 shows an example of a typical force history for each of the different sample sets. As is clearly evident the 0° and 90° differ greatly from the rest of the sample sets due to the different failure mode for these samples. The rest of the sample sets have a similar graph pattern with their impacts ending at roughly the same time. As can be seen the 10° symmetrical plot ends significantly sooner than the rest of the sample sets.

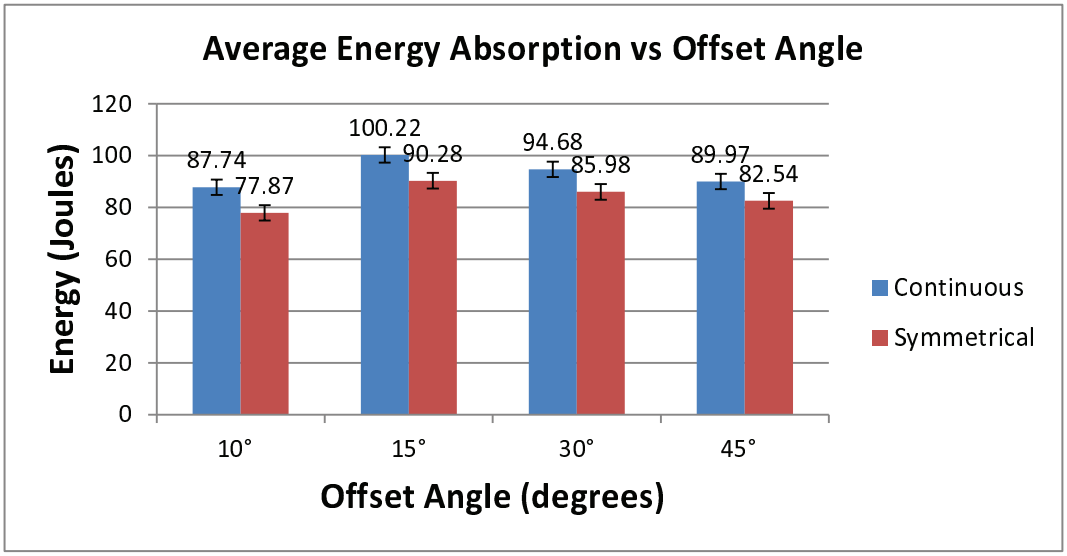

Figure 60: Average Energy Absorption Until Complete Failure vs. Offset Angle.

As can be seen in Figure 60 there is an improvement in energy absorption as the offset angle decreases. The following performance increases can be observed in the symmetrical sets: a 4.2% increase from the 45° set to the 30° set and a 5% increase from the 30° set to the 15° set. This is followed by a sharp drop-off in performance of the 10° set which falls by 15.9% of the 15° set. The sharp drop in performance in the 10° set is unexpected since an increase in properties was expected. However when the energy data is compared to force history data the drop in performance for the 10° symmetrical sample set is likely due to its significantly shorter impact duration. A similar effect was found by Grunenfelder in their experiments where a small offset angle actually resulted in a loss of performance. [49] They attributed the loss of performance to experimental factors the most important being sample dimensions which allow the cracks to reach the edge of the samples and allowing additional failure modes. However the experiments in this project exhibited a different response. On all except the 10° sample sets the cracks reached the boundary of the clamp at which point it was stopped and some fibres in the back layer would break.

A similar performance trend can be seen in the continuous sample sets as in the symmetric sample sets. The 30° set a has a 5.2% performance increase over the 45° set and the 15° set has a 5.4% performance increase over the 30° set. As with the symmetrical set a performance drop-off of 13.7% is observed from the 15° set to the 10° set.

Comparing the results of the symmetrical samples to the continuous samples with the same angle offsets found that the continuous sample sets consistently absorbed more energy than the symmetric samples. The following performance increases were observed:

- for the 45° offset angle a 9% increase;
- for the 30° offset angle a 10%% increase
- For the 15° offset angle a 11% increase
- For the 10° offset angle a 13% increase

The performance increases observed from making the samples continuous as opposed to symmetrical are significantly larger than those observed from decreasing the offset angle.

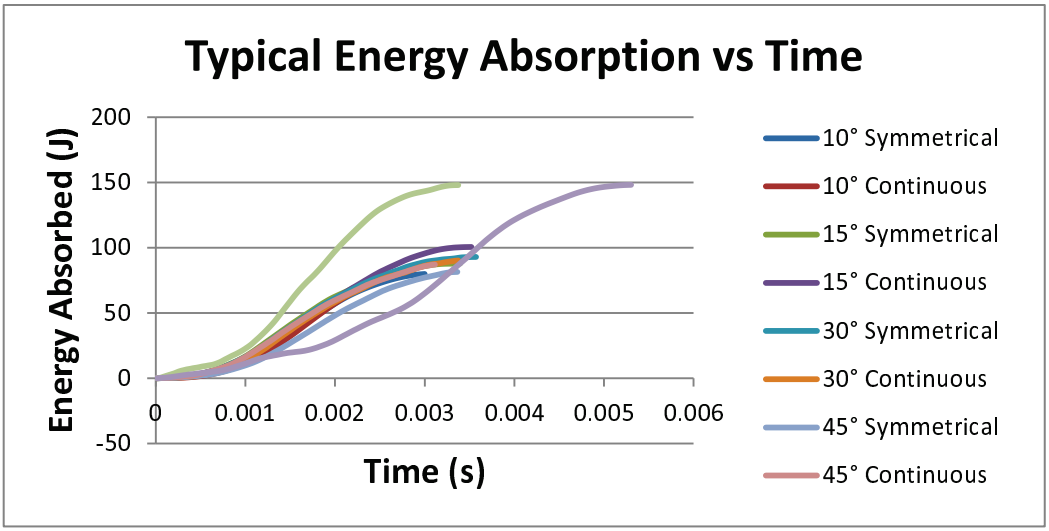

Figure 61: Typical Energy Absorbed vs Time Plot for Each Sample Set

As can be seen in Figure 61 almost all of the sample sets follow a similar trend for energy absorption with only small difference in the shape of their graphs. The 90° and 0° sample sets have a much different graph pattern due to the different failure mode of the samples.

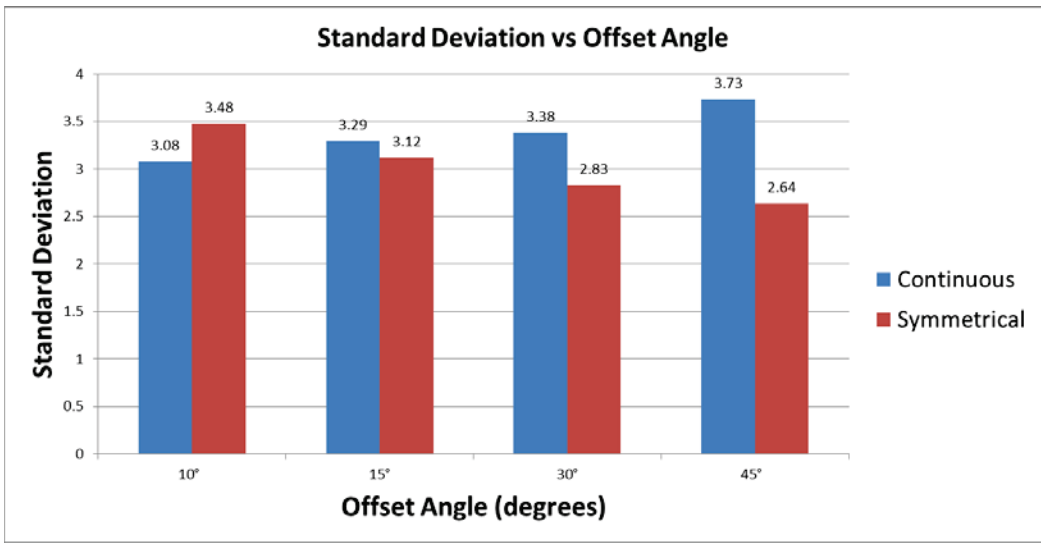

Figure 62: Standard Deviation vs. Offset Angle

The data acquired from calculating the energy absorption for each sample tested was then used to calculate the standard deviation of each sample set by using equation 4 with the results shown in Figure 62. As can be seen the standard deviations are fairly consistent with the symmetrical samples having slightly lower values than the continuous samples. This could be caused by the effect of warpage for the 10°, 30° and 45° sets since the 15° set has nearly identical values.

However with the standard deviations being so close to each other it could simply be due to insufficient data.

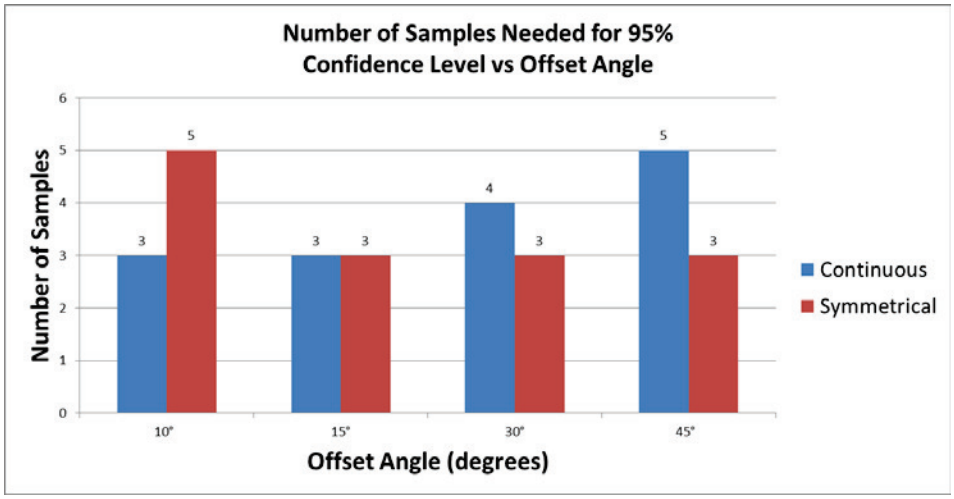

Figure 63: Minimum Number of Samples Needed in Order to Maintain a Confidence Level of 95% and a Margin of Error of 4%

From the standard deviations calculated as well as the margin of error determined for each sample set as 4% and the confidence level of 95% the minimum number of samples needed were calculated for each sample set by using equation 5. Since all of the sample sets already had more samples than were minimally required no further samples were tested.

In Sevkat et al.'s similar experiments, albeit with different material types and varying impact velocities; the energy absorption of almost all of the samples for the impact velocities of 4.8 m/s and 6.3 m/s was in the range of 60J to 100J. One of the 6.3m/s sample sets did reach 120J. When the results of this project are compared to those of Sevkat et al, it can be seen that they are the same order of magnitude. [22]

Soliman et al. also performed similar experiments with carbon fibre composite materials although they used a thickness of 2.7 mm for their samples and got energy absorption of roughly 30 J for the 120 J impact. However when this value is adjusted for thickness it is the same order of magnitude as the those of Sevkat et al's data and those of this project. [50] [22]

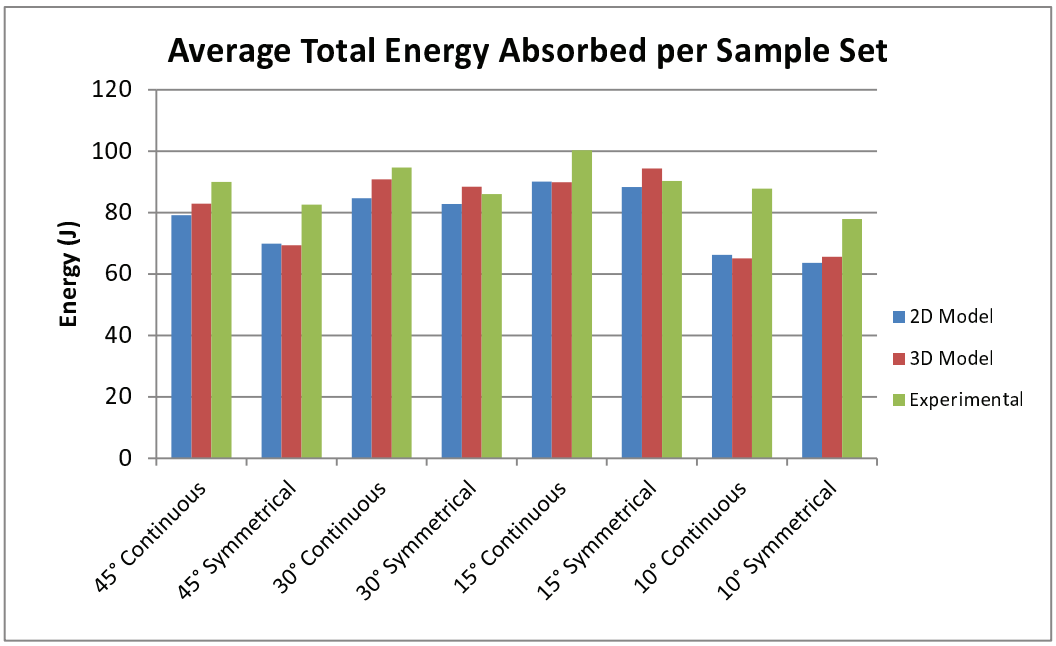

Figure 64: Average Total Energy Absorbed for Each Sample Set

As can be seen in Figure 64 both the simulations sets tended to under predict the energy absorption for nearly all of the sample sets to varying degrees except for the 15° and 30° symmetrical sets where the three dimensional model slightly over predicted the values. The two dimensional model was able to predict the trends in performance between different offset angles and symmetrical vs. continuous samples, albeit with small values at times. The three dimensional model was able to predict the trend in performance between the different offset angles. However it was not capable of predicting the performance trend for the 10° and 15° sets for symmetrical vs. continuous.

6. CONCLUSIONS AND RECOMMENDATIONS

6.1 Conclusions

After investigating the characteristics of the biological hammer of the mantis shrimp several strengthening characteristics were identified. The two major characteristics that were investigated were the difference in offset angle and the difference enforcing symmetry vs. creating a continuous sample.

The first priority was to establish that fibre length did not influence the impact resistance of the composite. Thus 90° uniform samples were compared to 0° uniform samples with results obtained from the experiments establishing that fibre length does not affect the impact resistance of the composite.

Following this samples sets with different offset angles were evaluated for their impact resistance. It was found that the smaller the offset angle, the higher the impact resistance with the values peaking at 15°. The 10° sample sets were observed to have the lowest impact resistance of all the sets; however this could be attributed to experimental factors.

Sample sets with continuous offset angles were prepared as well in order to compare them with the performance of the symmetrical sample sets as well as to determine whether a non-symmetrical layup without warpage is possible. All of the continuous sample sets warped with the exception of the 15° set. Additionally it was found that the continuous sample sets consistently outperformed the symmetrical sample sets by at least 10%. The same trend in increased impact resistance with a smaller offset angle was observed in the continuous sample sets.

The trends in performance mentioned above were correctly indicated by the simulation models in spite of the fact that the simulations underestimated the impact resistance of the materials by a small amount. While the failure modes the simulations predicted did not match the surface damage of the samples, they were correlated by the CT scans performed on the samples.

CT scans of the samples led to the discovery of the actual failure modes of the samples. The 45° sample had minimal internal damage compared to the external damage. The 30° sample had slightly more internal damage compared to the 45° with some crack rotation visible on the scans. The 15° samples however had massive internal damage with rotating cracks and delamination regions stretching across the entire diagonal of the samples from the one clamped region to the other. Thus the impact energy is spread across a much larger area. This characteristic is possibly the reason for it having the largest impact resistance. The 10° sample has a similar failure mode as the 15° set however it is on a much smaller scale with the cracks never reaching the boundary of the clamp. Whether the absence of contact with clamp boundary has an effect on the impact resistance of the sample is unknown, however all of the other samples which did have cracks reach the clamp boundary had a higher impact resistance.

6.2 Recommendations

Although decreasing the offset angle and making the sample continuous increases the impact resistance, they are not the only components responsible for the incredible impact resistance of the mantis shrimp's biological hammer. Future projects could evaluate the remaining characteristics which include: Decreasing levels of hardness throughout the composite, the effect of modulus mismatch in impact resistance and if possible the effect the oscillating hardness level. An additional point of interest could be the effect of using the same fibre material with different matrix properties, different epoxies, for the impact surface and internal regions as compared to changing the fibre material but keeping the matrix properties consistent.

Due to the fact that the biological hammer's structure can withstand impact and blast forces it is a possibility that if all of the structure's characteristics can be reproduced for composites that a composite material could be produced capable of withstanding impact and blast forces. Normally blast and impact resistance have opposite design considerations thus the potential value of developing a composite capable of withstanding both force types cannot be overstated. This would be even more valuable if the resulting composite is light weight.

7. REFERENCES

[1] N. E. Dowling, *Mechanical Behavior of Materials* Prentice Hall, NJ, ed. 3, 2006.

[2] J.C. Weaver, G.W.Milliron, A. Miserez, K.E. Lutterodt, S. Herrera, I. Gallana, W.J. Mershon, B.Swanson, P. Zavattieri, E. DiMasi, D. Kisailus, *The Stomatopod Dactyl Club: A Formidable Damage-Tolerant Biological Hammer,* Science, 2012, 336, 1275

[3] S.N. Patek. W.L. Korff, R.L. Caldwell, *Deadly strike mechanism of a mantis shrimp.* Nature, 2004, 428,819.

[4] S. N. Patek, R. L. Caldwell, *Extreme impact and cavitation forces of a biological hammer: Strike forces of the peacock mantis shrimp Odontodactylus scyllarus*. J. Exp. Biol, 2005, 208, 3655.

[5] T. Apichattrabrut, K. Ravi-Chandar, *Helicoidal composites*. Mech. Adv. Mater. Structures, 2006, 13, 61.

[6] J. R. A. Taylor, S. N. Patek, *Ritualized fighting and biological armor: The impact mechanics of the mantis shrimp's telson.* J. Exp. Biol, 2010, 213, 3496.

[7] P. Fratzl, H. S. Gupta, F. D. Fisher, O. Kolednik, *Hindered crack propagation in materials with periodically varying young's modulus—lessons from biological materials*. Adv. Mater, 2007, 19, 2657

[8] H. Ming-Yuan, J. W. Hutchinson,, *Crack deflection at an interface between dissimilar elastic materials*, International. Journal of Solids Structures, 1989, 25, 1053

[9] M.F. Ashby, Technology of the 1990's: *Advanced materials and predictive design*. Philosophical Transactions of the Royal Society of London, 1987, A322, 393-407.

[10] A.A. Griffith, *The phenomena of rupture and flow in solids,* Philosophical Transactions of the Royal Society, 1920, 221A, 163-198.

[11] J.E. Gordon, *The New Science of Strong Materials,* 2nd , Princeton University Press, Princeton, NJ, 1976

[12] D. Qian, J.G. Wagner, W.K. Liu, M.F. Yu and R.S. Ruoff, *Mechanics of carbon nanotubes,* Applied Mechanics Reviews, 2002, 55(6), 495-533.

[13] E.R. Thostenson, Z. Ren, T.W. Chou, *Advances in the science and technology of carbon nanotubes and their composites: A review.* Composites Science and Technology, 2001, 61, 1899-1912.

[14] R.F. Gibson, *Principles of Composite Material Mechanics*, Third Edition. CRC Press, Florida, 2011.

[15] A. Matzenmiller, J. Lunliner, R.L. Taylor, *A constitutive model for anistropic damage in fiber-composites*. Mechanics of Materials 20 (1995), p. 125-152, 1995.

[16] K. Schweizerhof, K. Weimar., Th. Munz, Th. Rottner, *Crashworthiness Analysis with Enhanced Composite Material Models in LS-DYNA - Merits and Limits*. LS-DYNA World Conference, Michigan, 1998.

[17] R.T. Schwartz, H.S. Schwartz, and Department of United States Air Force Materials Laboratory, Nonmetallic Materials Division, *Fundamental aspects of fiber reinforced plastic composites*, Interscience Publishers, Ohio, 1968.

[18] Z. Hashin, *Failure criteria for unidirectional fiber composites*. Journal of Applied Mechanics, 47: p. 329, 1980.

[19] T. Xiaodong, S. Zhen, C. Puhui, M. Gaedke , et al., *Methodology for residual strength of damaged laminated composites*, American Institute of Aeronautics and Astronautics, p: 1061, 1997.

[20] S.P. Rajbhandari, M.L. Scott, R.S. Thomson, D. Hachenberg, *An approach to modelling and predicting impact damage in composite structures.* ICAS 2002 Congress, Germany, 2002.

[21] X. Zhang, *Impact damage in composite aircraft structures-experimental testing and numerical simulation*. Proceedings of the Institution of Mechanical Engineers, Journal of Aerospace Engineering, 212(4): p. 245-259, 1998.

[22] E. Sevkat, B. Liaw, F. Delale, B.B Raju,*Drop-weight impact of plain-woven hybrid glass-graphite/toughened epoxy composites,* Composites: Part A 40 (2009), p. 1090-1110, 2009.

[23] C. Bouvet, B. Castanie, M. Bizeul, J.J. Barrau, *Low velocity impact modelling in laminate composite panels with discrete interface elements,* international Journal of Solids and Structures 46(15), p.2809-2821, 2009

[24] S. Heimbs, S. Heller, P. Middendorf, F. Hahnel, J. Weibe, *Low velocity impact on CFRP plates with compressive preload: Test and modelling,* International Journal of Impact Engineering 36(11), p.1182-1193, 2009.

[25] M. Aktas, C.Atas, B.M. Icten, R. Karakuzu, *An experimental investigation of the impact response of composite laminates,* Composite Structures 87(4), p.307-313, 2009

[26] M. Aktas, C.Atas, R. Karakuzu, Y. Arman, *Compression-after impact behavior of laminated composite plates subjected to low velocity impact in high temperatures*, Composite Structures 89(1), p.77-82, 2009

[27] R. D. Cook, D.S. Malkus, M.E. Plesha, R.J. Witt, *Concepts And Applications of Finite Element Analysis*, Fourth Edition. John Wiley & Sons Inc., University of Wisconsin, Madison, 2001.

[28] L. Iannucci, M.L. Willows, *An energy based damage mechanics approach to modelling impact onto woven composite materials* - Part 1: Numerical models. Composites: Part A 37, p. 2041-2056, 2006.

[29] L. Iannucci, *Progressive failure modelling of woven carbon composite under impact*. International Journal of Impact Engineering 32, p. 1013-1043, 2004

[30] ASTM D7136/D 7136M – 05, *Standard Test Method for Measuring the Damage Resistance of a Fiber-Reinforced Polymer Matrix Composite to a Drop-Weight Impact Event*, 2005

[31] HBM, *QuantumX MX410B - 4-channel, Highly Dynamic Universal Amplifier*, http://www.hbm.com/en/2133/quantumx-mx410b-4-channel-highly-dynamic-amplifier/ (accessed 13 February 2015).

[32] J. Tomblin, Y.C. Ng, K.S. Raju, DOT/FAA/AR-03/19, *Material Qualification and Equivalency for Polymer Matrix Composite Material Systems: Updated Procedure*, office of Aviation Research Washington, 2003.

[33] M.F. Triola, *Elementary Statistics*, 12th, Pearson Education Inc, New York, 2012.

[34] A.K. Kaw, *Mechanics of Composite Materials*, 2nd, Taylor & Francis Group, Florida, 2006.

[35] B. Wade, P. Feraboli, M. Osborne, *Simulating laminated composites using LS-DYNA material model MAT54 part I: [0] and [90] ply single-element investigation*, Joint Advanced Materials & Structures Center of Excellence 2012 Technical Review Meeting, 98195-2400, 2012.

[36] L.P. Kollár, G.S. Springer, *Mechanics of Composite Structures*, Cambridge University Press, Cambridge, 2003.

[37] M. De Freitas, L Reis, *Failure mechanisms on composite specimens subject to compression after impact*, Composite Structures, 1998, 42, 365-373

[38] P.D. Soden, A.S. Kaddour, M.J. Hinton. *Recommendations for designers and researchers resulting from the world-wide failure exercise*. Comp Sci Technol, 2004, 64, 589-604.

[39] Wichita State University, Composite Materials Handbook (CMH-17) Volume 3, Rev. G, SAE International, 2012.

[40] A. Matzenmiller, K. Schweizerhof, *Crashworthiness Simulations of Composite Structures- a first Step with Explicit Time Integration*, Nonlinear Computational Mechanics- A State of the Art, 1991.

[41] A.F. Johnson, A.K. Pickett, *Impact and crash modeling of composite structures: A challenge for damage mechanics*. European Conference on Computational Mechanics, ECCM'99, Germany, 1999.

[42] J.F.M. Wiggenraad, *Crashworthiness research at NLR: 1990-2003*. National Aerospace Laboratory, Netherlands, 2003.

[43] A.K. Pickett, T. Pyttel, F. Payen, F. Lauro, N. Petrinic, H. Werner, J. Christlein, *Failure prediction for advanced crashworthiness of transportation vehicles*. International Journal of Impact Engineering, 2004, 30, 853-872.

[44] A. Byar. *A modern aerospace modeling approach for evaluation of aircraft fuselage crashworthiness,* International Journal of Crashworthiness, 2003, 8(4), 401-413.

[45] P. Feraboli, F. Deleo, B. Wade, M. Rassaian, M. Higgins, A. Byar, M. Reggiani, A. Bonfatti, L. DeOto, A. Masini, *Predictive modeling of an energy-absorbing sandwich structural concept using the building block approach*. Composites: Part A, 2010, 41, 774-786.

[46] J. Gabrys, J. Schatz, K. Carney, M. Melis, E. Fasanella, K. Lyle, *The use of LS-DYNA in the Columbia accident investigation and Return to Flight activities*. 8th International LS-DYNA Users Conference, Detroit MI, 2004.

[47] K.E. Jackson, E.L. Fasanella. *Development of an LS-DYNA model of an ATR42-300 aircraft for crash simulation*. 8th International LS-DYNA Users Conference, Detroit MI, 2004.

[48] P. Feraboli, F. Deleo, B. Wade, M. Rassaian, M. Higgins, A. Byar, M. Reggiani, A. Bonfatti, L. DeOto, A. Masini, *Predictive modeling of an energy-absorbing sandwich structural concept using the building block approach*. Composites: Part A 41,p. 774-786 , 2010.

[49] L. Grunenfelder, N. Suksangpanya, C. Salinas, G. Milliron, N. Yaraghi, S. Herrera, K. Evans-Lutterodt, S. Nutt, P. Zavattieri, D. Kisailus, *Bio-inspired impaCT resistant composites*, Acta Biomaterialia, 10, 3997-4008, 2014.

[50] E.M. Soliman, M.P. Sheyka, M.R. Taha, *Low velocity impact of thin woven carbon fabric composites incorporating multi-walled carbon nanotubes*, International Journal of Impact Engineering, 45, p. 39-47. 2012

APPENDIX A: TEST SETUP DESIGN

A.1: Baseplate

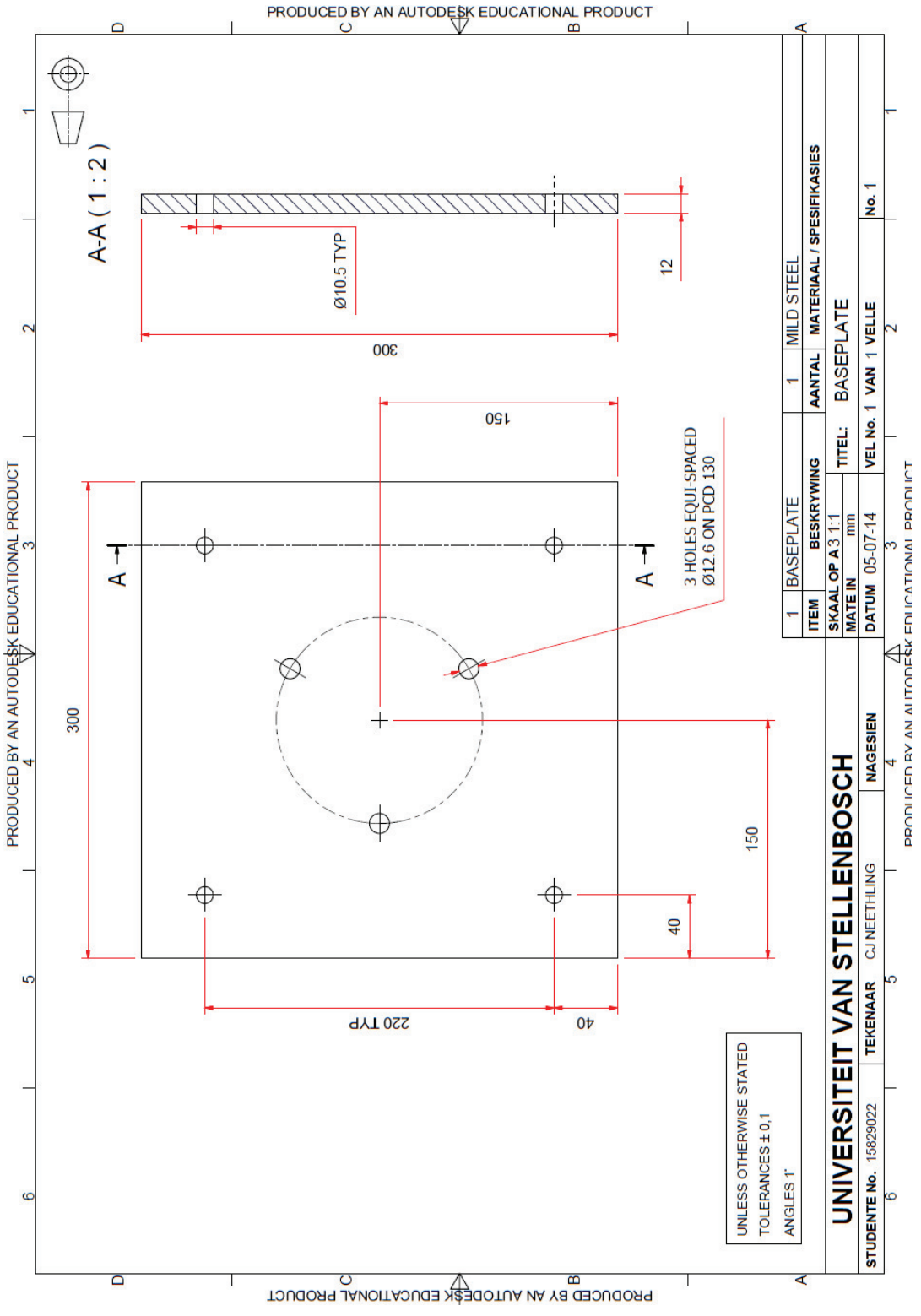

A.2: Clamp

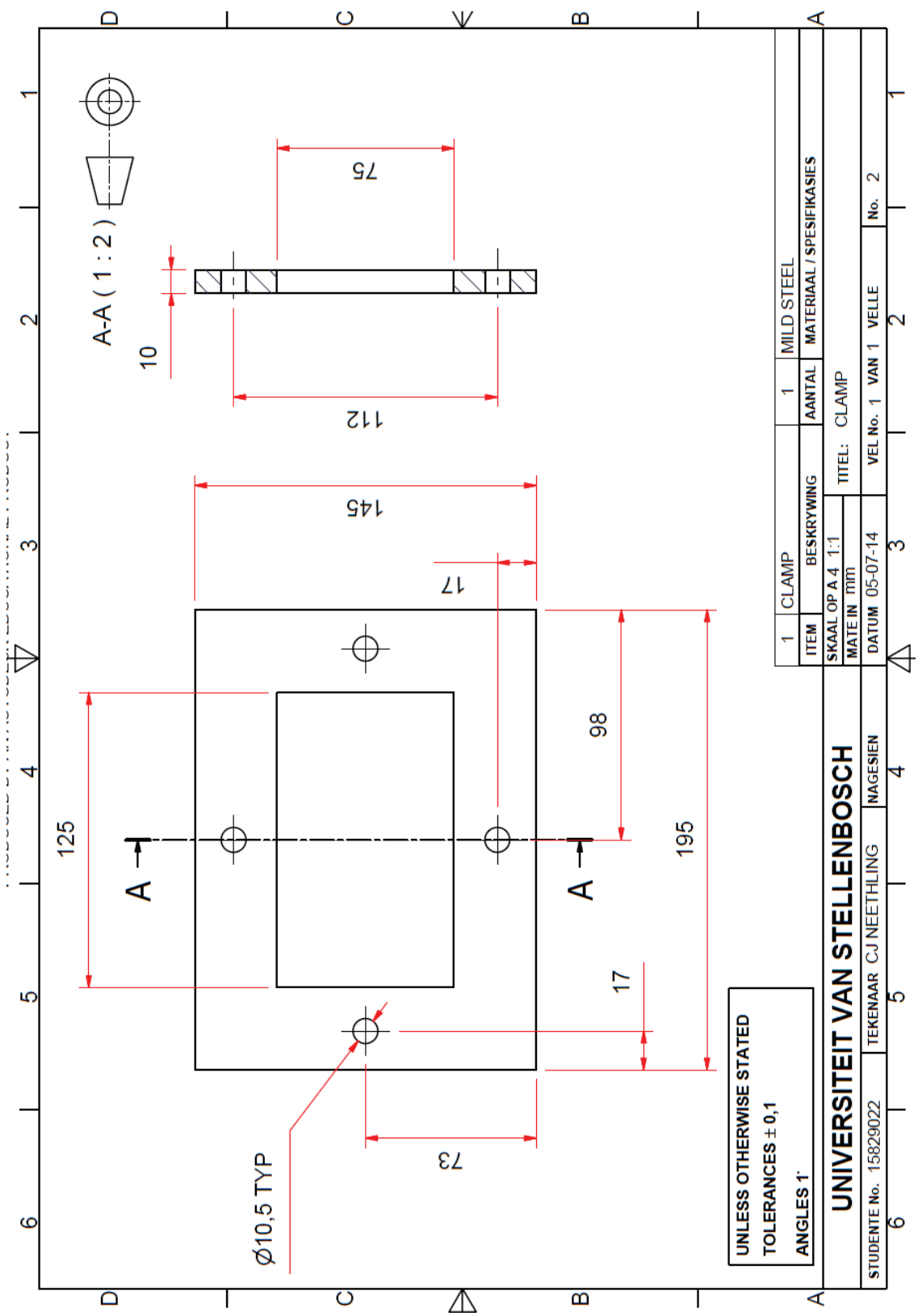

A.3: Impact Fixture

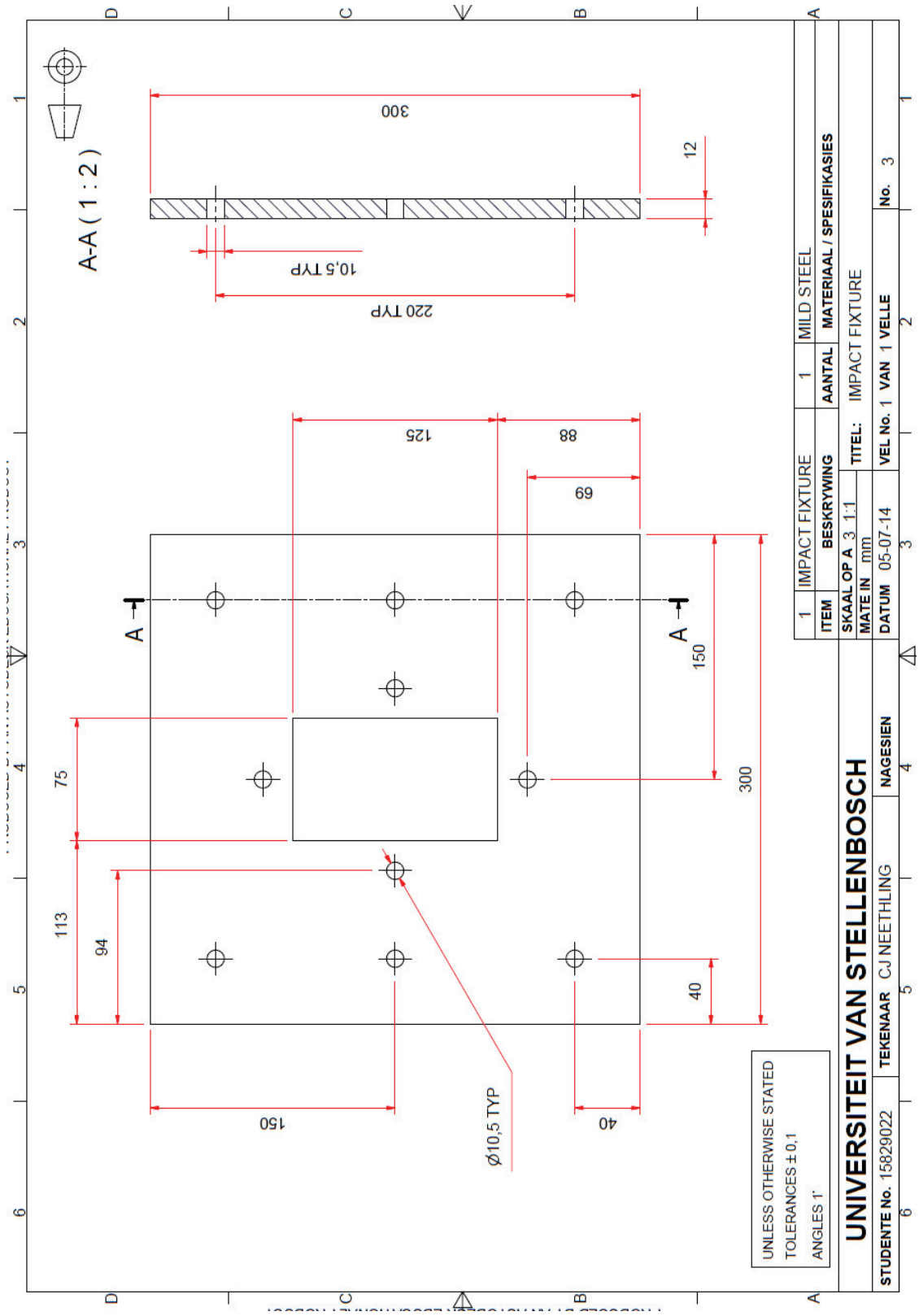

A.4: Support

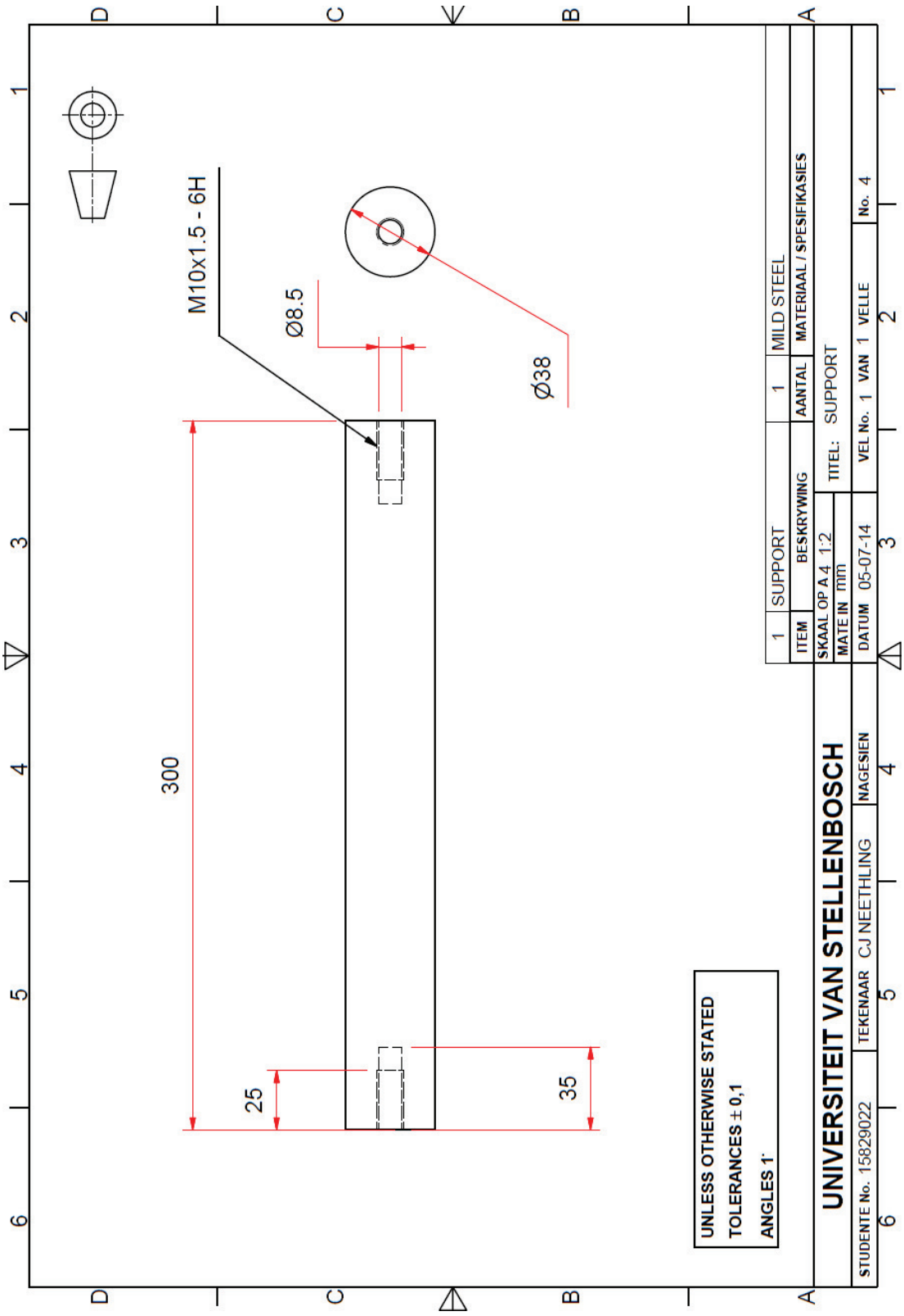

A.5: Assembly

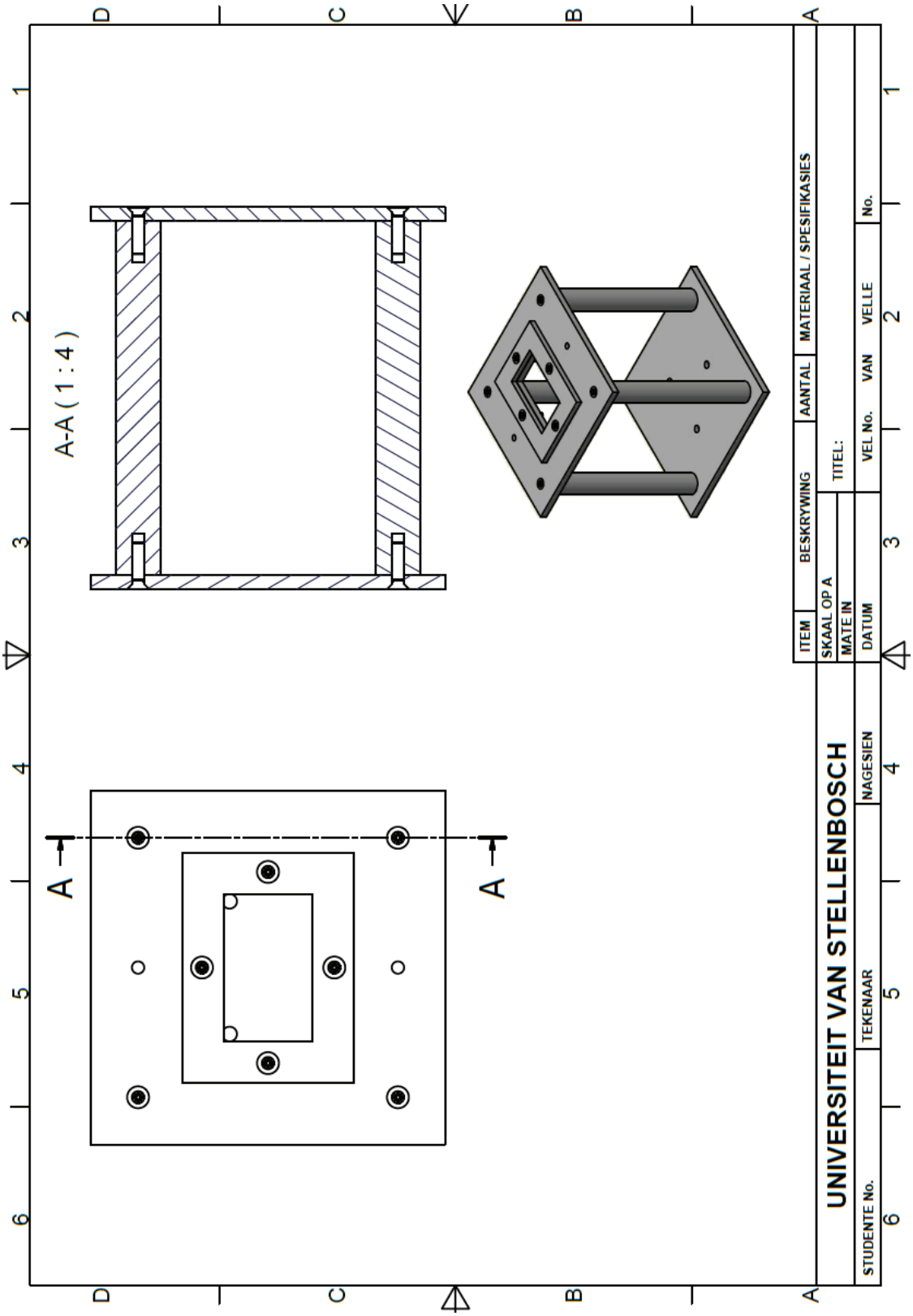

APPENDIX B: DATA ACQUISITION EQUIPMENT

B.1: C6A Loadcell Data Sheet

Data Sheet

C6A

Force Transducer

Special features

- Compressive force transducer
- Nominal forces 200 kN ... 5 MN
- Continuous inner bore for nominal forces from 200 kN to 2 MN
- Rust-resistant version for 200 kN and 500 kN nominal forces
- Extensive mounting accessories

Dimensions (in mm; 1 mm= 0.03937 inches)

C6A[1], nominal forces 200 kN...2 MN

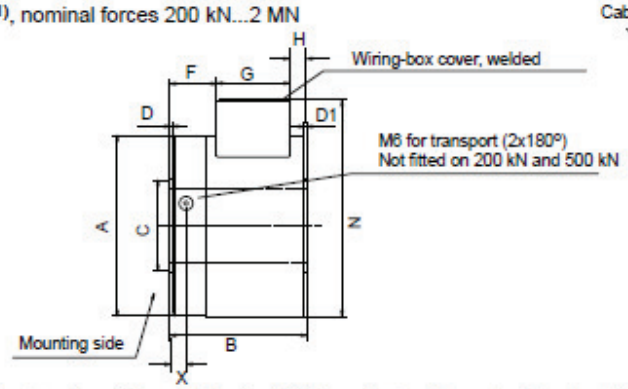

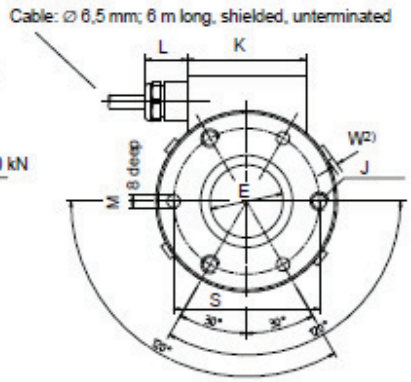

1) Force transducers for nominal loads ≤ 500kN, manufactured from rust-resistent material

2) For 1 MN and 2 MN only

Nominal forces	A	B	C ±0.1	D	D1	E+0.1	F	G	H	J	K	L	M H11	N	S ±0.1	W	X
200 kN	80	60	40.4	1	1	32	19.5	32.5	8	M8 - 8 deep	53	18.5	6	97.5	64	–	–
500 kN	80	60	52	1	1	32	19.5	32.5	8	M8 - 8 deep	53	18.5	6	97.5	64	–	–
1 MN	168	100	88	2	3	68	29	43	28	M12 - 15 deep	50	35	8	200	130	1	10
2 MN	168	100	106	2	3	68	29	43	28	M12 - 15 deep	50	35	8	200	130	1	10

B0635-2.3 en

HBM

Dimensions continued (in mm)

C6A, nominal force 5 MN

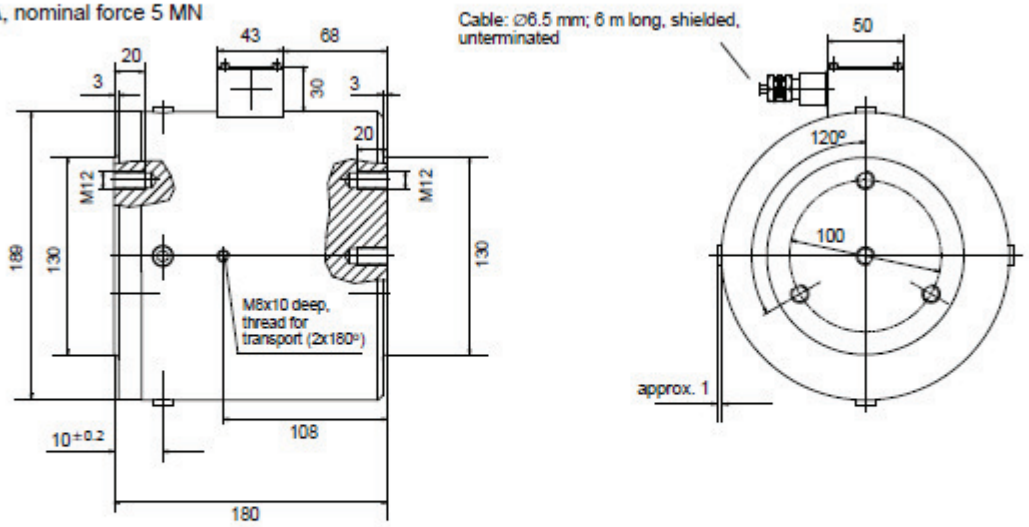

Mounting accessories

Spherical cap ZK (Compensation by oblique load introduction)

for nominal forces in range 200 kN...2 MN

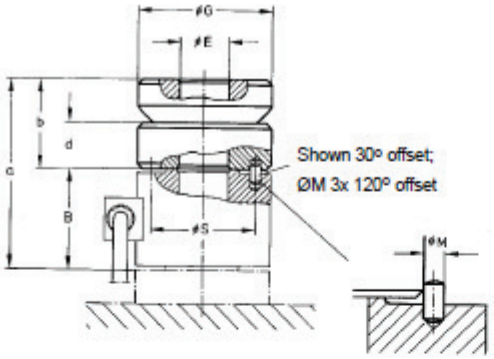

for 5 MN nominal forces

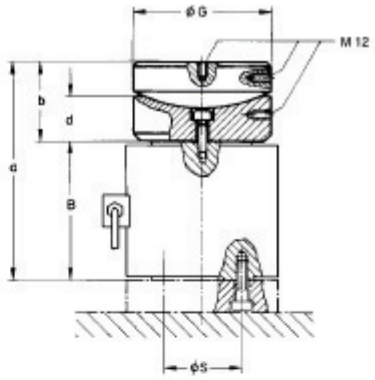

Nominal forces	ZK order no.	Weight in kg	B	$E^{+0.1}$	G	M_{h11}	s	a	b	d
200...500 kN	1-C6/50T/ZK	1.7	60	32	$82_{-0.2}$	6	64 ± 0.1	112	52	28
1 MN	1-C6/100T/ZK	3.8	100	68	$121.5_{-0.2}$	8	130 ± 0.1	175	74.5	40
2 MN	1-C6/200T/ZK	11.6	100	68	$159_{-0.2}$	8	130 ± 0.1	195	95	50
5 MN	1-C6/500T/ZK	20.6	180	–	$178_{-0.3}$	–	100	284	103	61

Mounting accessories continued

Load button ZL (for high-precision measurement)

for nominal forces in range 200 kN... 2 MN

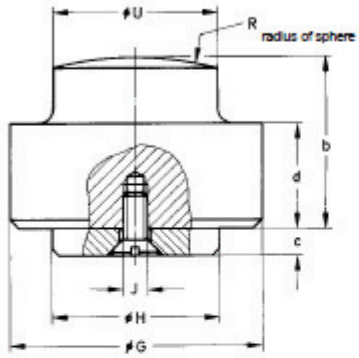

for 5 MN nominal forces

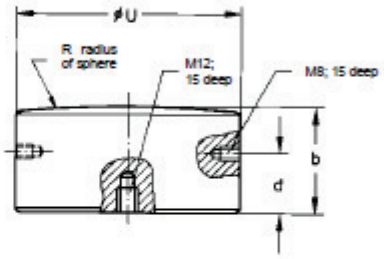

Nominal forces	ZL order no.	Weight in kg	G	H$_{-0.1}$	J	R	U$_{-0.2}$	b	c	d
200 kN	1-C6/20T/ZL	0.8	60	31.9	M5	300	32	45	5	30
500 kN	1-C6/50T/ZL	0.8	60	31.9	M5	300	44	45	5	30
1 MN	1-C6/100T/ZL	6.4	120	67.9	M8	600	64	80	8	60
2 MN	1-C6/200T/ZL	6.8	120	67.9	M8	600	85	80	8	60
5 MN	1-C6/500T/ZL	6.5	–	–	–	–	129.8$_{-0.05}$	60	–	35

Thrust piece EPO3

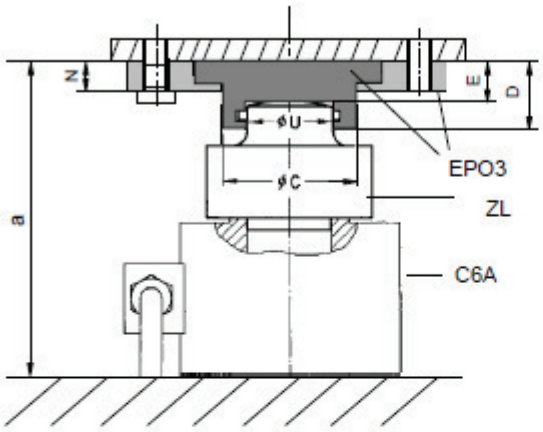

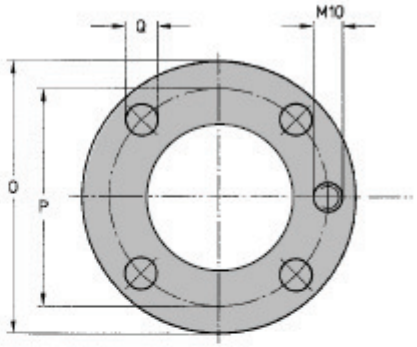

* Shown with load buttons ZL 0.2 MN...2 MN

Nominal forces	EPO3 order no.	Weight in kg	C	D	E	N	O	P	Q	U$_{-0.2}$	a
200 kN	1-EPO3R/20T	1.2	47.9	27.5	20	14	114	90	13	32	125
500 kN	1-EPO3/50T	3.4	81.9	50	39.5	20	148	120	17	44	144.5
1 MN	1-EPO3/100T	3.2	81.9	50	39.5	20	148	120	17	64	219.5
2 MN	1-EPO3/250T	13.0	139.5	80	67.5	25	225	190	22	85	247.5
5 MN	1-EPO3/500T	27.0	169.8	103	90	33	270	220	26	130	250

Specifications (data according to VDI standards 2638)

Type			C0A				
Accuracy class			0.5				
Nominal force	F_{nom}	MN	200 kN	500 kN	1 MN	2 MN	5 MN
Nominal sensitivity	C_{nom}	mV/V	2				
Relative sensitivity deviation[2]	d_c						
when used with hardened pressure plates		%			< ± 2.5		
when used with load button ZL and pendle bearing EPO3		%			< ± 0.5		
when used with spherical cap ZK		%		< ± 2.5		< ± 4	
Relative zero signal deviation	$d_{s,o}$	%			< 1		
Relative range of inversion ($0.5F_{nom}$)	u	%			< ± 0.8		
Linearity deviation[2]	d_{lin}						
when used with hardened pressure plates		%			< ± 1		
when used with load button ZL and pendle bearing EPO3		%			< ± 0.5		
when used with spherical cap ZK		%			< ± 1		
Effect of temperature on sensitivity / 10 K by reference to nominal sensitivity	TK_C	%			< ± 0.1		
Effect of temperature on zero signal / 10 K by reference to nominal sensitivity	TK_0	%			< ± 0.05		
Creep over 30 min, in nominal temperature range[1]	d_{crF+E}	%			< ± 0.06		
Input resistance at reference temperature	R_e	Ω			> 345		
Output resistance at reference temperature	R_a	Ω			356 ± 1.5		
Isolation resistance at test voltage 100 V	R_{is}	GΩ			$> 5 \times 10^9$		
Reference excitation voltage	U_{ref}	V			5		
Operating range of the excitation voltage	$B_{U,GT}$	V			0.5 ... 12		
Reference temperature	t_{ref}	°C			+23		
Nominal temperature range	$B_{t,nom}$	°C			−10...+70		
Operating temperature range	$B_{t,G}$	°C			−30...+85		
Storage temperature range	$B_{t,S}$	°C			−50...+100		
Maximum operating force[1]	F_G	%			150		
Limit force[1]	F_L	%			150		
Breaking force[1]	F_B						
when used with hardened pressure plates		%			> 300		
when used with load button ZL and pendle bearing EPO3		%			> 300		> 200
when used with spherical cap ZK		%			> 200		> 200
Static lateral limit force[1]	F_Q						
when used with hardened pressure plates		%			20		
when used with load button ZL and pendle bearing EPO3		%			20		10
when used with spherical cap ZK		%			10		
Permissible vibration amplitude[1] to DIN 50 100	F_{rb}	%			70		
Nominal displacement without mounting accessories (± 15 %)	S_{nom}	mm	0.07	0.08	0.09	0.11	0.26
Natural frequency without coupled ground and without mounting accessories	f_G	kHz	4.5	8	6	7.5	4.3
Weight, without cable		kg	1.4	1.7	10.8	12.2	33
Degree of protection to DIN EN 60 529			IP 67				
Cable length, 6-wire connection		m	6				

[1] related to the nominal force

[2] the differing tolerances when using different mounting accessoires are due to the transducer's low profile

Hottinger Baldwin Messtechnik GmbH

Im Tiefen See 45 · 64293 Darmstadt · Germany
Tel. +49 6151 803-0 · Fax: +49 6151 803-9100
Email: info@hbm.com · www.hbm.com

measure and predict with confidence

HBM

B0635-2.3 en

B.2: Excerpt From QuantumX MX410B Data Sheet

QUANTUM X

MX410B

Highly dynamic
universal amplifier

Data sheet

Special features

- 4 individually configurable inputs (electrically isolated)
- Connection of more than 5 transducer technologies
- Individual sample rates up to 100 kS per channel, 200 kS at 2 channels
- 24-bit A/D converter per channel for synchronous, parallel measurements
- 4 analog outputs
- Real-time computation (Peak, RMS)
- Supply voltage (DC) for active transducers: 5 V ... 24 V

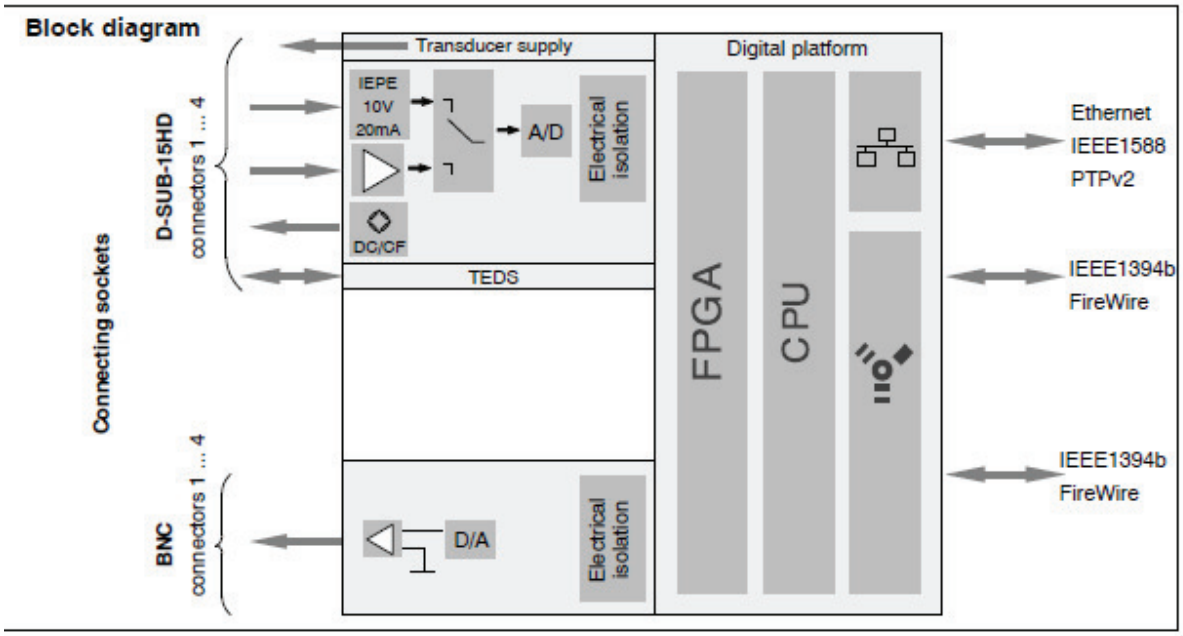

B3889-4.0 en

HBM

Specifications MX410B

General specifications		
Inputs	number	4, electrically isolated from each other and from supply[1]
Transducer technologies per connector		Strain gage, half and full bridge (carrier frequency or DC), Quarter-bridge with 1-SCM-SG120/350, piezoresistive full bridge, IEPE (ICP®), Inductive half and full bridge, voltage, normalized voltage (± 10 V), electric voltage up to 300 V CAT II with Adapter-SCM-HV, normalized current (20 mA)
A/D conversion		24-bit delta-sigma converter
Sample rates (Domaine adjustable by software, Factory setting is „HBM Classic)	Hz	Decimal : 0.1 ... 100,000, adjustable for each channel 0.1 ... 200,000 in two-channel mode HBM Classic: 0.1 ... 96,000 adjustable for each channel 0.1 ... 192,000 in two-channel mode
Bandwidth (-3 dB)	kHz	38 78in two-channel mode
Active low pass filter (Bessel/Butterworth, adjustable)	Hz	0.1 ... 20,000
Transducer identification		TEDS, IEEE 1451.4
max. TEDS module distance	m	100
Transducer connection		D-SUB-15HD
Analog outputs		4 (BNC), electrically isolated to measurement inputs and to supply (not to one another)
Supply voltage range (DC)	V	10 ... 30 (nominal (rated) voltage 24 V)
Supply voltage interruption		max. for 5 ms at 24 V
Power consumption		
without adjustable transducer excitation	W	< 12
with adjustable transducer excitation	W	< 15
Supply voltage (active transducers)		
Adjustable transducer excitation (DC)	V	5 ... 24; adjustable channel by channel
Maximum output power	W	0.7 per channel / 2 in total
Ethernet (data link)		10Base-T / 100Base-TX
Protocol/addressing	-	TCP/IP (direct IP address or DHCP)
Plug connection	-	8P8C-modular plug (RJ-45) with twisted pair cable (CAT-5)
Max. cable length to module	m	100
Synchronization options		IEEE1394b FireWire (only QuantumX, automatically, recommended)
EtherCAT®[4]		via CX27
IRIG-B (B000 to B007; B120 to B127)		via MX440A- or MX840A input channel
IEEE1588 (PTPv2), NTP		Ethernet based Network Time Protocol
IEEE1394b FireWire (module synchronization, data link, optional supply voltage)		IEEE 1394b (HBM modules only)
Baud rate	MBaud	400 (approx. 50 MBytes/s)
Max. current from module to module	A	1.5
Max. cable length between nodes	m	5
Max. number of modules connected in series (daisy chain)	-	12 (= 11 hops)
Max. number of modules in a IEEE1394b FireWire system (incl. hubs[2], backplane)	-	24
Max. number of hops[3]	-	14
Nominal (rated) temperature range	°C [°F]	-20 ... +65 [-4 ... +149]
Storage temperature range	°C [°F]	-40 ... +75 [-40 ... +167]
Relative humidity	%	5 ... 95 (non-condensing)
Protection class	-	III
Degree of protection		IP20 per EN60529
Mechanical tests[5]		
Vibration (30 min)	m/s^2	50
Shock (6 ms)	m/s^2	350
EMC requirements		per EN 61326
Maximum input voltage at transducer socket to ground (PIN 6 or PIN 9)		
PIN 1, 2, 3, 4, 5, 7, 8, 10 (bridge and TEDS)	V	±5.5
PIN 14 (voltage)	V	±40
PIN 13 (current)	V	± 1.5
PIN 4, 15 (control circuits)	V	+ 3.3

1) When variable transducer supply is used, there is no electrical isolation from the supply.
2) Hub: IEEE1394b FireWire node point or distributor
3) Hop: transition from module to module/signal conditioning
4) EtherCAT® is a registered trademark and patented technology, licensed by Beckhoff Automation GmbH, Germany
5) Mechanical stress is tested in accordance with European standards EN60068-2-6 for vibration and EN60068-2-27 for shock. The devices are exposed to an acceleration of 50 m/s^2 within the frequency range 5...65 Hz in all 3 axes. Duration of this vibration test: 30 minutes per axis. The shock test is implemented at a nominal (rated) acceleration of 350 m/s^2 for a duration of 6 ms, half sine and with shocks in each of the six possible directions.

Specifications MX410B (continued)

Dimensions, horizontal (H x W x D)	mm mm	52.5 x 200 x 122 (with case protection) 44 x 174 x 119 (without case protection)
Weight, approx.	g	990

Strain gage full bridge and half bridge 4 mV/V CF with excitation 1 V or 2.5 V or 5 V (AC, effective)		
Accuracy class		0.05[1]
Carrier frequency (sine)	Hz	4,800 ± 2
Bridge excitation voltage (effective)	V	1; 2.5; 5 (± 5 %)
Transducers that can be connected		Strain gage and inductive full and half bridges
Permissible cable length between MX410B and transducer	m	< 100
Measuring ranges at 5 V excitation at 2.5 V excitation at 1 V excitation	 mV/V mV/V mV/V	 ±4 ±8 ±20
Additional shunt resistor can be connected (control signal)	kΩ	100 ± 0.1%
Measurement frequency range (–3 dB)	Hz	0 ... 1,600
Transducer impedance at 5 V excitation at 2.5 V excitation at 1 V excitation	 Ω Ω Ω	 300 ... 1,000 110 ... 1,000 80 ... 1,000
Noise at 25 °C and 5 V excitation (peak to peak) at 1 Hz Bessel filter at 10 Hz Bessel filter at 100 Hz Bessel filter at 1 kHz Bessel filter	 µV/V µV/V µV/V µV/V	 < 0.1 < 0.2 < 0.5 < 1.5
Linearity error	%	< 0.02 of full scale value
Zero drift (full bridge with excitation 5 V)	% / 10 K	< 0.02[1] of full scale value
Full-scale drift (excitation 5 V)	% / 10 K	< 0.05 of measured value

[1] with half bridge : 0.1

Strain gage full bridge and half bridge 4 mV/V DC with excitation 1 V or 2.5 V or 5 V or 7.5 V (DC)		
Accuracy class		0.05[1]
Bridge excitation voltage (DC)	V	1 ; 2.5; 5; 7.5 (± 6 %)
Transducers that can be connected		Strain gage full and half bridges
Permissible cable length between MX410B and transducer	m	< 100 (at U_B=7.5 V: < 50 m)
Measuring ranges at 7.5 V excitation at 5 V excitation at 2.5 V excitation at 1 V excitation	 mV/V mV/V mV/V mV/V	 ±4 ±4 ±10 ±20
Additional shunt resistor can be connected (control signal)	kΩ	100 ± 0.1%
Measurement frequency range (–3 dB)	Hz	0 ... 38,300 with 96,000 Hz data rate 0 ... 78,600 with 192,000 Hz data rate
Transducer impedance at 7.5 V excitation at 5 V excitation at 2.5 V excitation at 1 V excitation	 Ω Ω Ω Ω	 300 ... 1,000[2] (max. 50 m cable) 300 ... 1,000[2] 110 ... 1,000[2] 80 ... 1,000[2]
Noise at 25 °C and 5 V excitation (peak to peak) at 1 Hz Bessel filter at 10 Hz Bessel filter at 100 Hz Bessel filter at 1 kHz Bessel filter at 10 kHz Bessel filter at filter Off	 µV/V µV/V µV/V µV/V µV/V µV/V	 < 0.15 < 0.3 < 0.6 < 2 < 9 < 10
Linearity error	%	< 0.02 of full scale value
Zero drift (full bridge with excitation 5 V)	% / 10 K	< 0.05[1] of full scale value
Full-scale drift (excitation 5 V)	% / 10 K	< 0.05 of measured value

[1] with half bridge : 0.1

[2] Range can be modulated up to 5 kΩ, in this case: up to 1 % absolute zero deviation

Specifications MX410B (continued)

Strain gage full bridge and half bridge 100 mV/V CF with excitation 1 V or 2.5 V (AC, effective)		
Accuracy class		0.05[1]
Carrier frequency (sine)	Hz	4,800 ± 2
Bridge excitation voltage (effective)	V	1; 2.5; (± 6 %)
Transducers that can be connected		Strain gage and inductive full and half bridges
Permissible cable length between MX410B and transducer	m	< 100
Measuring ranges		
at 2.5 V excitation	mV/V	± 100
at 1 V excitation	mV/V	± 250
Measurement frequency range (–3 dB)	Hz	0 ... 1,600
Transducer impedance		
at 2.5 V excitation	Ω	110 ... 1,000
at 1 V excitation	Ω	80 ... 1,000
Noise at 25 °C and 2.5 V excitation (peak to peak)		
at 1 Hz Bessel filter	µV/V	< 2
at 10 Hz Bessel filter	µV/V	< 4
at 100 Hz Bessel filter	µV/V	< 12
at 1 kHz Bessel filter	µV/V	< 40
Linearity error	%	< 0.02 of full scale value
Zero drift (full bridge with excitation 2.5 V)	% / 10 K	< 0.01[1] of full scale value
Full-scale drift (excitation 2.5 V)	% / 10 K	< 0.05 of measured value

[1] with half bridge : 0.1

Piezoresistive strain gage full bridge and half bridge 100 mV/V DC with excitation 2.5 V or 5 V (DC)		
Accuracy class		0.05[1]
Bridge excitation voltage (DC)	V	2.5; 5 (± 5 %)
Transducers that can be connected		Strain gage full and half bridges
Permissible cable length between MX410B and transducer	m	< 100
Measuring ranges		
at 5 V excitation	mV/V	± 50
at 2.5 V excitation	mV/V	± 100
Measurement frequency range (–3 dB)	Hz	0 ... 39,300 with 96,000 Hz data rate
	Hz	0 ... 78,600 with 192,000 Hz data rate
Transducer impedance		
at 5 V excitation	Ω	300 ... 5,000
at 2.5 V excitation	Ω	110 ... 5,000
Noise at 25 °C and 5 V excitation (peak to peak)		
at 1 Hz Bessel filter	µV/V	< 2
at 10 Hz Bessel filter	µV/V	< 3
at 100 Hz Bessel filter	µV/V	< 8
at 1 kHz Bessel filter	µV/V	< 25
at 10 kHz Bessel filter	µV/V	< 130
at filter Off	µV/V	< 150
Linearity error	%	< 0.02 of full scale value
Zero drift (full bridge with excitation 5 V)	% / 10 K	< 0.03[1] of full scale value
Full-scale drift (excitation 5 V)	% / 10 K	< 0.05 of measured value

[1] with half bridge : 0.1

Specifications MX410B (continued)

Voltage 10 V (DC)		
Accuracy class		0.03
Transducers that can be connected		Voltage sensor ± 10 V
Permissible cable length between MX410B and transducer	m	< 100
Measuring range	V	± 10
Measurement frequency range (–3 dB)	Hz Hz	0 ... 39,300 with 96,000 Hz data rate 0 ... 78,600 with 192,000 Hz data rate
Internal resistance of the connected voltage source	kΩ	< 5
Input impedance	MΩ	> 10
Noise at 25 °C (peak to peak) at 1 Hz Bessel filter at 10 Hz Bessel filter at 100 Hz Bessel filter at 1 kHz Bessel filter at 10 kHz Bessel filter at filter Off	 µV µV µV µV µV µV	 < 100 < 300 < 600 < 3,000 < 13,000 < 15,000
Linearity error	%	< 0.02 of full scale value
Common-mode rejection at DC common-mode at 50 Hz common-mode	 dB dB	 > 100 75
Max. common-mode voltage (to housing and supply ground)	V	± 60
Zero drift	% / 10 K	< 0.02 of full scale value
Full-scale drift	% / 10 K	< 0.03 of measured value

Current 20 mA (DC)		
Accuracy class		0.03
Transducers that can be connected		Transducer with 4 ... 20 mA current output
Permissible cable length between MX410B and transducer	m	< 100
Measuring range	mA	± 20
Measurement frequency range (–3 dB)	Hz Hz	0 ... 39,300 with 96,000 Hz data rate 0 ... 78,600 with 192,000 Hz data rate
Measuring resistance value	Ω	50
Noise at 25 °C (peak to peak) at 1 Hz Bessel filter at 10 Hz Bessel filter at 100 Hz Bessel filter at 1 kHz Bessel filter at 10 kHz Bessel filter at filter Off	 µA µA µA µA µA µA	 < 0.5 < 1.5 < 10 < 20 < 28 < 30
Linearity error	%	< 0.02 of full scale value
Common-mode rejection at DC common-mode at 50 Hz common-mode	 dB dB	 > 100 typically 75
Max. common-mode voltage (to housing and supply ground)	V	± 60
Zero drift	% / 10 K	< 0.02 of full scale value
Full-scale drift	% / 10 K	< 0.03 of measured value

Specifications MX410B(continued)

Current-fed piezoelectric transducers (IEPE – Integrated Electronics Piezo Electric, ICP®)		
Accuracy class		0.1
Transducer technology		IEPE (BNC adapter available: 1-SUBHD15-BNC)
Permissible cable length between MX410B and transducer	m	< 30
Transducer identification (TEDS, IEEE 1451.4)		only version 1.0
Transducer excitation	mA	4 mA ± 15%
Measuring ranges	V	± 2; ± 10
Measurement frequency range (–3 dB)	Hz Hz	0 ... 39,300 with 96,000 Hz data rate 0 ... 78,600 with 192,000 Hz data rate
Internal resistance of the connected voltage source, typ.	kΩ	2 . . . 3
Noise at 25 °C and measuring range ± 10 V (peak to peak)		
at 1 Hz Bessel filter	µV	< 100
at 10 Hz Bessel filter	µV	< 300
at 100 Hz Bessel filter	µV	< 600
at 1 kHz Bessel filter	µV	< 3,000
at 10 kHz Bessel filter	µV	< 13,000
at filter Off	µV	< 15,000
Linearity error	%	< 0.1 of full scale value
Common-mode rejection		
at DC common-mode	dB	> 100
at 50 Hz common-mode, typically	dB	75
Max. common-mode voltage (to housing and supply ground)	V	± 60
Zero drift	% / 10 K	< 0.1 of full scale value
Full-scale drift	% / 10 K	< 0.05 of output value

Analog outputs		
Accuracy class		0.05
Number of outputs		4 (input1 to output1 etc.)
Type of connection		BNC
Max. cable length	m	< 30
Bandwidth	kHz	Defined by the input signal filter
Output rate max.	kHz	576
Nominal (rated) voltage	V	± 10
Reference signal		Common ground for all outputs, electrically isolated from supply and measurement inputs
D/A converter resolution	bits	16
Noise (peak to peak)	mV	< 10
Permissible load impedance	Ω	> 2,000 / <2 nF
Crosstalk attenuation	dB	> 65
Min. settling time	µs	120
Zero drift	% / 10 K	< 0.05 of full scale value
Full-scale drift	% / 10 K	< 0.05 of output value

Real-time computation on the module		
Root-mean-square unit (RMS)		4
Peak-value unit		
Number of peak values		8
Max. output rate	Hz	4800

APPENDIX C: SIMULATION PARAMETERS

C.1: Carbon Fibre Prepreg Data Sheet

Technical Data Sheet

Description: CM-Preg T-C-1 200/635 CP0031 42

The CP003 systems are high flow, low viscosity epoxy systems. Due to the low viscosity at high temperature these systems are suitable for vacuum only processes at low temperatures. The systems could be pigmented upon request

Benefits and Features:

modifyed flow characteristic
good bonding properties
suitable for vacuum process
very good surface properties

Matrix Properties:

		CP0031
min. Viscosity	mPas	325
T_g (2h/120°C)	°C	125
Colour		transparent
Specials		tbd

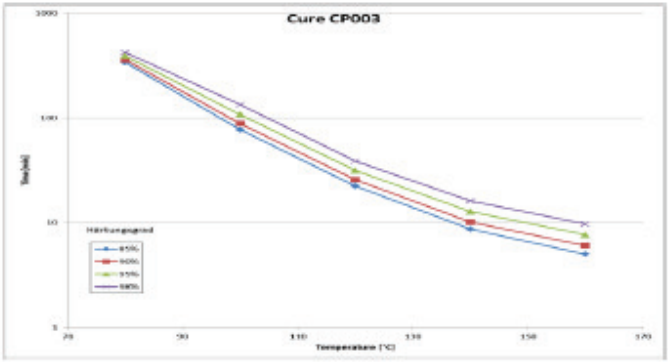

For more information please contact
c-m-p GmbH Industrieparkstr 15 52525 Heinsberg Tel.: +49 (0) 2452 1572110
www.c-m-p-gmbh.de support@c-m-p-gmbh.de

1 / 3

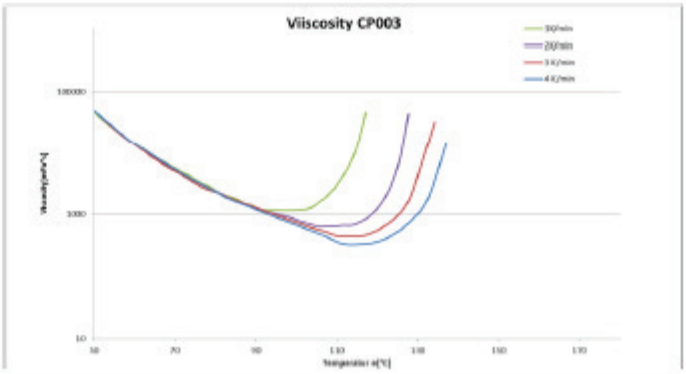

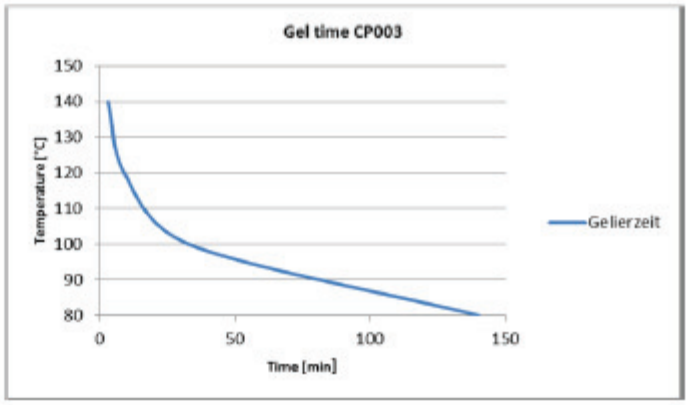

Storage Life and Storage Conditions

45 days	@	20 °C
12 month	@	-18 °C

Processing

Prepregs out of CP003 resin system are processable with all common techologies. The typical processing window is between 80°C and 170°C. The curing time varies from 4min up to 8hours depending on temperature

For more information please contact
c-m-p GmbH Industrieparkstr 15 52525 Heinsberg Tel.: +49 (0) 2452 1572110
www.c-m-p-gmbh.de support@c-m-p-gmbh.de

Technical Data Sheet

Prepreg Properties:

Textuer:	Epoxy Carbon UD-Prepreg

Fiber Areal weight:	g/m^2	DIN	29971	200
Resin Content:	%	DIN	2557 C	42
Prepreg Areal Weight:	g/m^2	DIN	2557 C	345
Width:	mm	DIN		635

Laminate-Properties (Example - HT - Carbon fiber / 60 Vol%)

		CM-Preg F	CM-Preg T
Artikel			
Grade		Köper 2/2	UD
FAW	g/m^2	245	200

Tensile Strength 0°	MPa	DIN	ISO 527	1100	1900
E-Modulus 0°	GPa	DIN	ISO 527	70	135
Flexural Strength	MPa	DIN	ISO 14125	1050	2050
Flexural-Modulus 0°	GPa	DIN	ISO 14125	62	130
ILSF	MPa	DIN	EN 2563	70	85

additional mechanical properties available on request

Important

This is not a specification. All information is believed to be accurate in relation to the performance, storage and other characteristics of the product without acceptance of liability. Users are held to do their own tests to check the suitability of the product for its particular purpose

print date 01.10.2015

For more information please contact
c-m-p GmbH Industrieparkstr 15 52525 Heinsberg Tel.: +49 (0) 2452 1572110
www.c-m-p-gmbh.de support@c-m-p-gmbh.de

C.2: Mat54 Input Parameter Definitions

Variable	Definition	Suggested Value
MID	Material identification number	Any arbitrary integer
RO	Mass per unit volume*	ρ from material properties*
EA	Young's modulus in longitudinal direction.	E_1, from material properties
EB	Young's modulus in transverse direction.	E_2, from material properties
EC	Young's modulus through the thickness	Not used
PRBA	Minor Poisson's ratio, $v_{ba} = v_{21}$	Calculated using v_{12} , E_1 and E_2
PRCA	Minor Poisson's ratio, $v_{ca} = v_{31}$	Not used
PRCB	Minor Poisson's ratio, $v_{cb} = v_{32}$	Not used
GAB	Shear modulus, G_{ab}	G_{12}, from material properties
GBC	Shear modulus, G_{bc}	Assumed equal to G_{ab}
GCA	Shear modulus, G_{ca}	Assumed equal to G_{ab}
KF	Bulk modulus of material	Not used
AOPT	Material axes option parameter	AOPT = 0
XP YP ZP	Material axes coordinates for AOPT = 1	Not used
A1 A2 A3 D1 D2 D3	Material axes coordinates for AOPT = 2	Not used
MANGLE	Material angle in degrees used when AOPT = 3	Not used
V1 V2 V3	Material axes coordinates for AOPT = 3	Not used
DFAILT	Max strain for fiber tension	DFAILT = (F_1^{tu} / E_1) [DFAILT > 0]
DFAILC	Max strain for fiber compression	DFAILC = (F_1^{cu} / E_1) [DFAILC < 0]
DFAILM	Max strain for matrix straining in tension and compression	DFAILM ≥ *max*[(YT/EB) , (YC/EB)]
DFAILS	Max shear strain	0 < DFAILS ≤ 0.1
EFS	Effective failure strain	EFS = 0
TFAIL	Time step size criteria for element deletion	0 < TFAIL < (Δt/10)
ALPH	Shear stress non-linear term	1E-3 ≤ ALPH ≤ 1
SOFT	Crush front strength reducing parameter	Must be calibrated for crush simulations
FBRT	Softening factor for fiber tensile strength after matrix failure	0 ≤ FBRT ≤ 1
YCFAC	Softening factor for fiber compressive strength after matrix failure	0 ≤ YCFAC ≤ (XC/YC)
BETA	Weighing factor for shear term in tensile fiber mode	0 ≤ BETA ≤ 1
XC	Longitudinal compressive strength	$\|F_1^{cu}\|$, from material properties
XT	Longitudinal tensile strength	F_1^{tu}, from material properties
YC	Transverse compressive strength	$\|F_2^{cu}\|$, from material properties
YT	Transverse tensile strength	F_2^{tu}, from material properties
SC	Shear strength	F_{12}^{tu}, from material properties
CRIT	Failure criterion used (MAT54 Chang-Chang, MAT55 Tsai-Wu)	Assign value of 54 or 55
*For English units, must be divided by a gravity factor to convert from pound-weight to pound-mass.		

C.3: MAT54 Input Parameters

TITLE	MAT_054_ENHANCED_COMPOSITE_DAMAGE						
Carbon Fibre							
MID	RO	EA	EB	EC	PRBA	PRCA	PRCB
1	1380	1.35E+11	8.41E+09	0	0.249	0	0
GAB	GBC	GCA	KF	AOPT			
4.21E+09	4.21E+09	4.21E+09	0.00E+00	2.00E+00			
XP	YP	ZP	A1	A2	A3	MANGLE	
0	0	0	1	0	0	0	
V1	V2	V3	D1	D2	D3	DFAILM	DFAILS
0	0	0		0	1	0.024	0.03
TFAIL	ALPH	SOFT	FBRT	YCFAC	DFAILT	DFAILC	EFS
1.15E-09	0.1	0	0.5	1.2	0.015	-0.0116	0
XC	XT	YC	YT	SC	CRIT	BETA	
1.45E+09	1.90E+09	1.99E+08	4.89E+07	1.54E+08	54	0.5	

C.4: Shell Input Parameter Definitions

Variable	Definition
SECID	Section ID
ELFORM	Element formulation options
SHRF	Shear factor which scales the transverse shear stress
NIP	Number of through shell thickness integration points
PROPT	Printout option: 3 = Resultant stresses at all points, fibre lengths
QR/IRID	Quadrature rule or Integration rule ID: 0 = Gauss
ICOMP	Flag for orthotropic/anisotropic layered composite material model.
SETYP	2D solid element type
T1-4	Shell thickness at nodes 1-4

C.5: Shell Input Parameters

TITLE	SECTION_SHELL						
0 UNIDIRECTIONAL							
SECID	ELFORM	SHRF	NIP	PROPT	QR/IRID	ICOMP	SETYP
1	11	1	40	3	0	0	1
T1	T2	T3	T4				
0.005	0.005	0.005	0.005				

TITLE	SECTION_SHELL						
90 UNIDIRECTIONAL							
SECID	ELFORM	SHRF	NIP	PROPT	QR/IRID	ICOMP	SETYP
1	11	1	40	3	0	0	1
T1	T2	T3	T4				
0.005	0.005	0.005	0.005				

TITLE		SECTION_SHELL					
45 CONTINUOUS							
SECID	ELFORM	SHRF	NIP	PROPT	QR/IRID	ICOMP	SETYP
1	11	1	40	3	0	1	1
T1	T2	T3	T4				
0.005	0.005	0.005	0.005				
B1	B2	B3	B4	B5	B6	B7	B8
0	0	45	45	90	90	-45	-45
B9	B10	B11	B12	B13	B14	B15	B16
0	0	45	45	90	90	-45	-45
B17	B18	B19	B20	B21	B22	B23	B24
0	0	45	45	90	90	-45	-45
B25	B26	B27	B28	B29	B30	B31	B32
0	0	45	45	90	90	-45	-45
B33	B34	B35	B36	B37	B38	B39	B40
0	0	45	45	90	90	-45	-45

TITLE		SECTION_SHELL					
45 CONTINUOUS							
SECID	ELFORM	SHRF	NIP	PROPT	QR/IRID	ICOMP	SETYP
1	11	1	40	3	0	1	1
T1	T2	T3	T4				
0.005	0.005	0.005	0.005				
B1	B2	B3	B4	B5	B6	B7	B8
0	0	45	45	90	90	-45	-45
B9	B10	B11	B12	B13	B14	B15	B16
0	0	45	45	90	90	-45	-45
B17	B18	B19	B20	B21	B22	B23	B24
0	0	45	45	45	45	0	0
B25	B26	B27	B28	B29	B30	B31	B32
-45	-45	90	90	45	45	0	0
B33	B34	B35	B36	B37	B38	B39	B40
-45	-45	90	90	45	45	0	0

TITLE		SECTION_SHELL					
30 SYMMETRICAL							
SECID	ELFORM	SHRF	NIP	PROPT	QR/IRID	ICOMP	SETYP
1	11	1	40	3	0	1	1
T1	T2	T3	T4				
0.005	0.005	0.005	0.005				
B1	B2	B3	B4	B5	B6	B7	B8
0	0	30	30	60	60	90	90
B9	B10	B11	B12	B13	B14	B15	B16
-60	-60	-30	-30	0	0	30	30
B17	B18	B19	B20	B21	B22	B23	B24
60	60	90	90	90	90	60	60
B25	B26	B27	B28	B29	B30	B31	B32
30	30	0	0	-30	-30	-60	-60
B33	B34	B35	B36	B37	B38	B39	B40
90	90	60	60	30	30	0	0

TITLE		SECTION_SHELL					
30 CONTINUOUS							
SECID	ELFORM	SHRF	NIP	PROPT	QR/IRID	ICOMP	SETYP
1	11	1	40	3	0	1	1
T1	T2	T3	T4				
0.005	0.005	0.005	0.005				
B1	B2	B3	B4	B5	B6	B7	B8
0	0	30	30	60	60	90	90
B9	B10	B11	B12	B13	B14	B15	B16
-60	-60	-30	-30	0	0	30	30
B17	B18	B19	B20	B21	B22	B23	B24
60	60	90	90	-60	-60	-30	-30
B25	B26	B27	B28	B29	B30	B31	B32
0	0	30	30	60	60	90	90
B33	B34	B35	B36	B37	B38	B39	B40
-60	-60	-30	-30	0	0	30	30

TITLE		SECTION_SHELL					
15 SYMMETRICAL							
SECID	ELFORM	SHRF	NIP	PROPT	QR/IRID	ICOMP	SETYP
1	11	1	40	3	0	1	1
T1	T2	T3	T4				
0.005	0.005	0.005	0.005				
B1	B2	B3	B4	B5	B6	B7	B8
0	0	15	15	30	30	45	45
B9	B10	B11	B12	B13	B14	B15	B16
60	60	75	75	90	90	-75	-75
B17	B18	B19	B20	B21	B22	B23	B24
-60	-60	-45	-45	-45	-45	-60	-60
B25	B26	B27	B28	B29	B30	B31	B32
-75	-75	90	90	75	75	60	60
B33	B34	B35	B36	B37	B38	B39	B40
45	45	30	30	15	15	0	0

TITLE		SECTION_SHELL					
15 CONTINUOUS							
SECID	ELFORM	SHRF	NIP	PROPT	QR/IRID	ICOMP	SETYP
1	11	1	40	3	0	1	1
T1	T2	T3	T4				
0.005	0.005	0.005	0.005				
B1	B2	B3	B4	B5	B6	B7	B8
0	0	15	15	30	30	45	45
B9	B10	B11	B12	B13	B14	B15	B16
60	60	75	75	90	90	-75	-75
B17	B18	B19	B20	B21	B22	B23	B24
-60	-60	-45	-45	-30	-30	-15	-15
B25	B26	B27	B28	B29	B30	B31	B32
0	0	15	15	30	30	45	45
B33	B34	B35	B36	B37	B38	B39	B40
60	60	75	75	90	90	-75	-75

TITLE		SECTION_SHELL					
10 SYMMETRICAL							
SECID	ELFORM	SHRF	NIP	PROPT	QR/IRID	ICOMP	SETYP
1	11	1	40	3	0	1	1
T1	T2	T3	T4				
0.005	0.005	0.005	0.005				
B1	B2	B3	B4	B5	B6	B7	B8
0	0	10	10	20	20	30	30
B9	B10	B11	B12	B13	B14	B15	B16
40	40	50	50	60	60	70	70
B17	B18	B19	B20	B21	B22	B23	B24
80	80	90	90	90	90	80	80
B25	B26	B27	B28	B29	B30	B31	B32
70	70	60	60	50	50	40	40
B33	B34	B35	B36	B37	B38	B39	B40
30	30	20	20	10	10	0	0

TITLE		SECTION_SHELL					
10 CONTINUOUS							
SECID	ELFORM	SHRF	NIP	PROPT	QR/IRID	ICOMP	SETYP
1	11	1	40	3	0	1	1
T1	T2	T3	T4				
0.005	0.005	0.005	0.005				
B1	B2	B3	B4	B5	B6	B7	B8
0	0	10	10	20	20	30	30
B9	B10	B11	B12	B13	B14	B15	B16
40	40	50	50	60	60	70	70
B17	B18	B19	B20	B21	B22	B23	B24
80	80	90	90	-80	-80	-70	-70
B25	B26	B27	B28	B29	B30	B31	B32
-60	-60	-50	-50	-40	-40	-30	-30
B33	B34	B35	B36	B37	B38	B39	B40
-20	-20	-10	-10	0	0	10	10

APPENDIX D: FORCE VS. TIME RESPONSE PLOTS

D.1: 90° Unidirectional Set

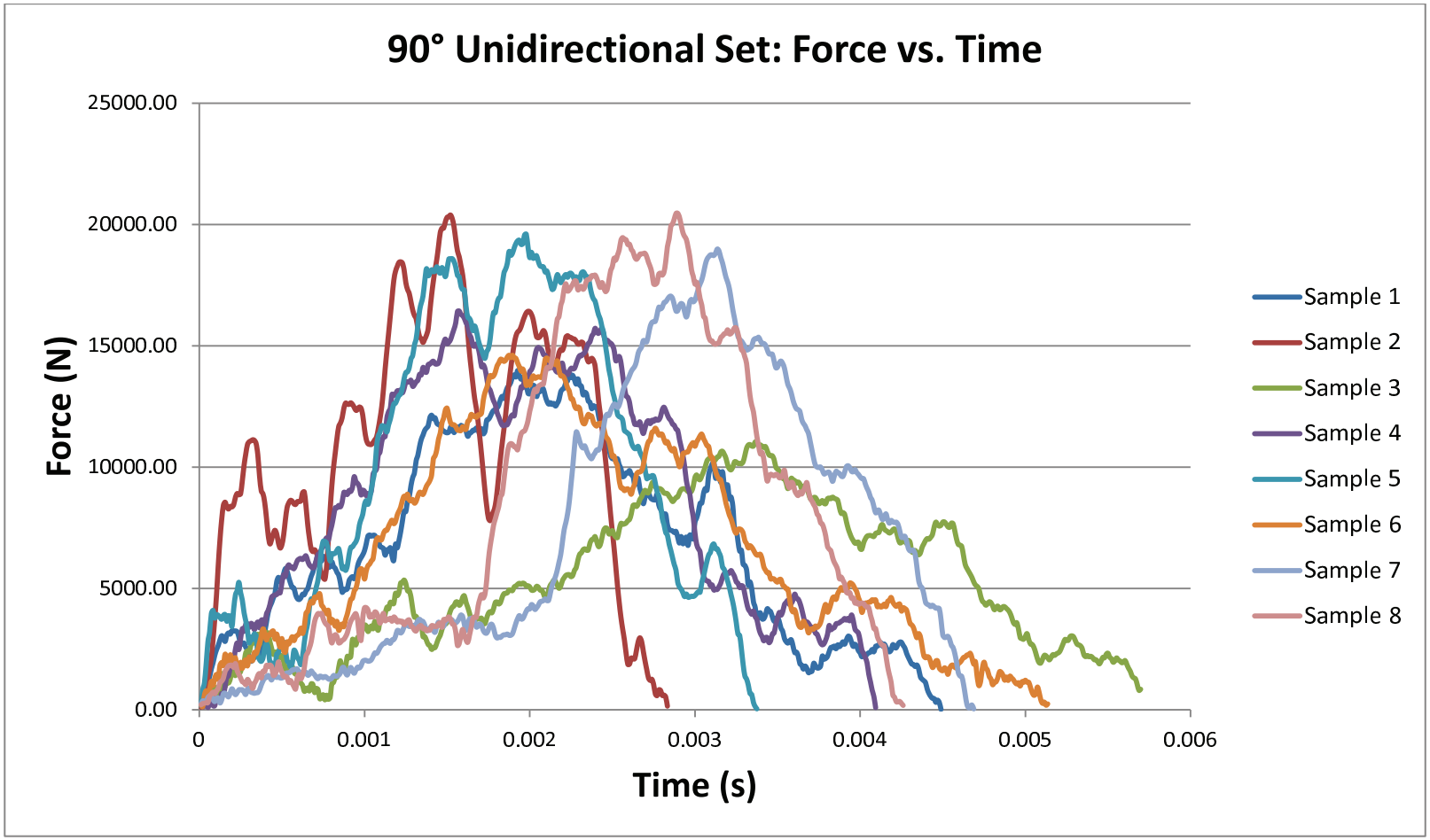

D.2: 0° Unidirectional Set

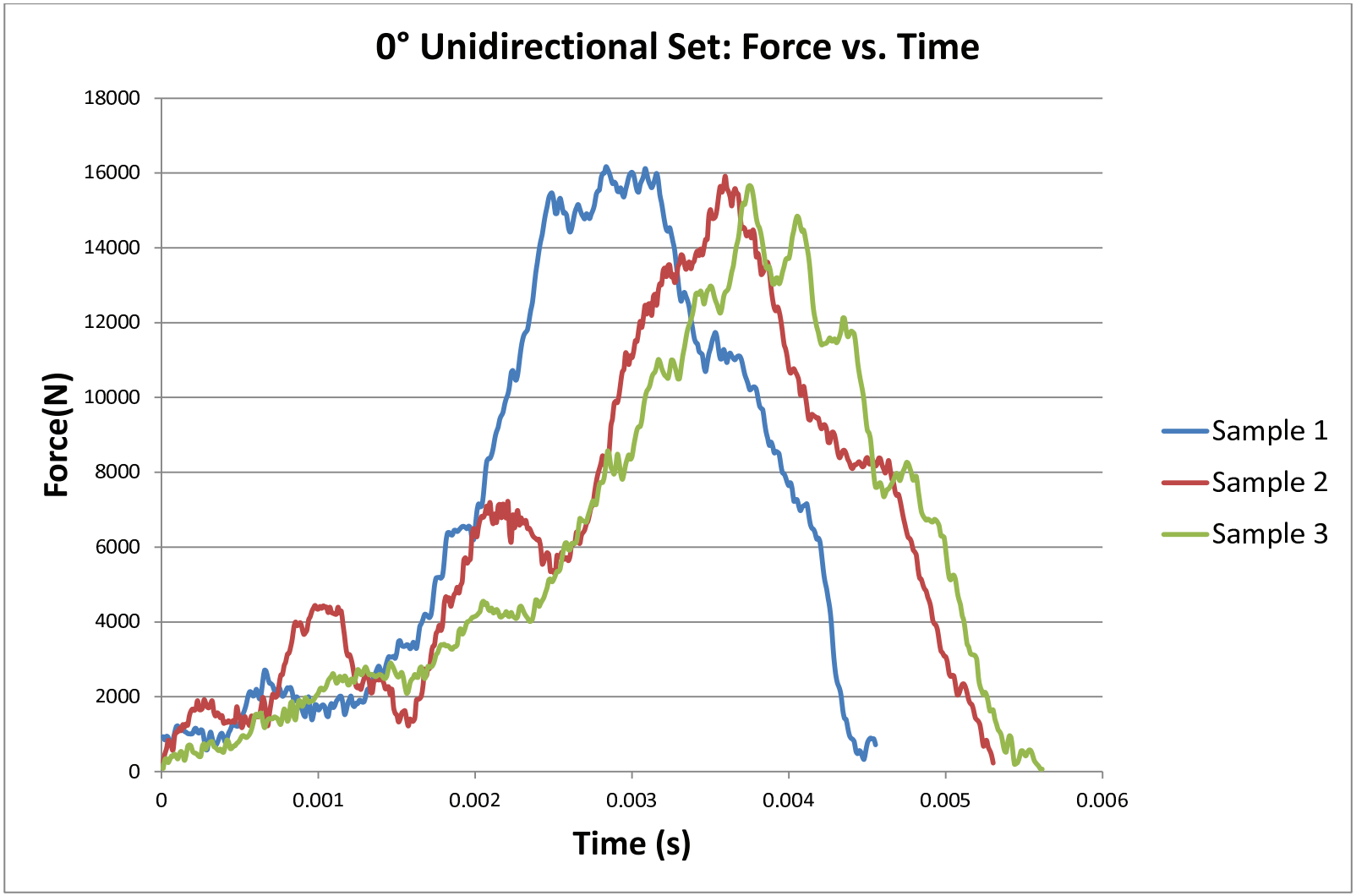

D.3: 45° Symmetrical Set

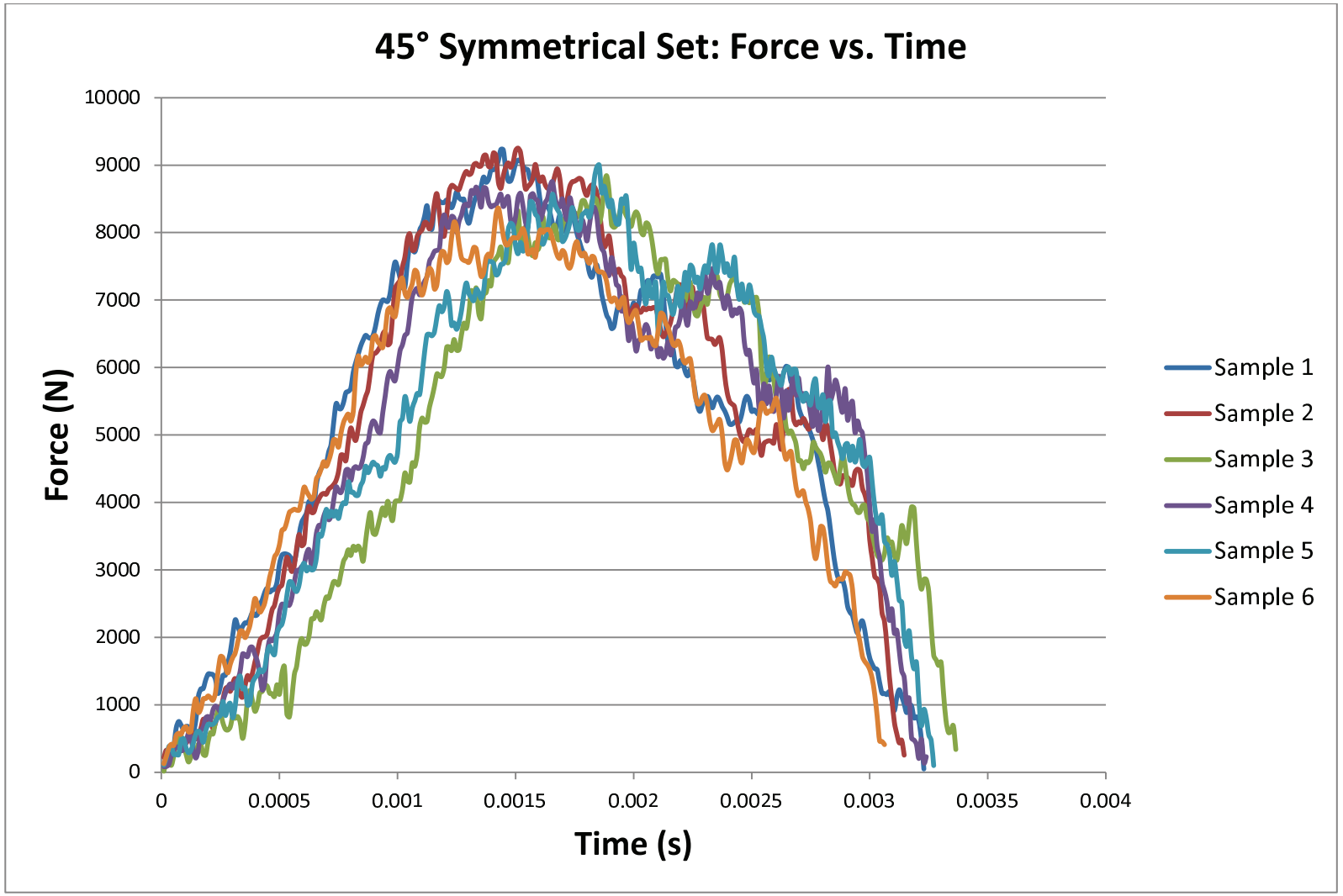

D.4: 45° Continuous Set

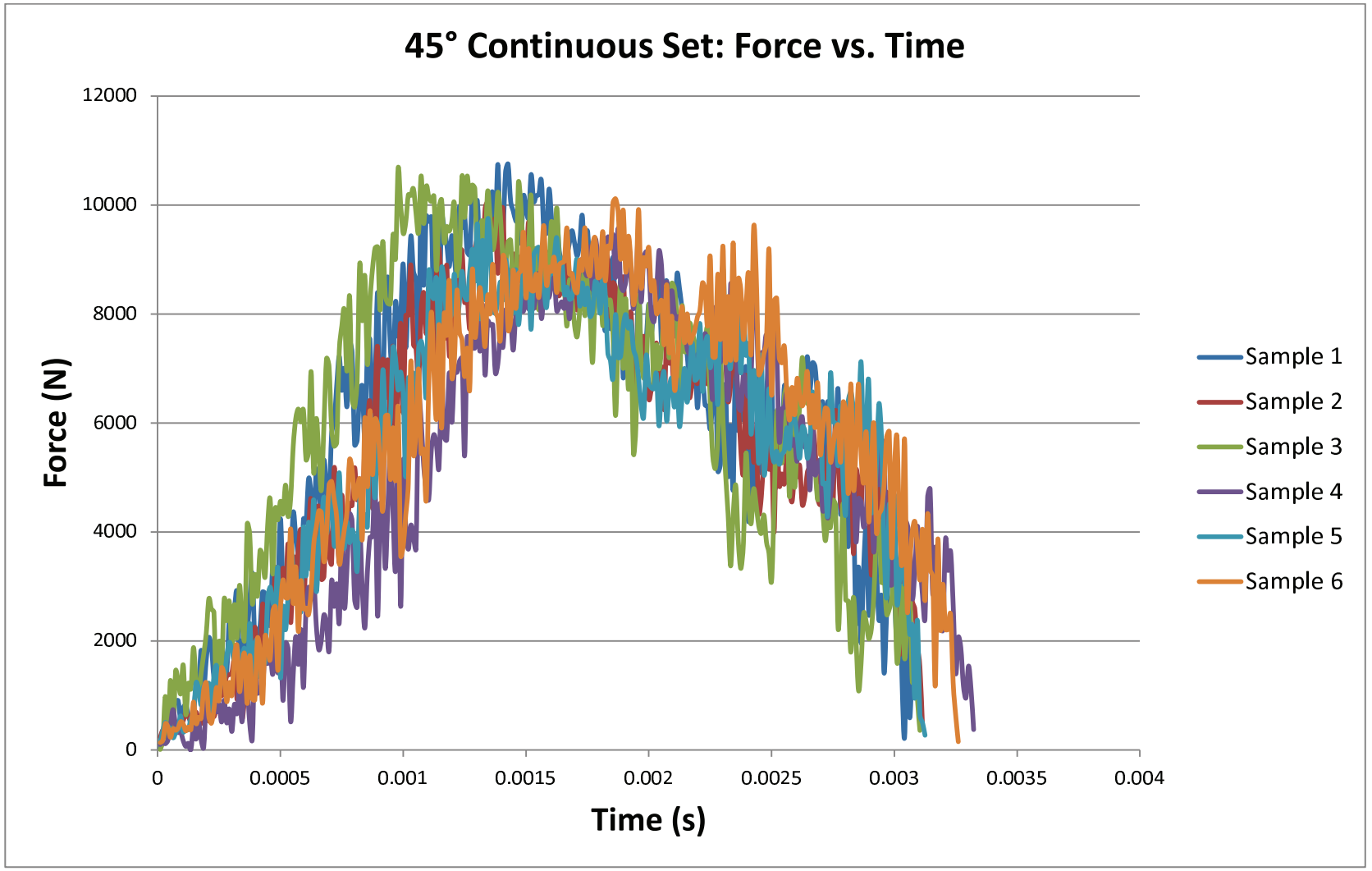

D.5: 30° Symmetrical Set

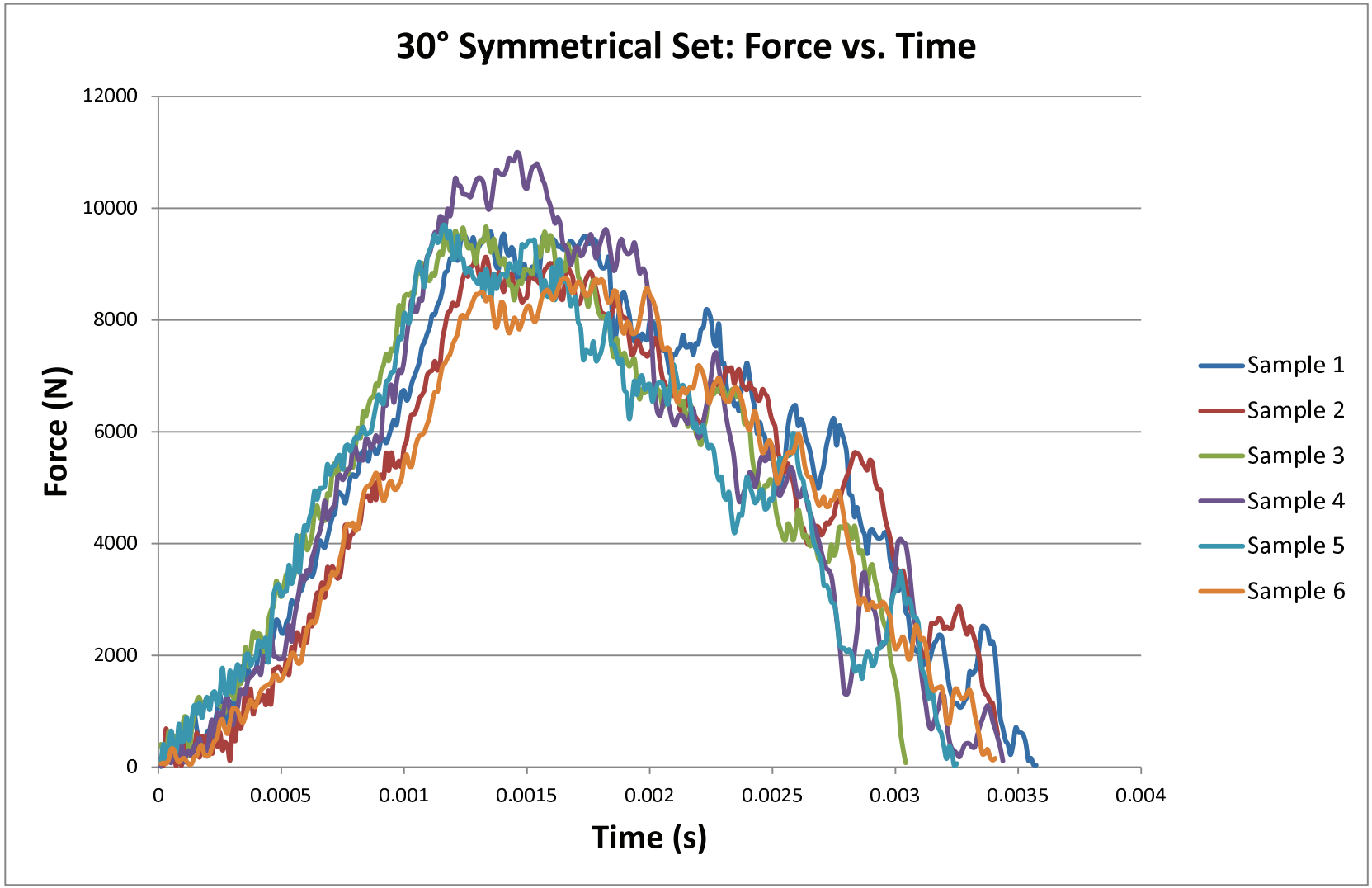

D.6: 30° Continuous Set

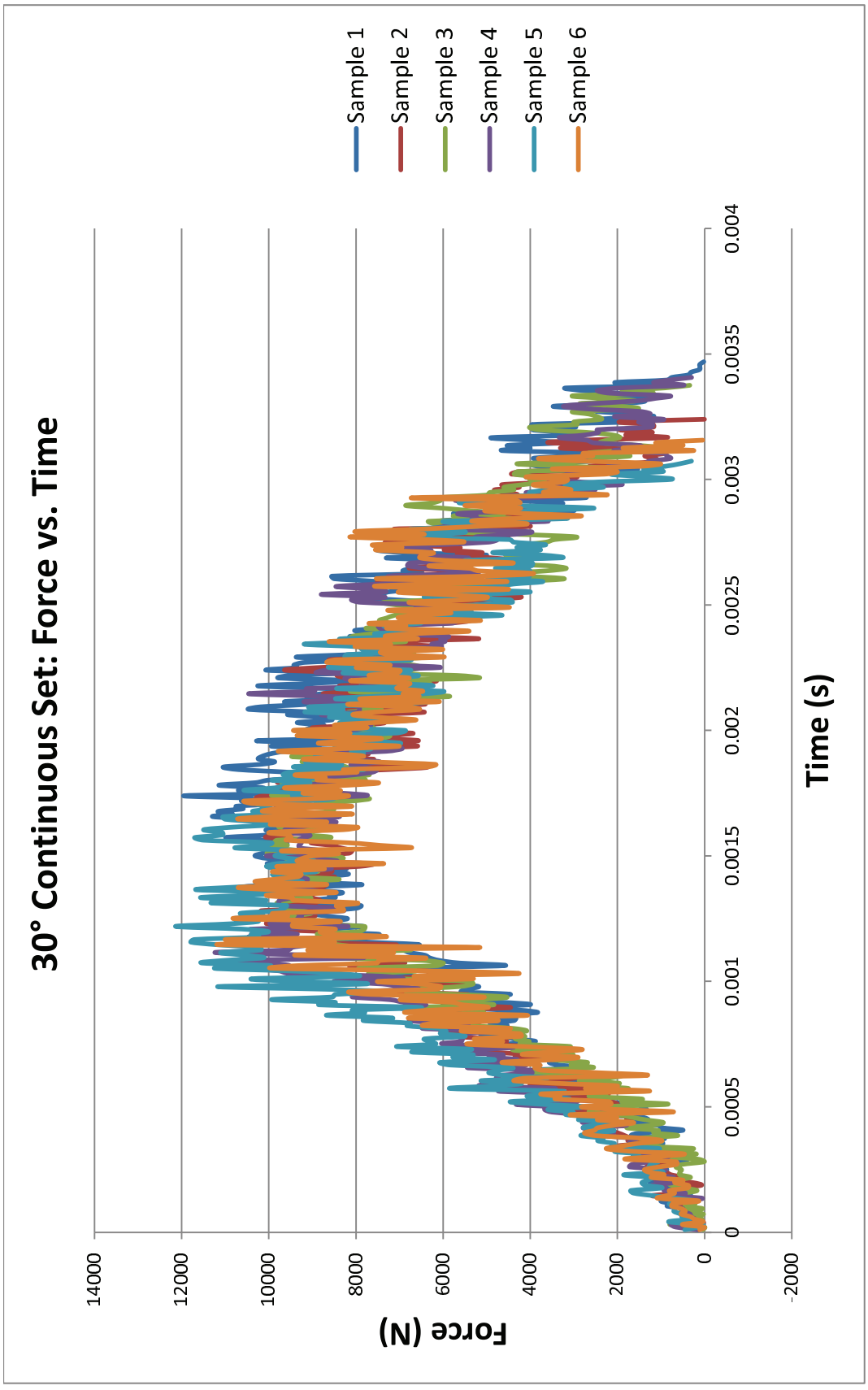

D.7: 15° Symmetrical Set

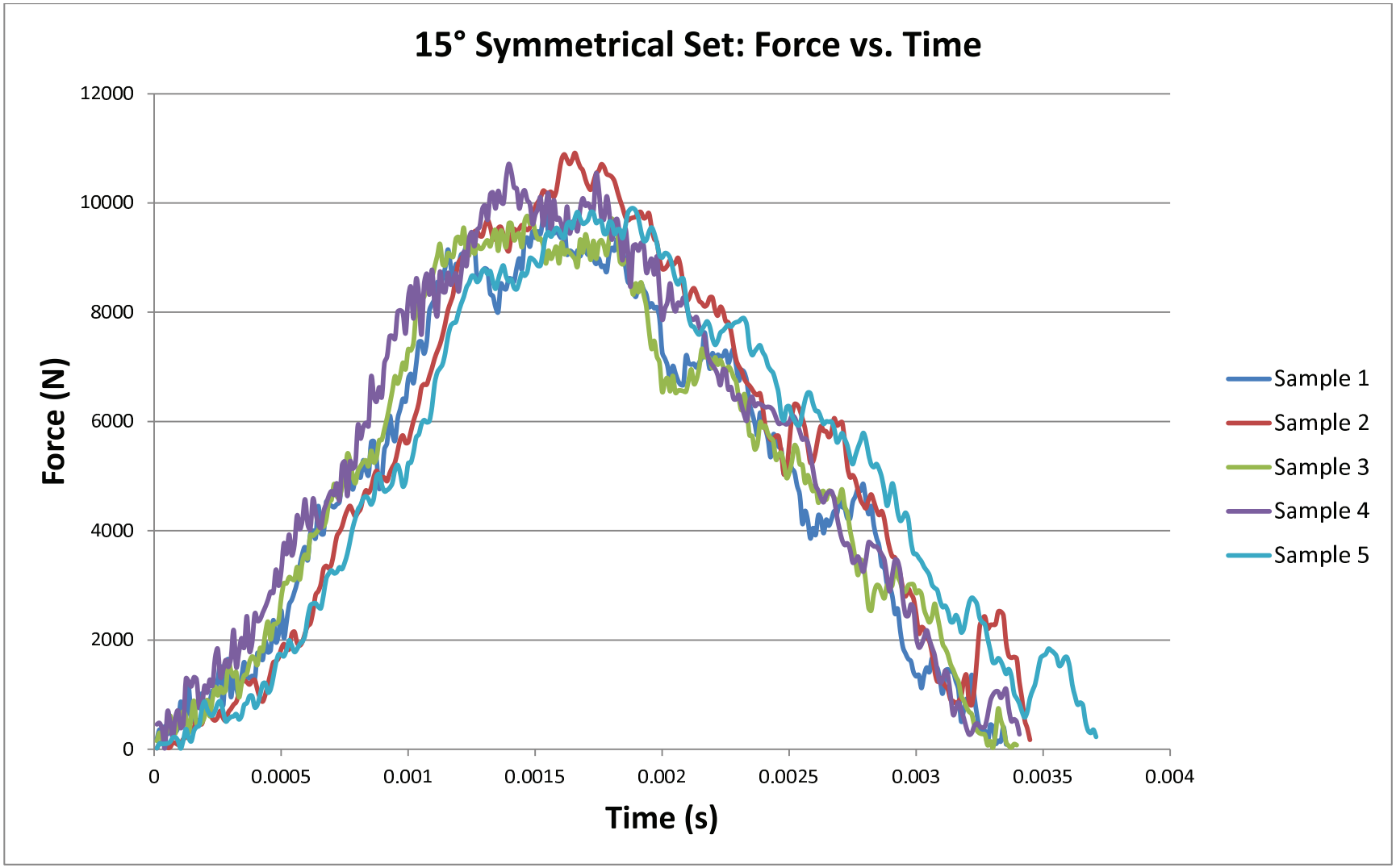

D.8: 15° Continuous Set

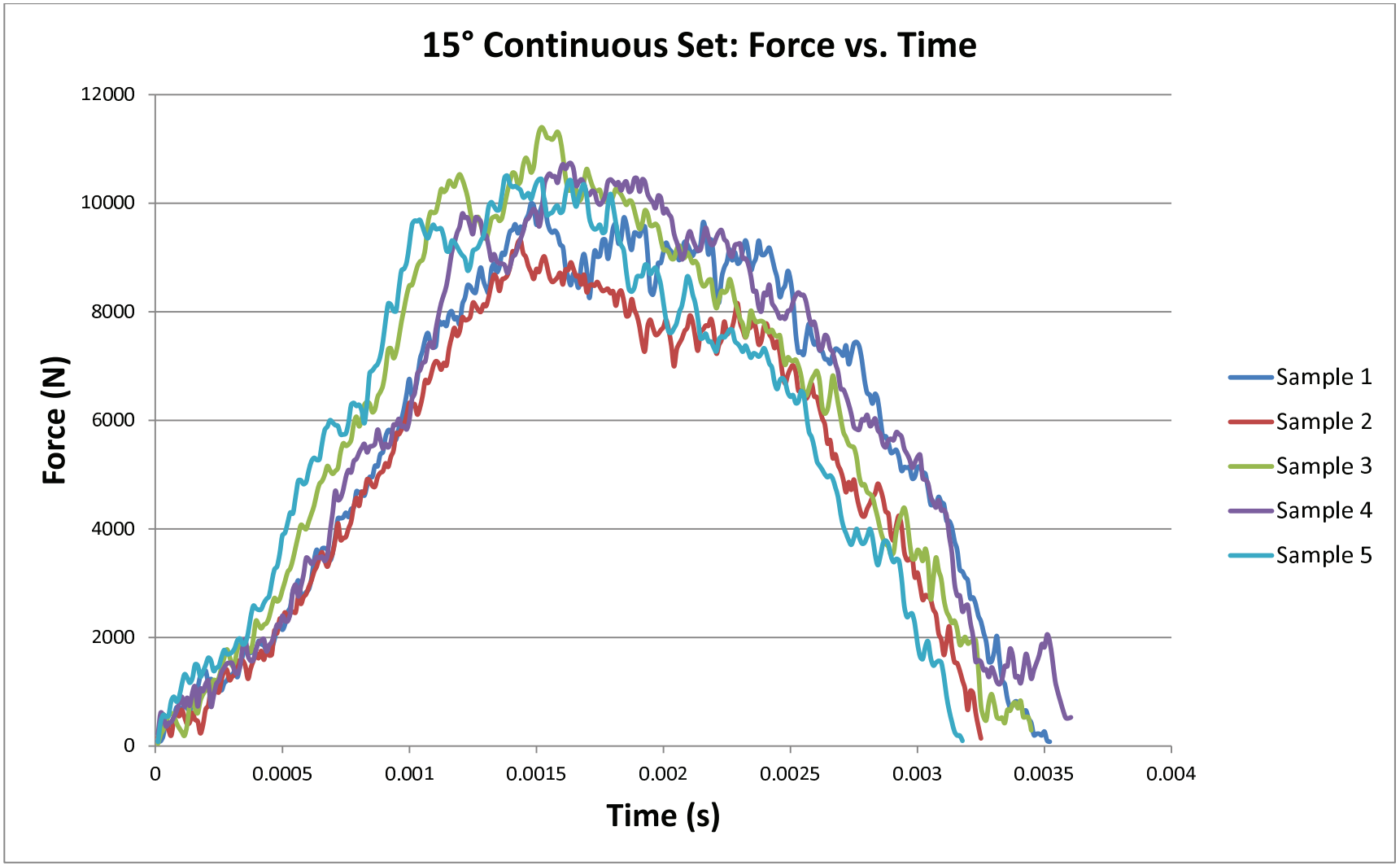

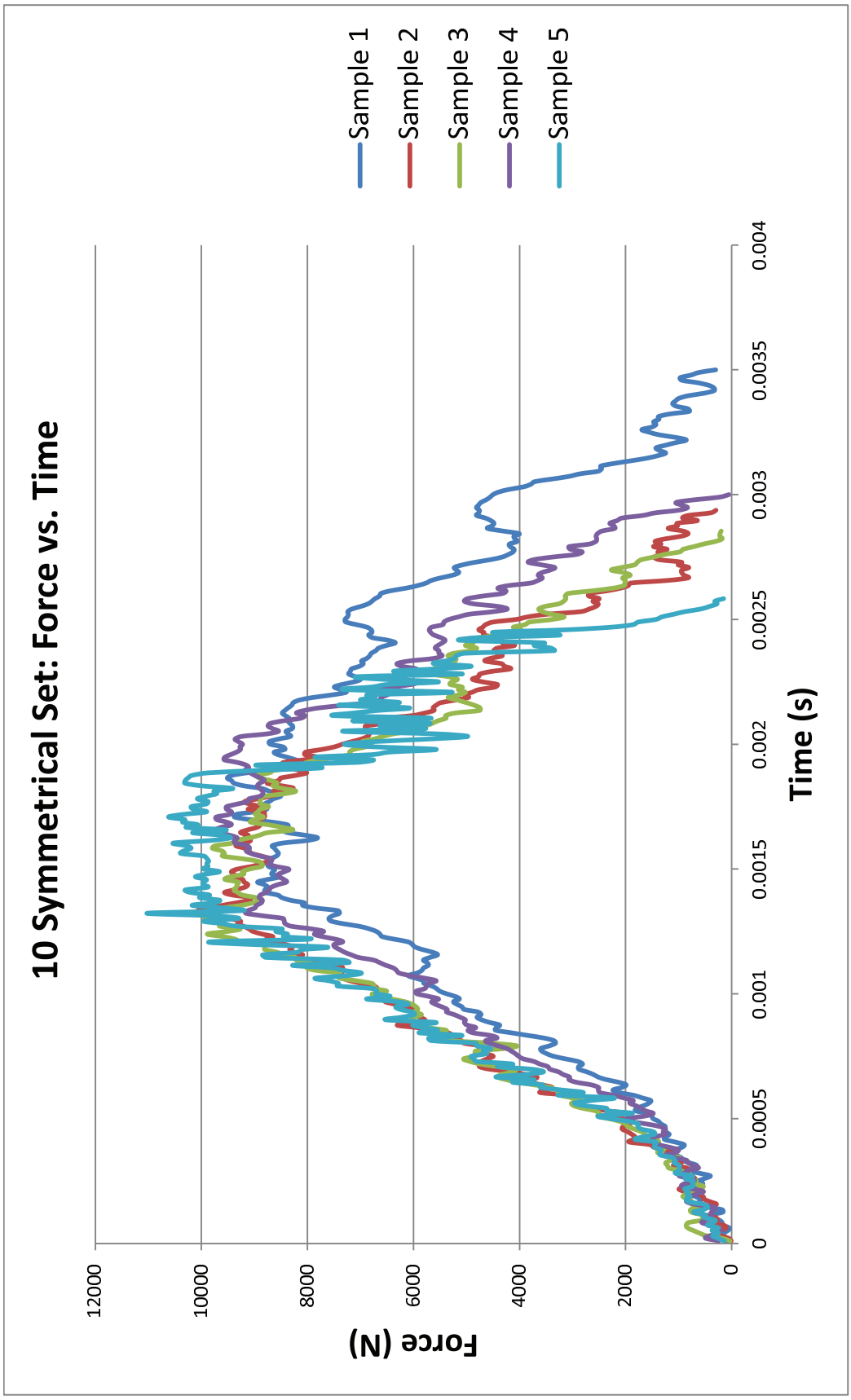

D.9: 10° Symmetrical Set

D.10: 10° Symmetrical Set

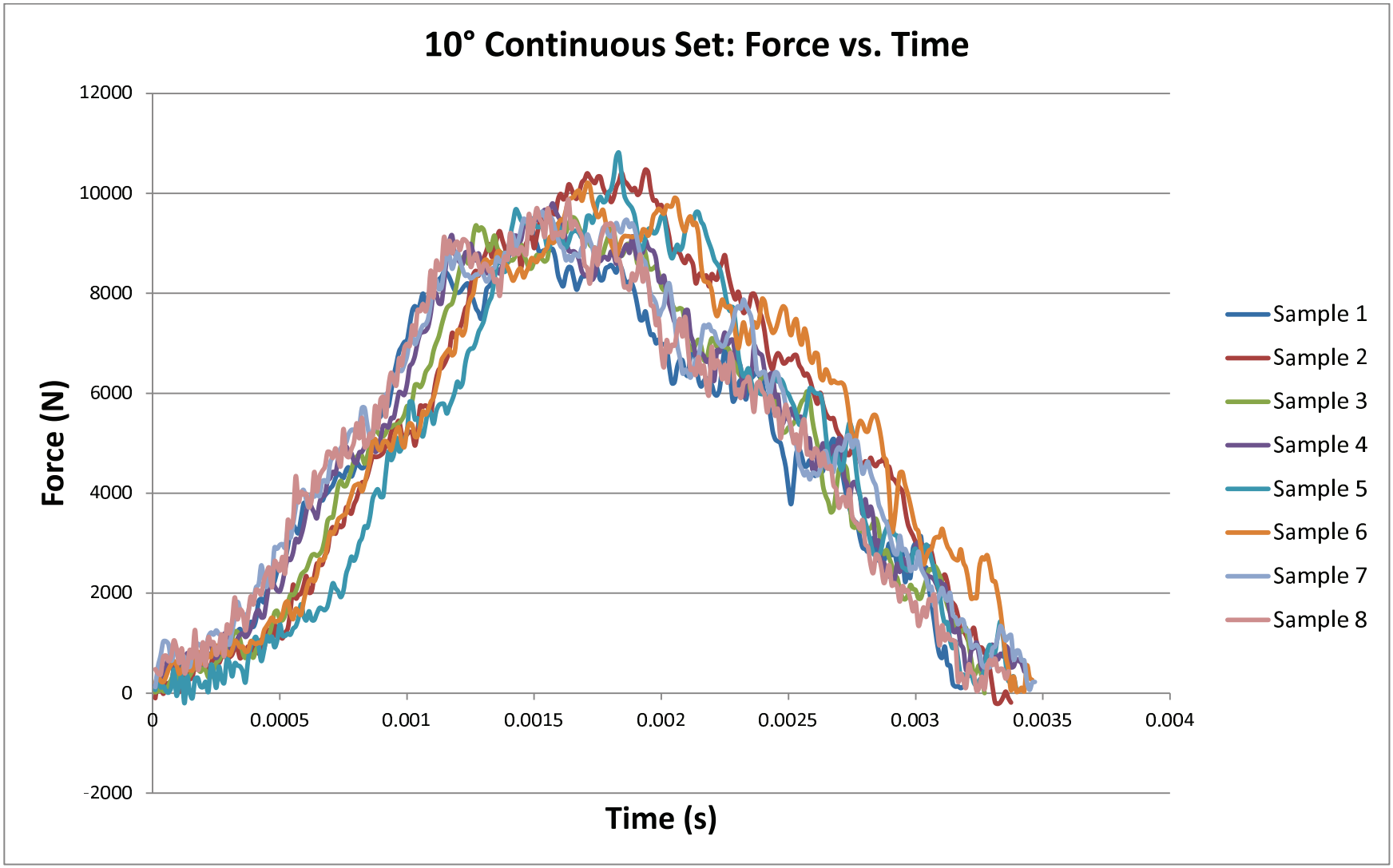

APPENDIX E: CT SCANS OF SAMPLES POST IMPACT

E.1: 45° Symmetrical Sample

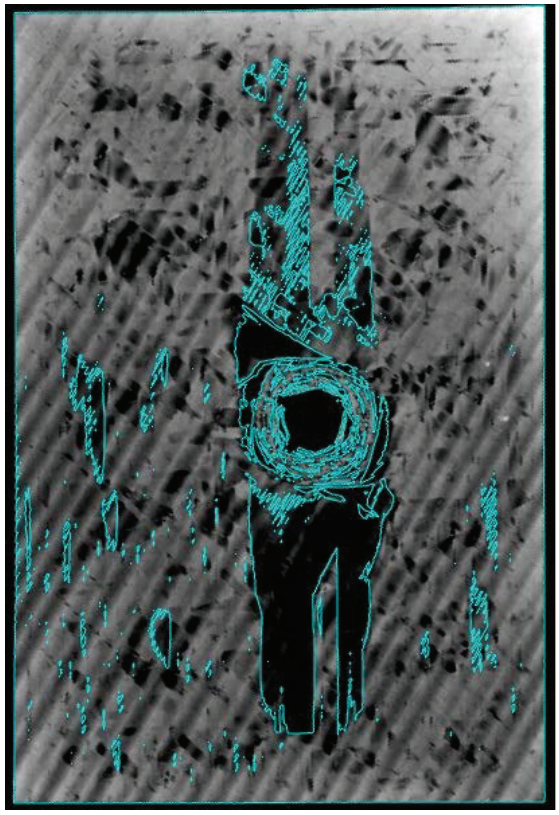

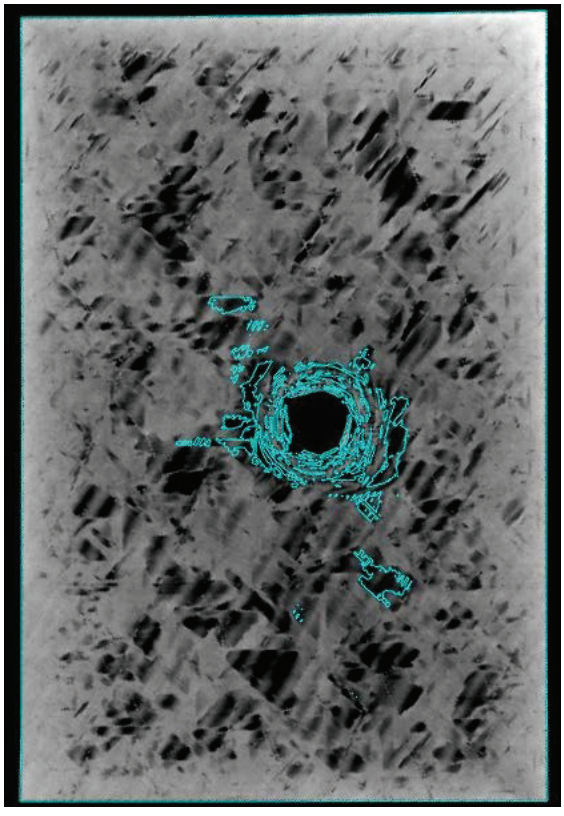

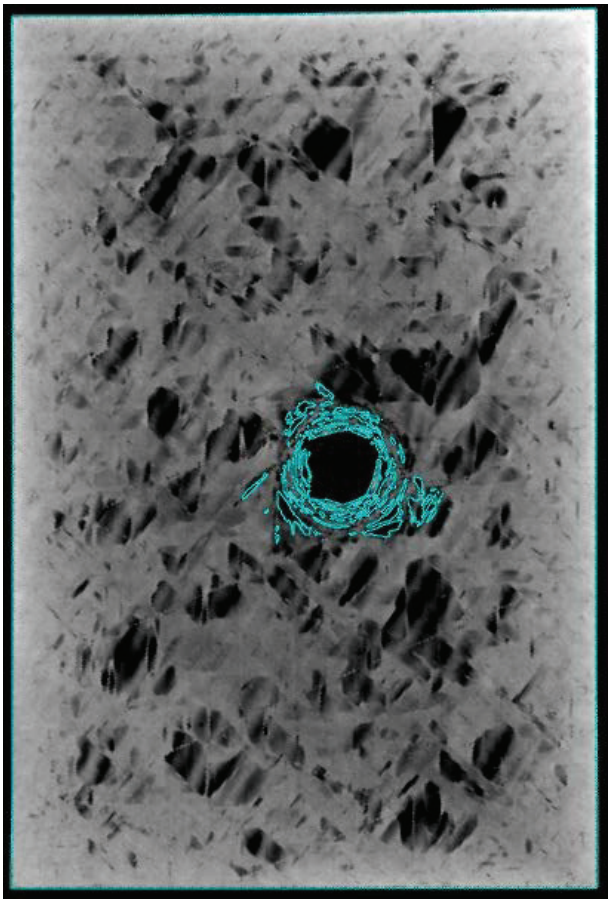

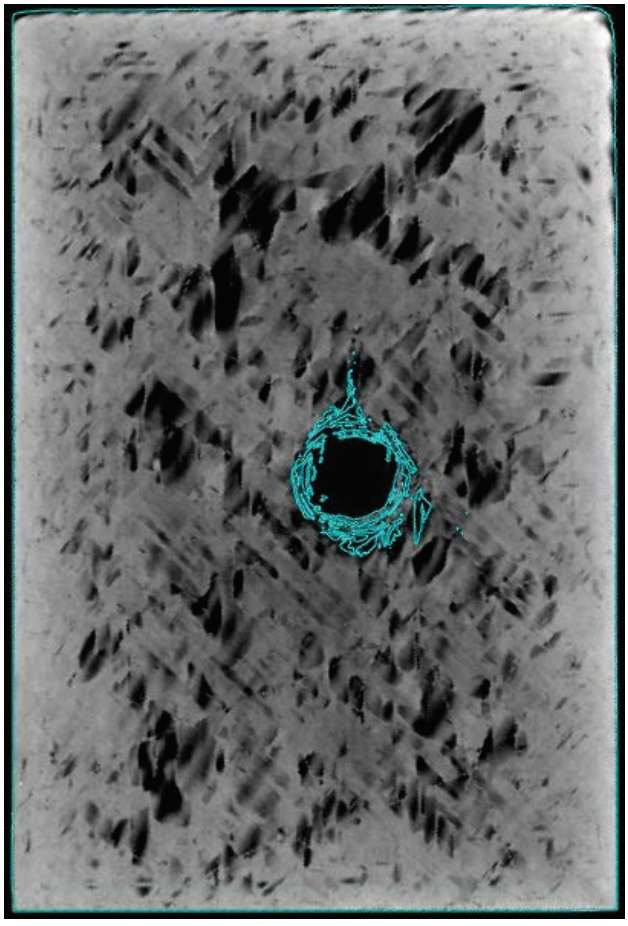

E.2: 30° Symmetrical Sample

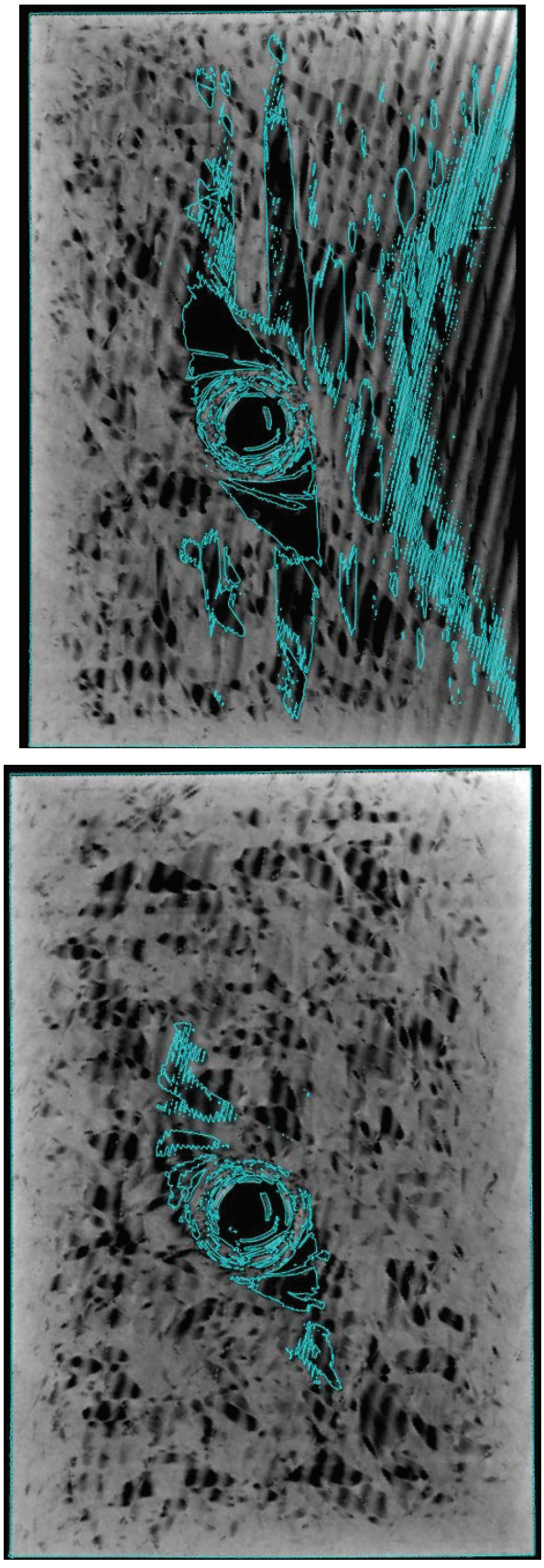

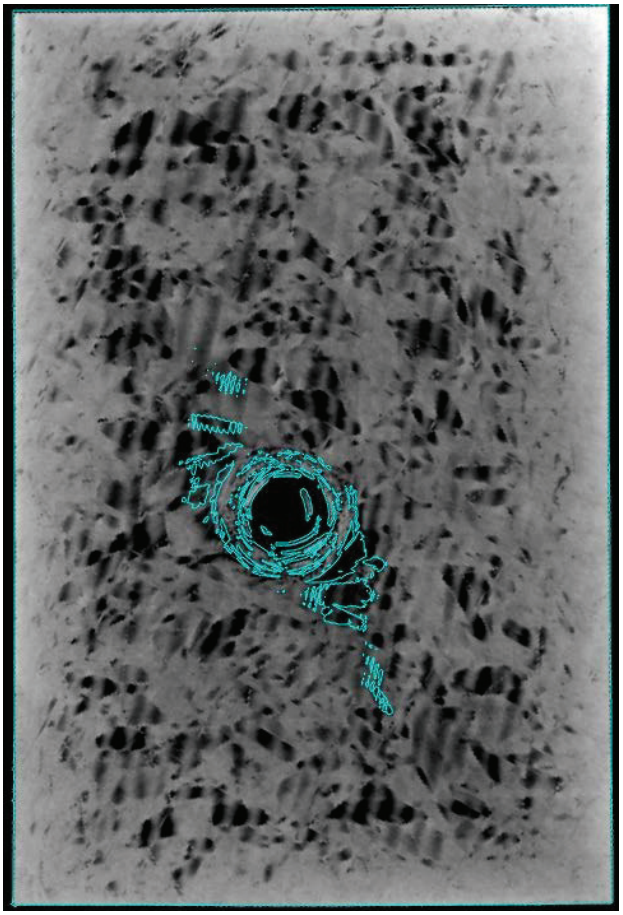

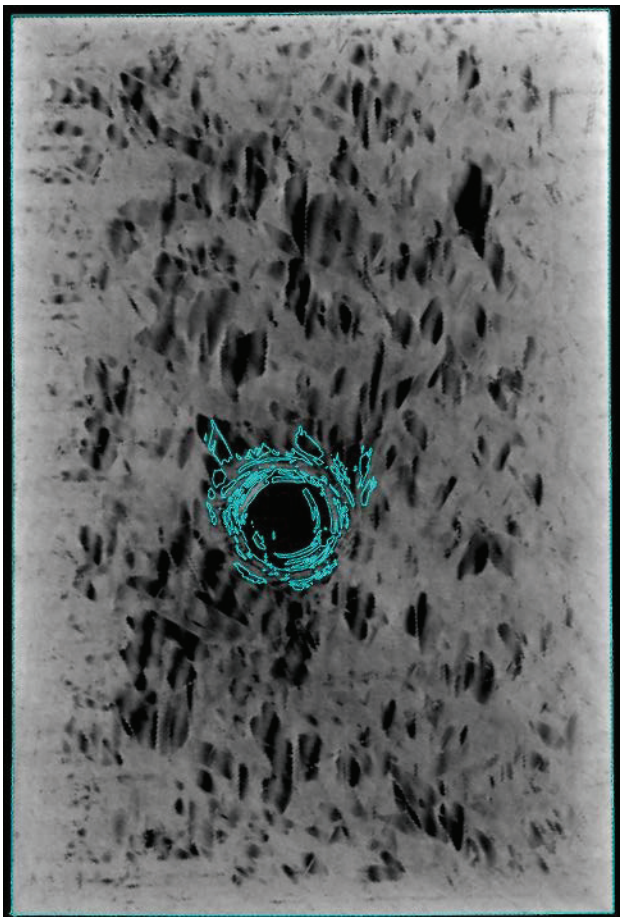

E.3: 15° Symmetrical Sample

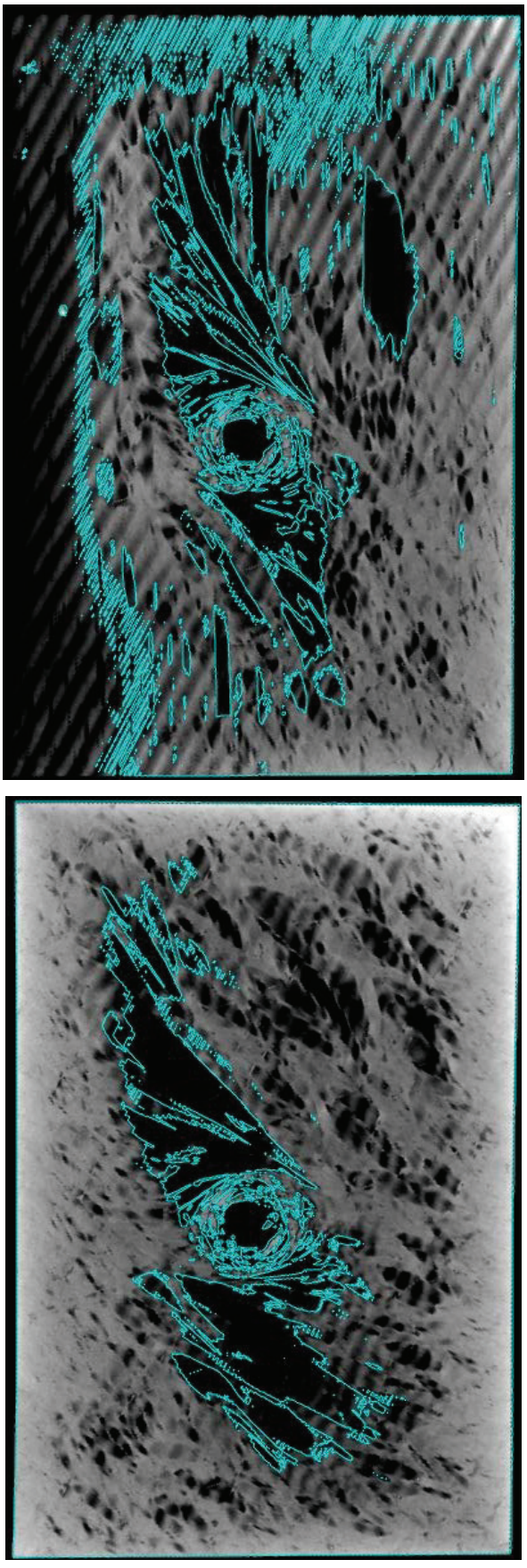

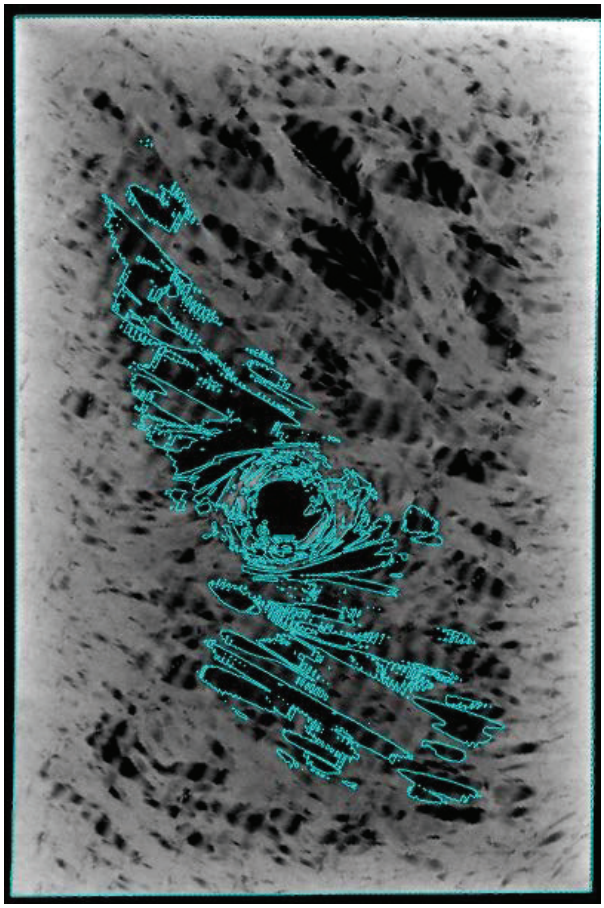

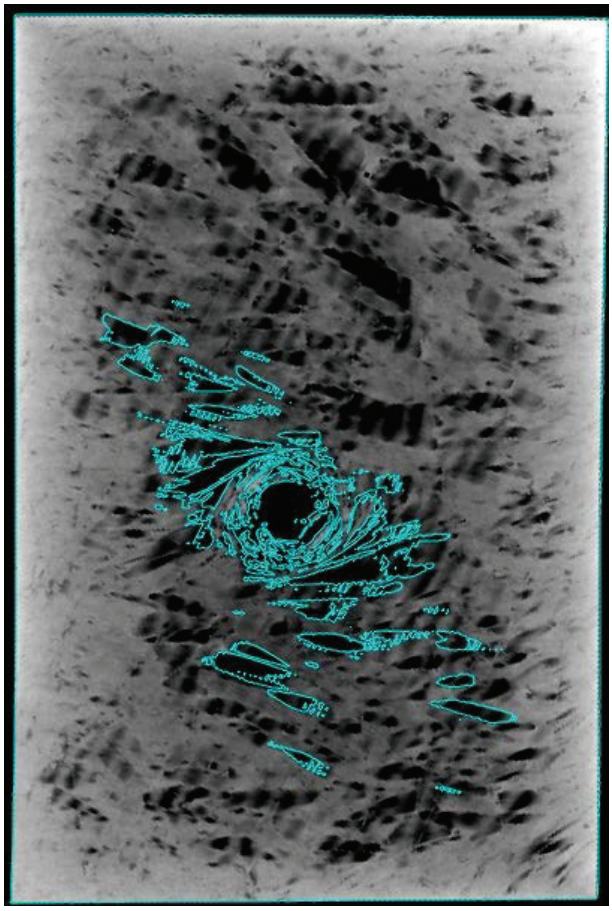

E.4: 15° Continuous Sample

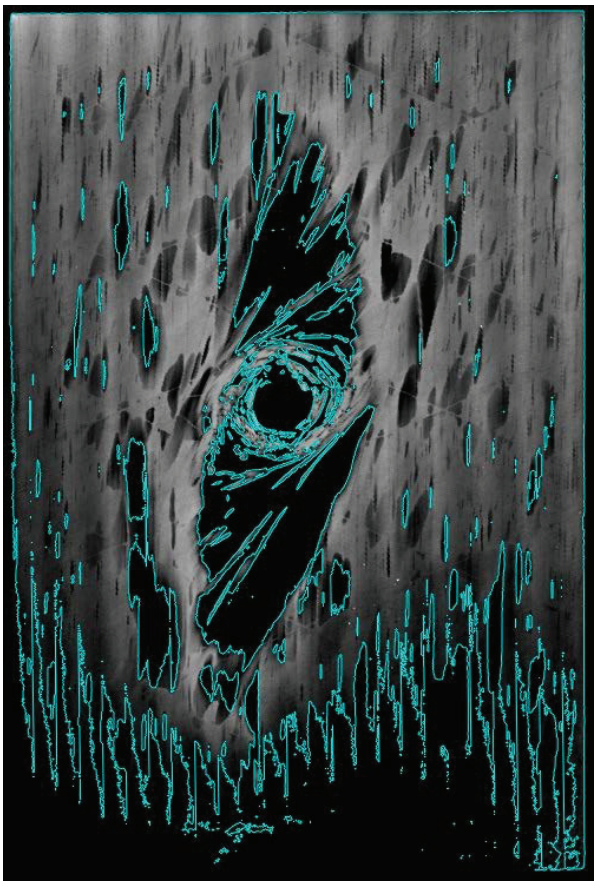

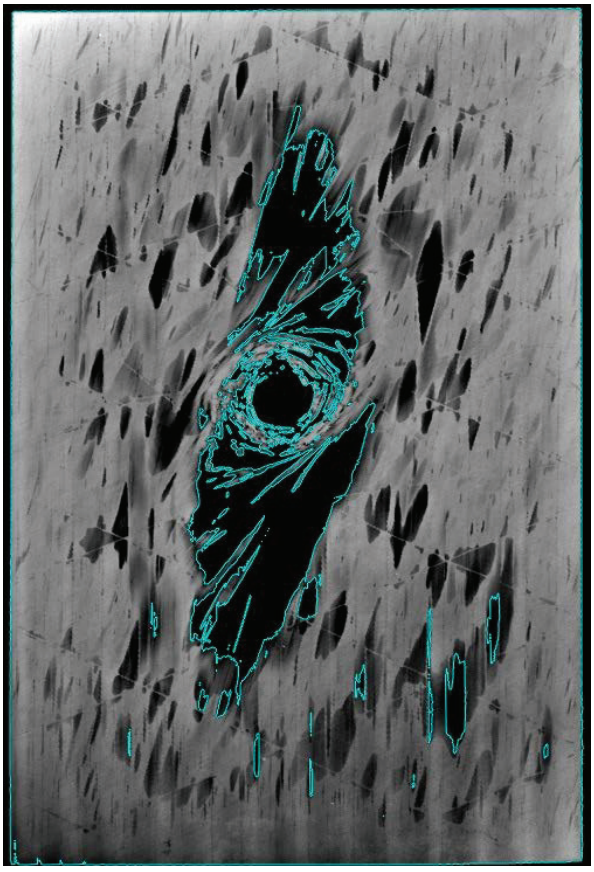

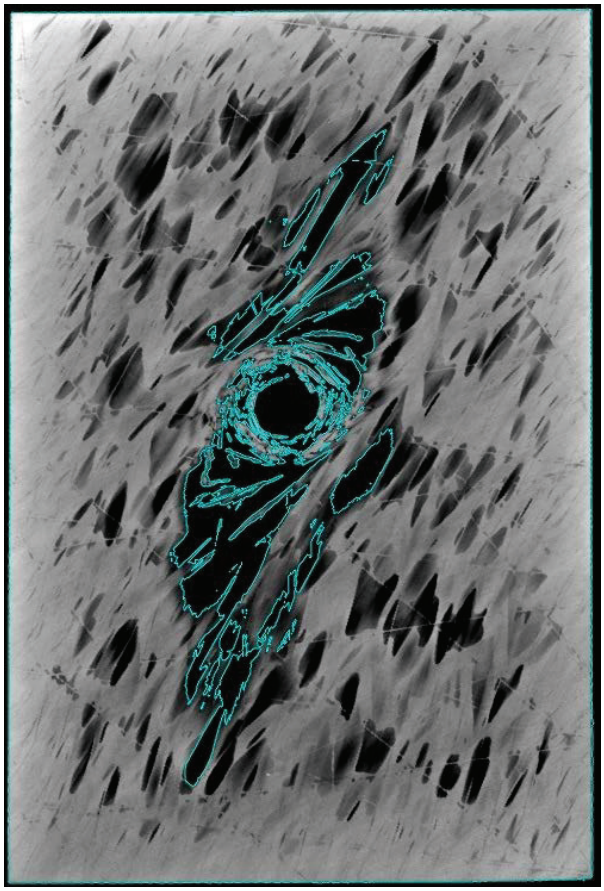

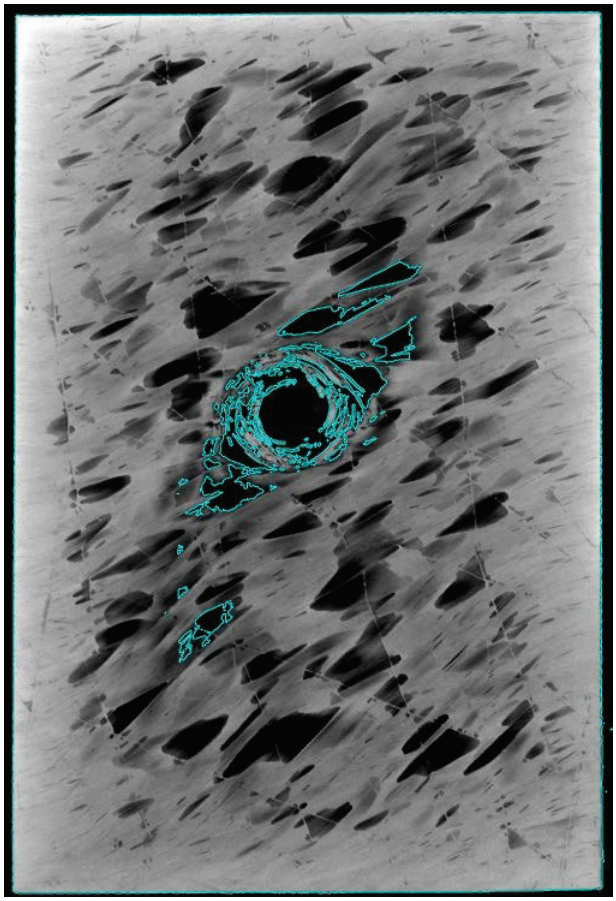

E.5: 10° Symmetrical Sample

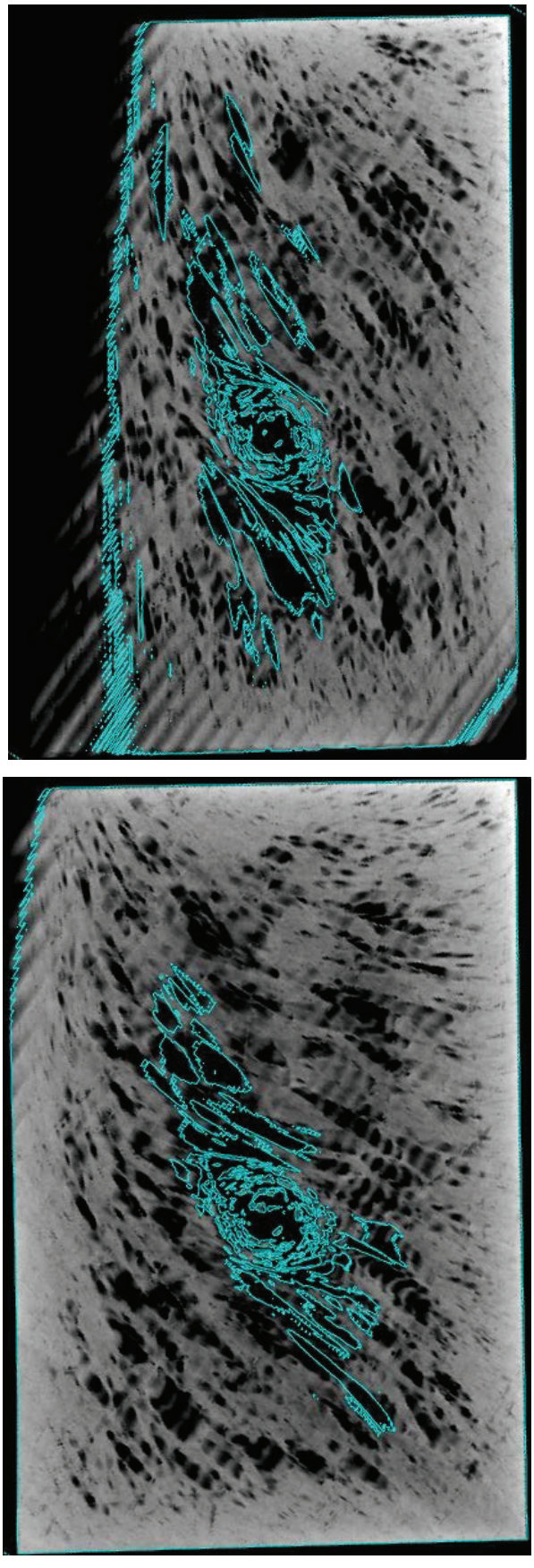

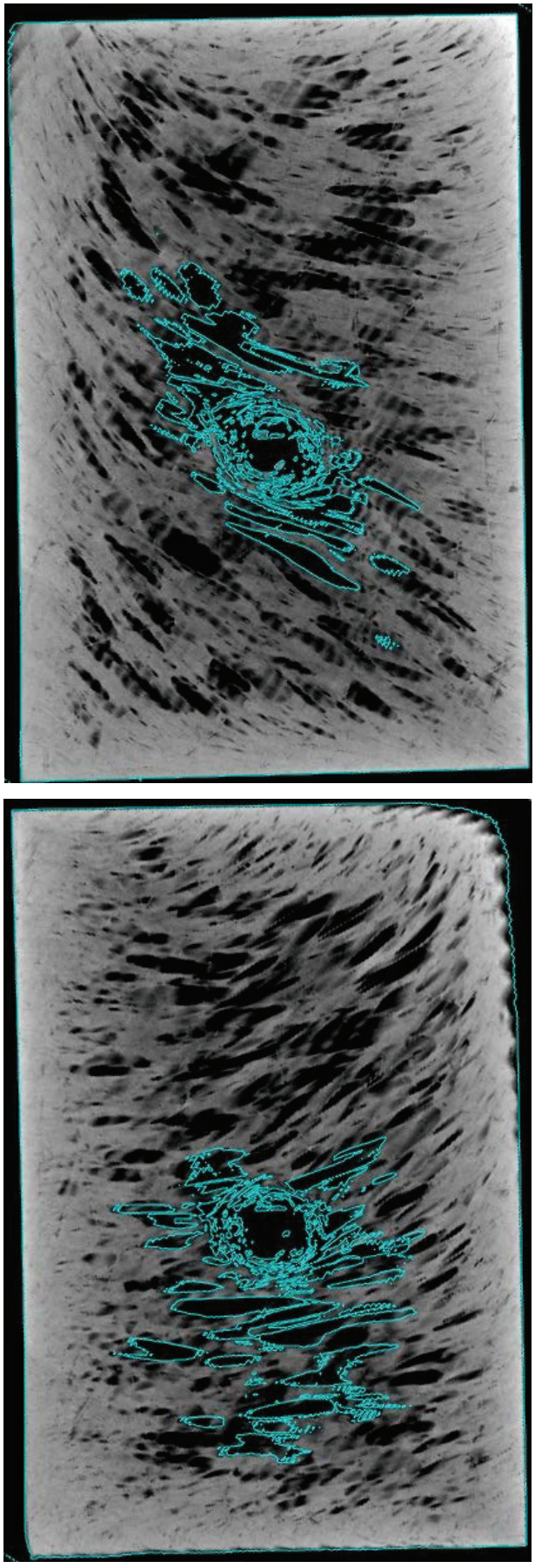

APPENDIX F: SIMULATION CROSS SECTIONS OF SAMPLES POST IMPACT

F.1: 90° Unidirectional Sample

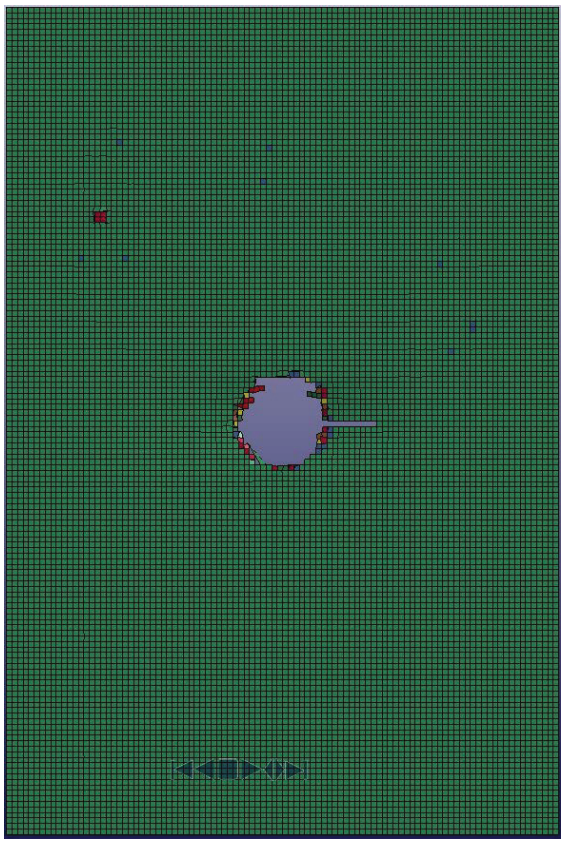

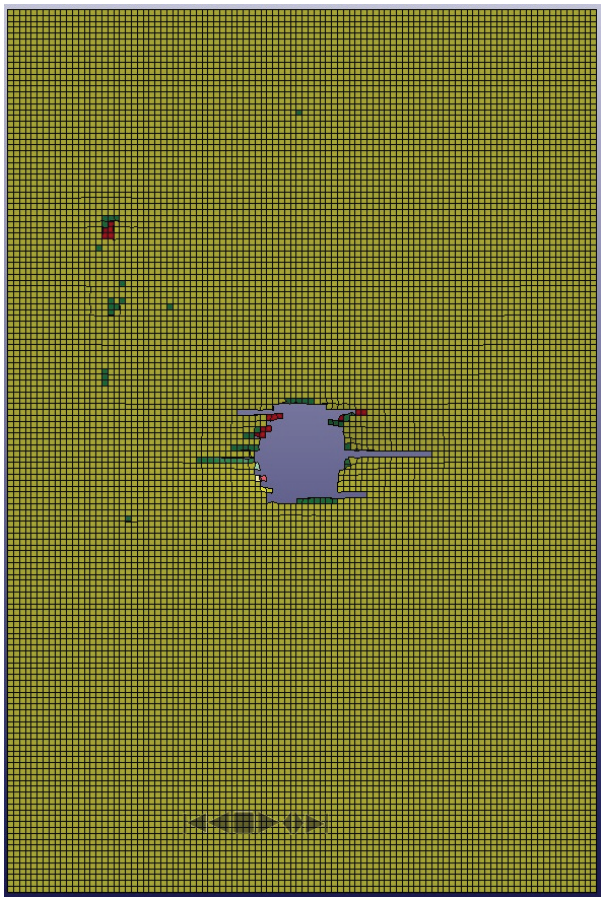

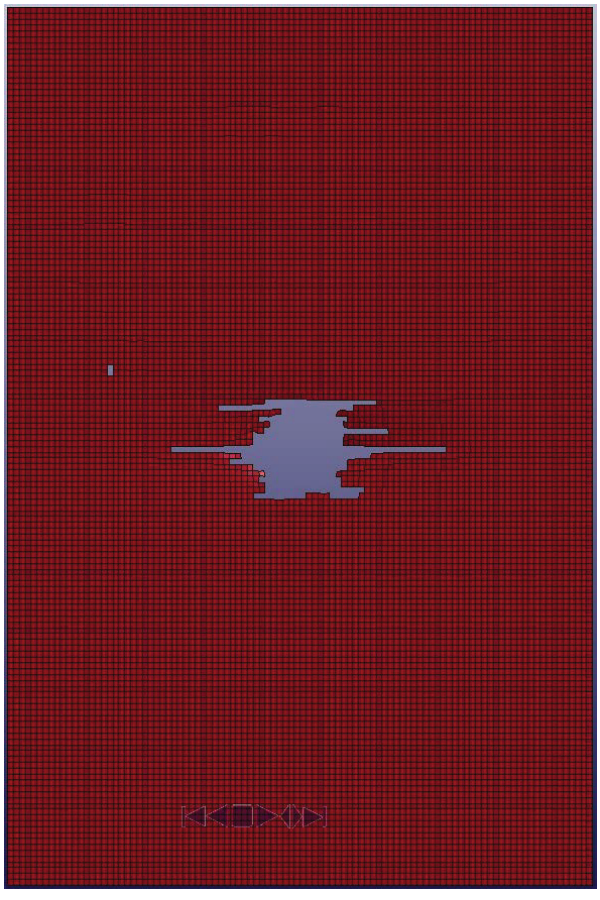

F.2: 0° Unidirectional Sample

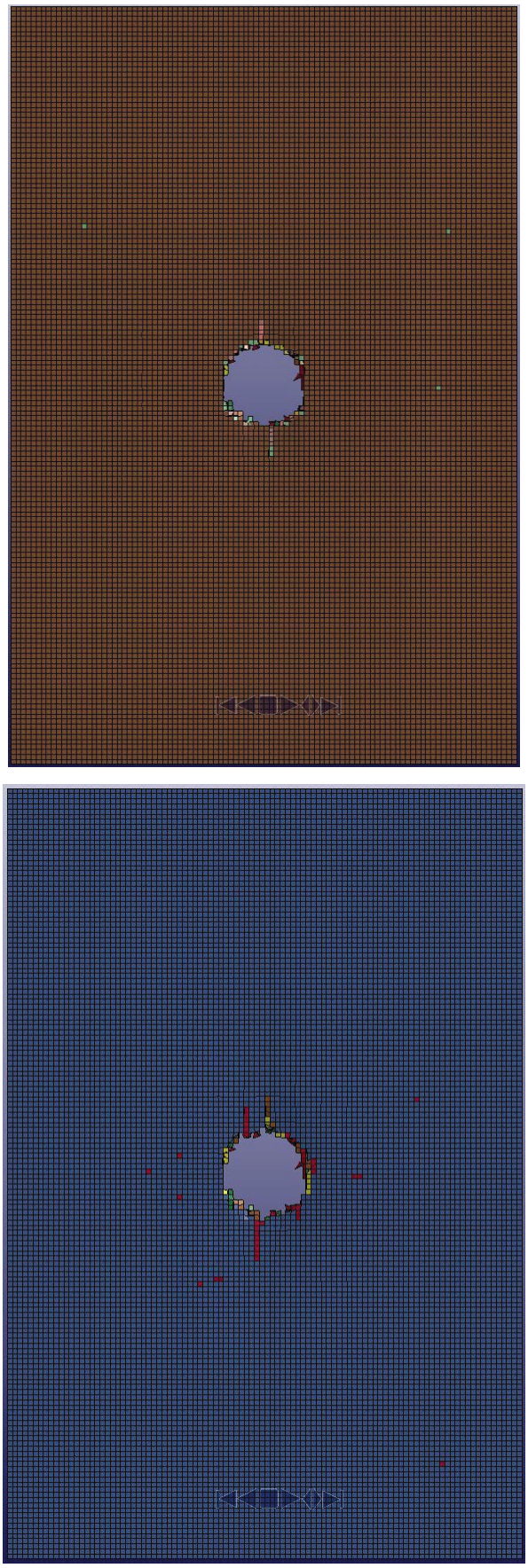

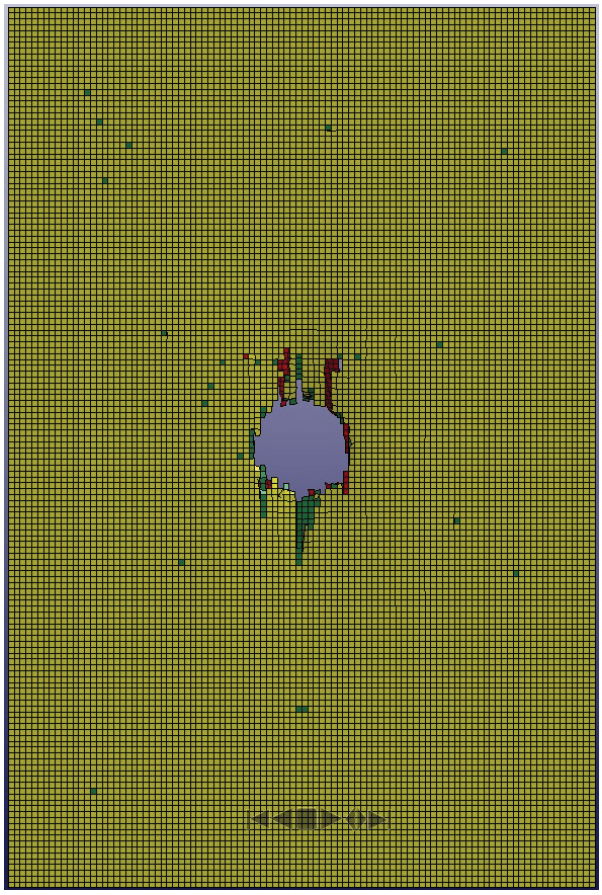

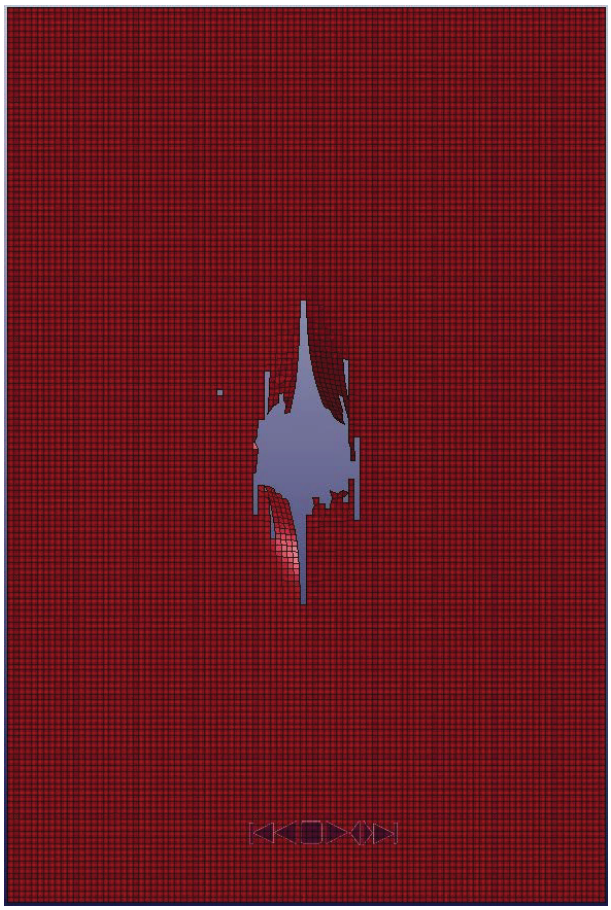

F.3: 45° Symmetrical Sample

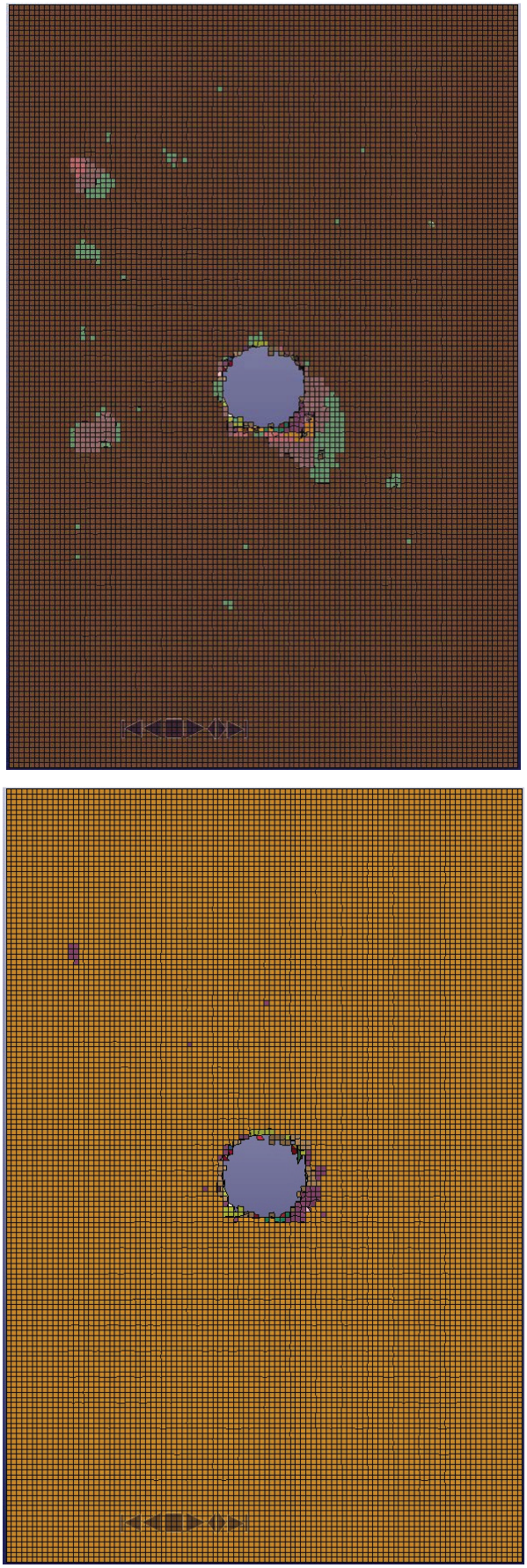

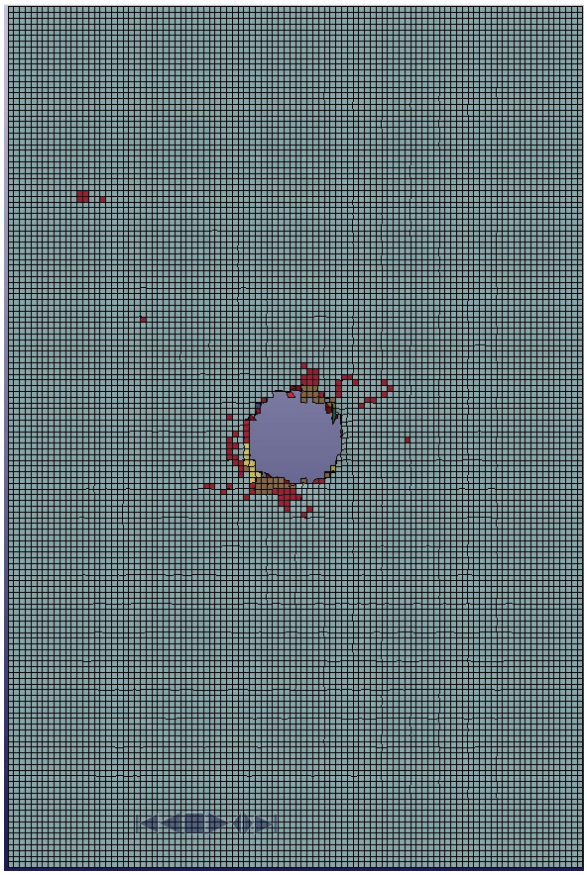

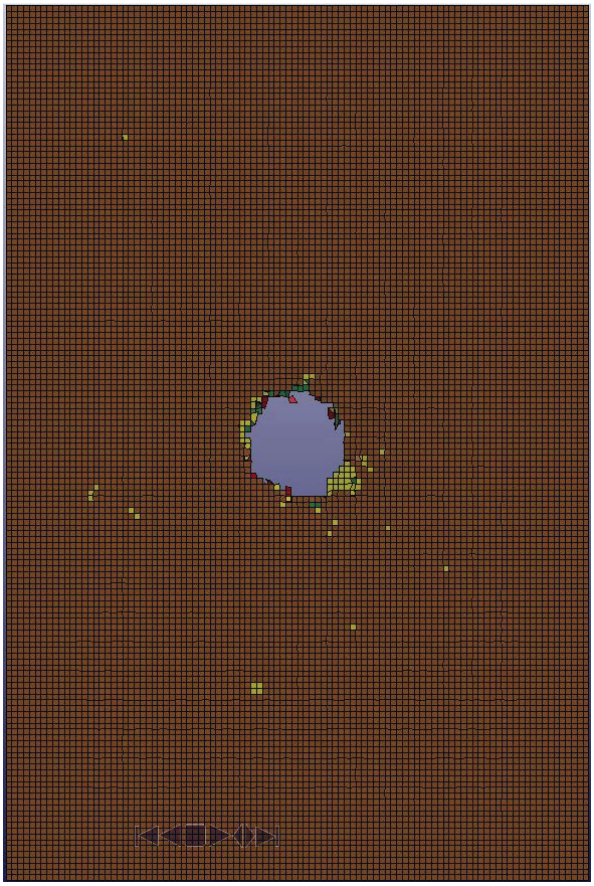

F.4: 45° Continuous Sample

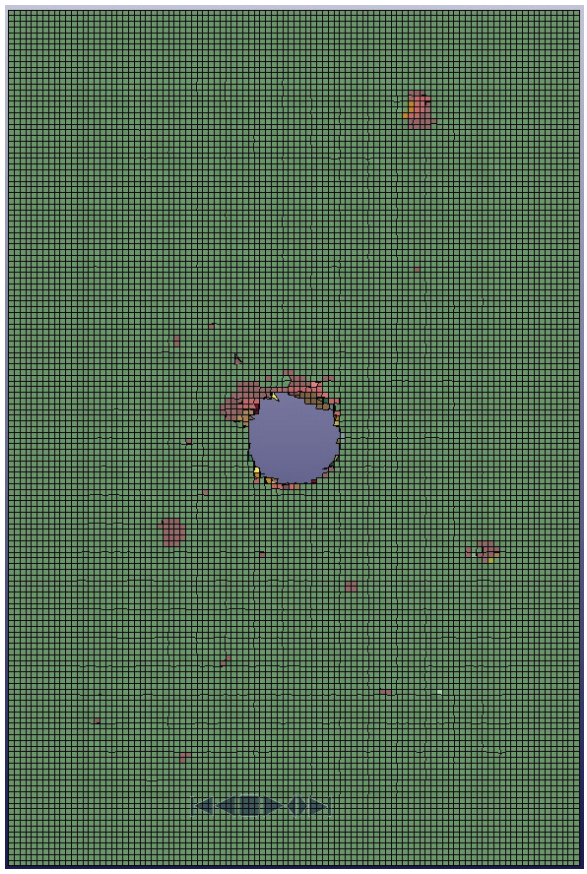

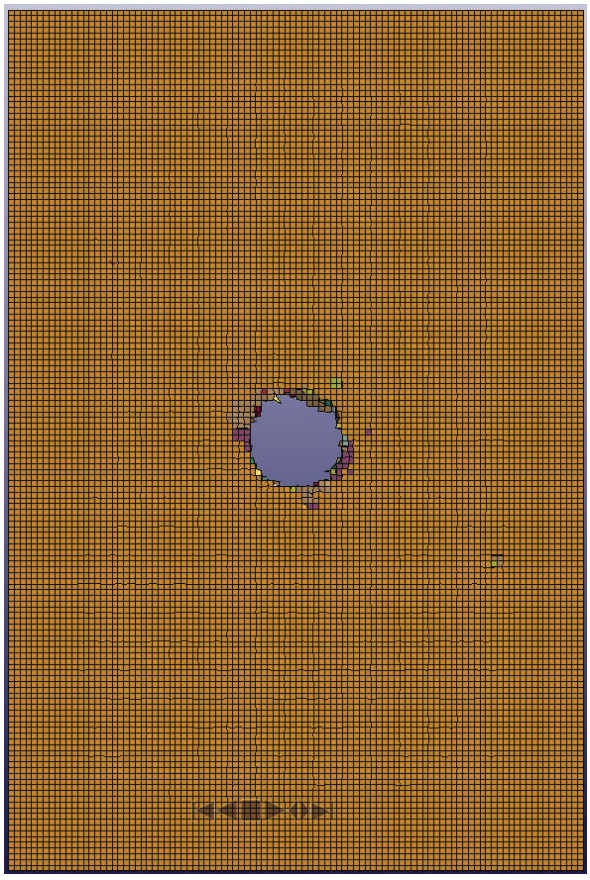

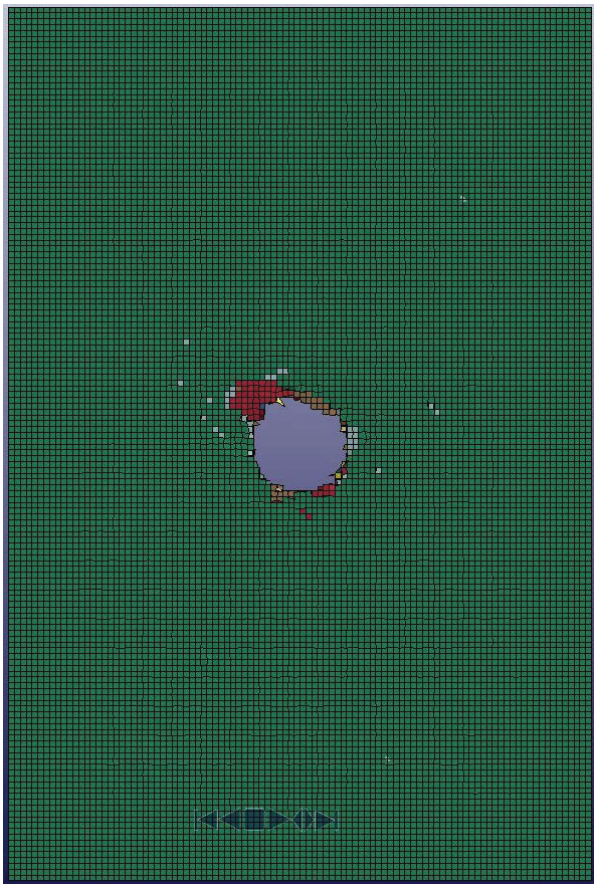

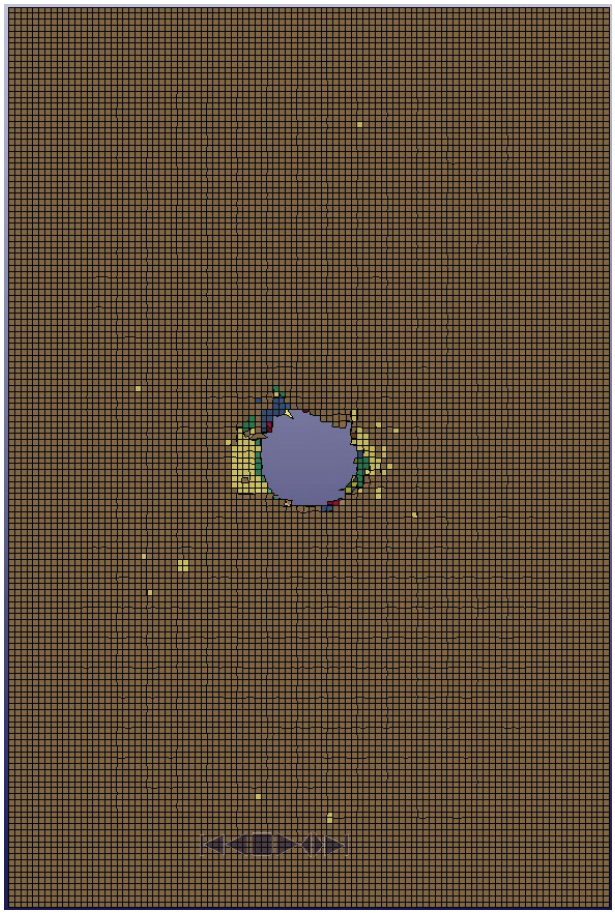

F.5: 30° Symmetrical Sample

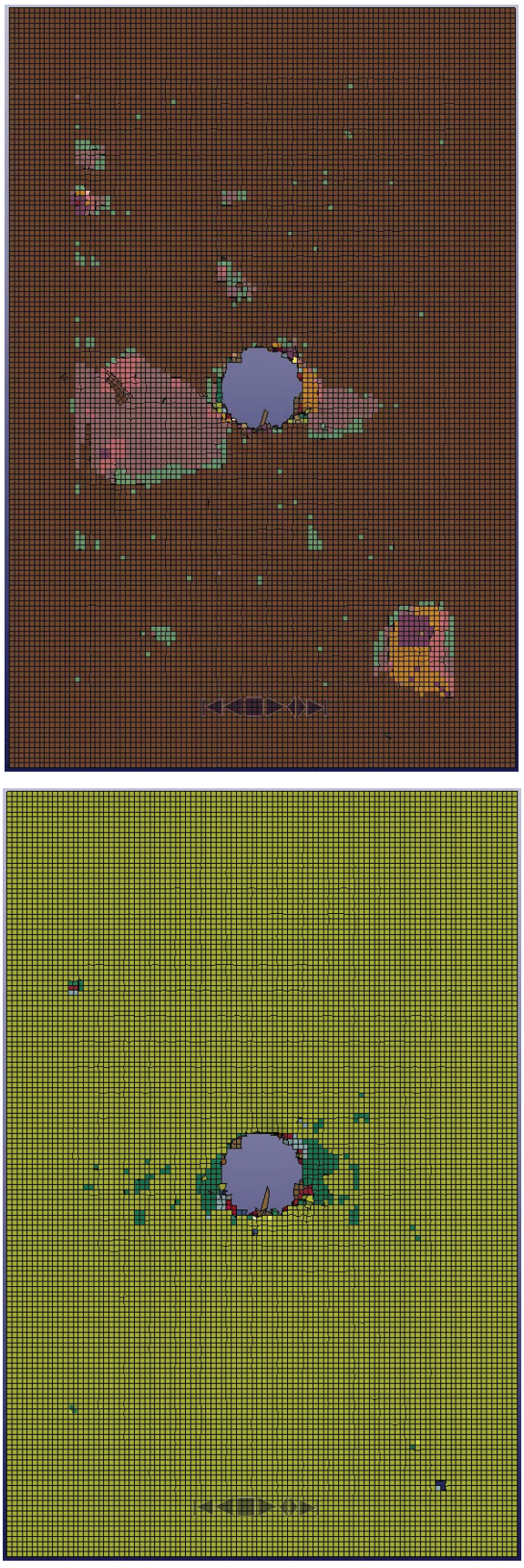

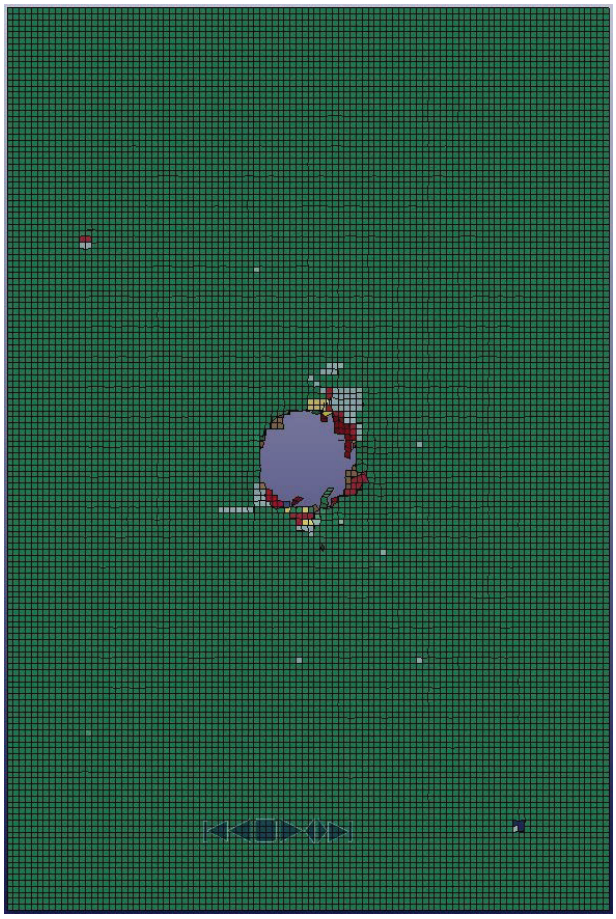

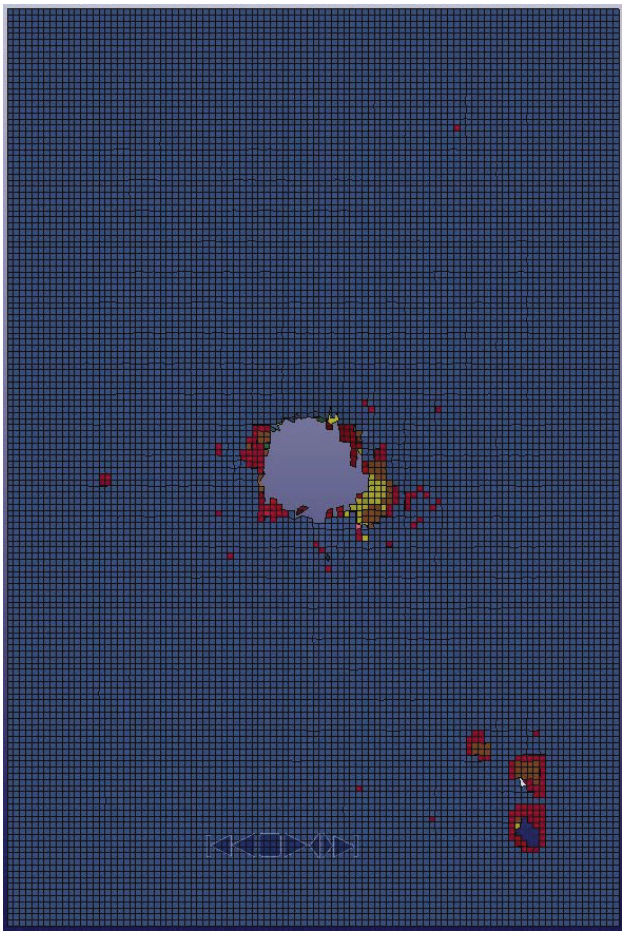

F.6: 30° Continuous Sample

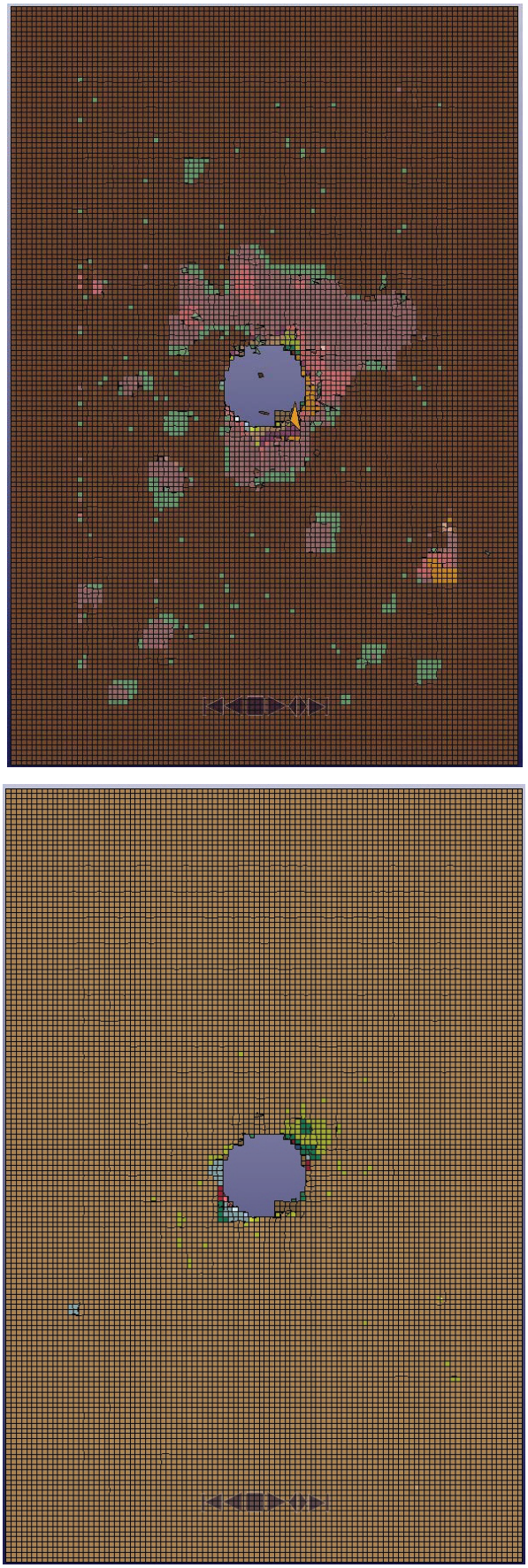

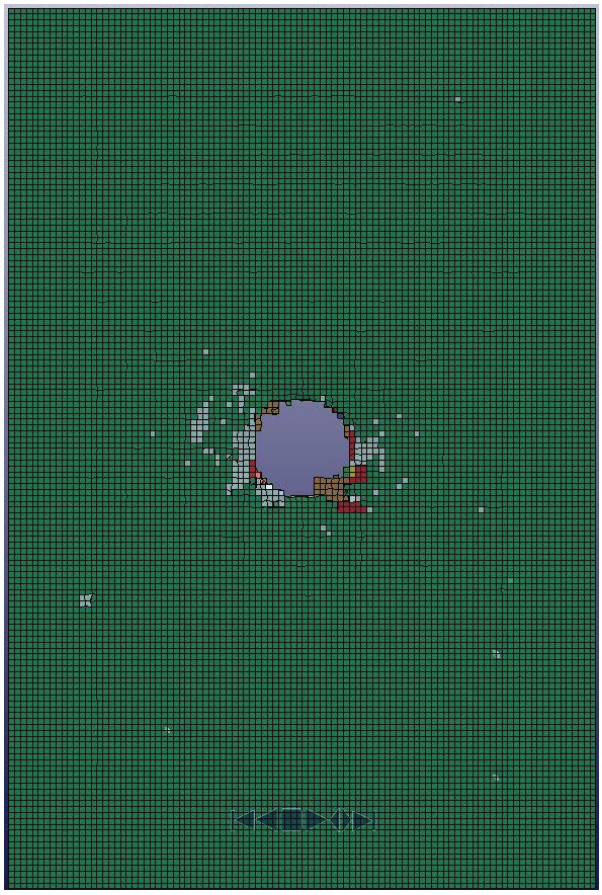

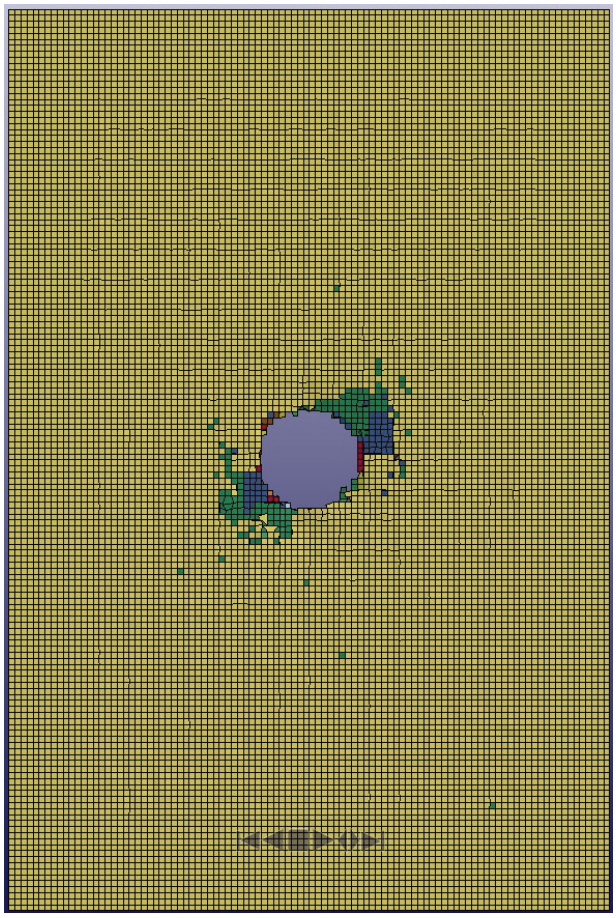

F.7: 15° Symmetrical Sample

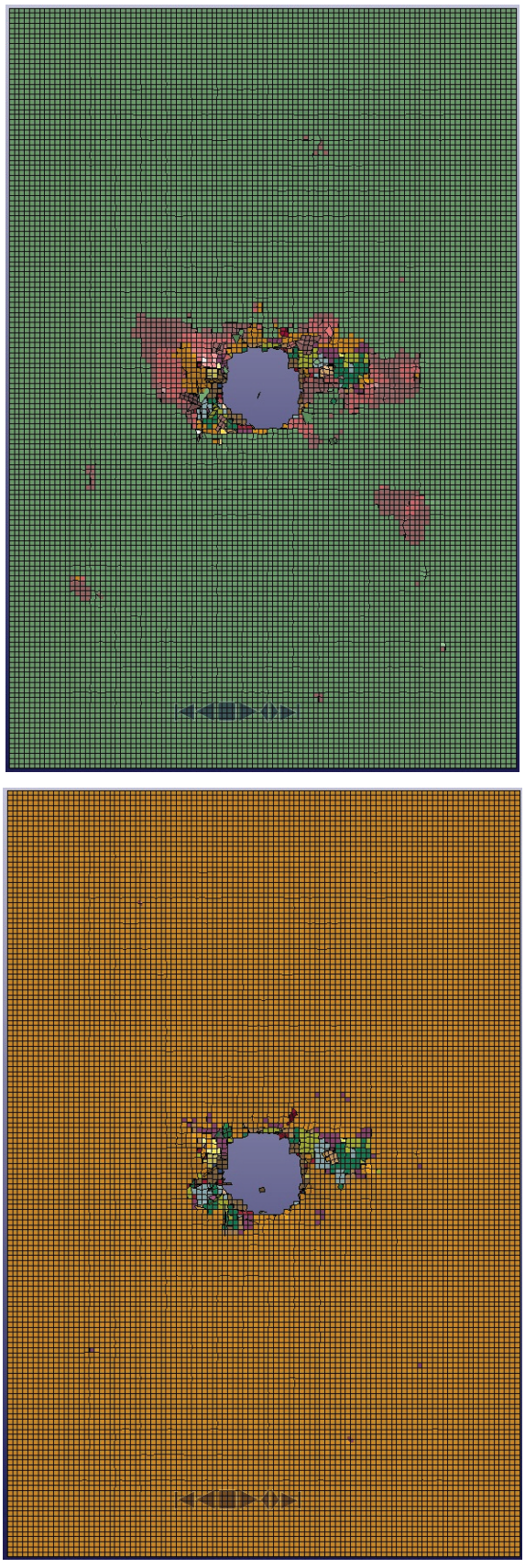

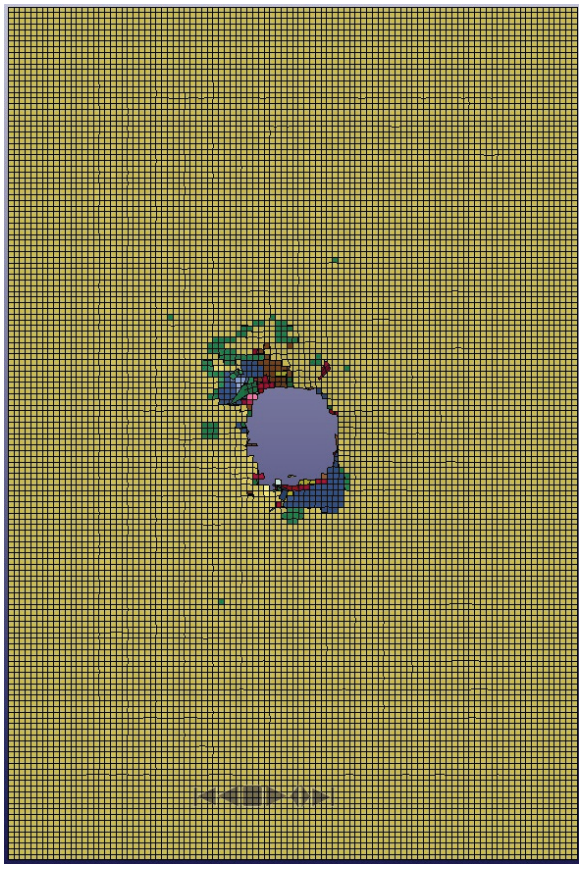

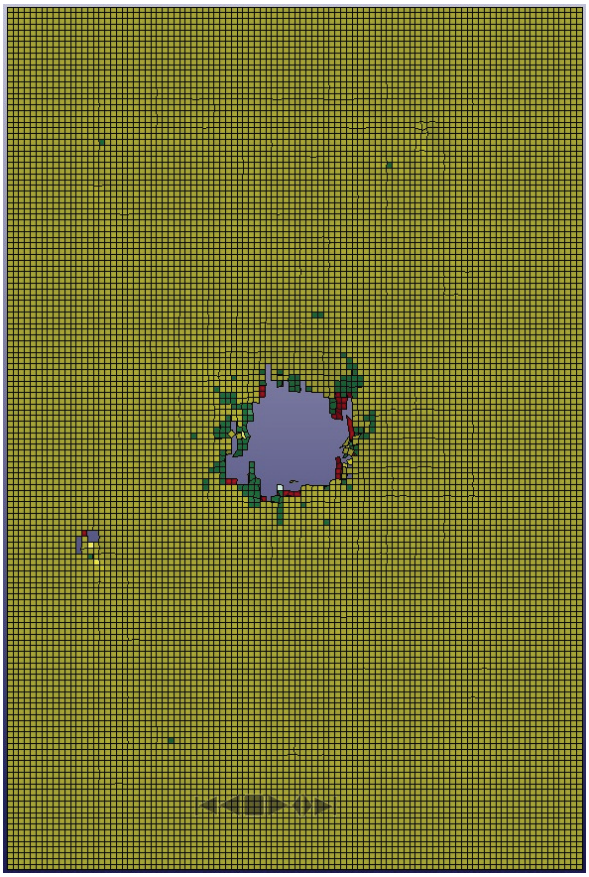

F.8: 15° Continuous Sample

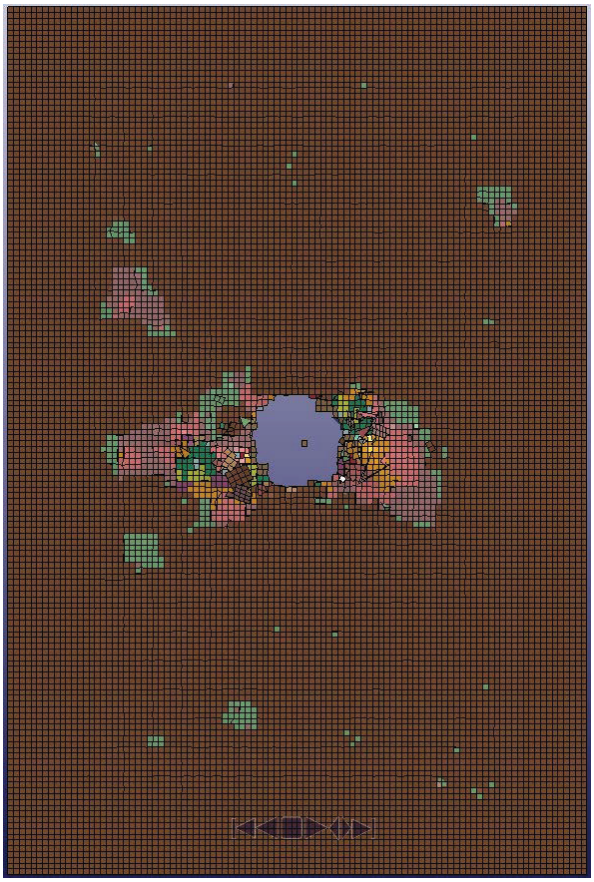

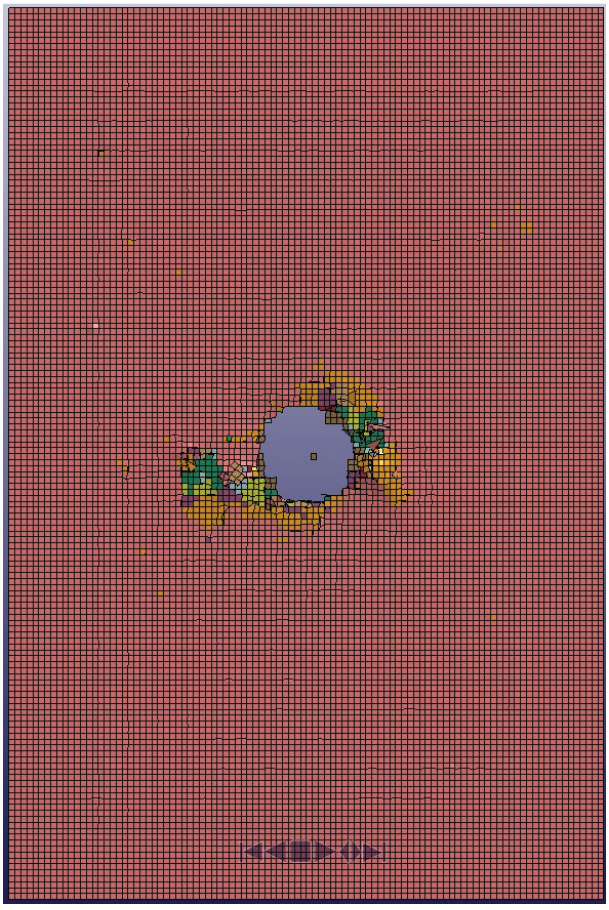

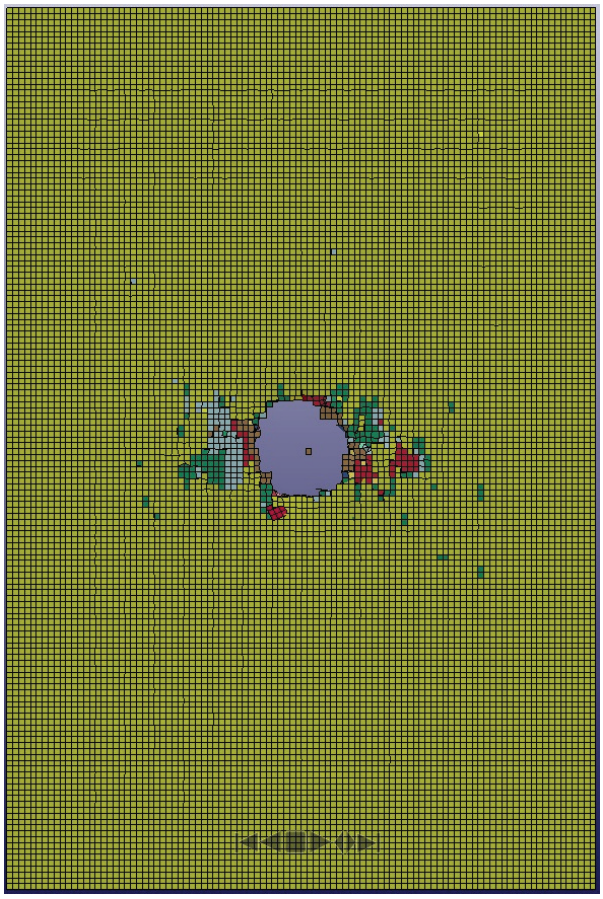

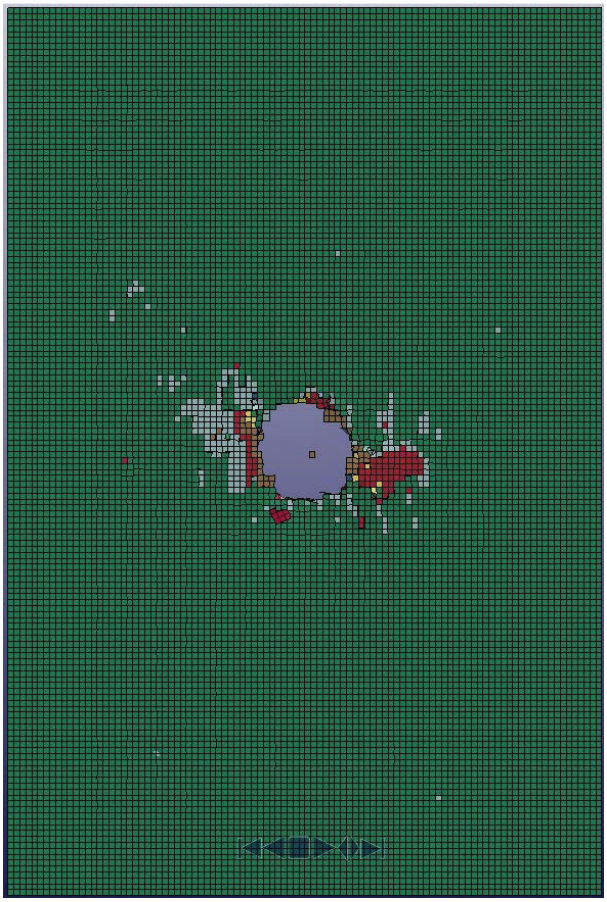

F.9: 10° Symmetrical Sample

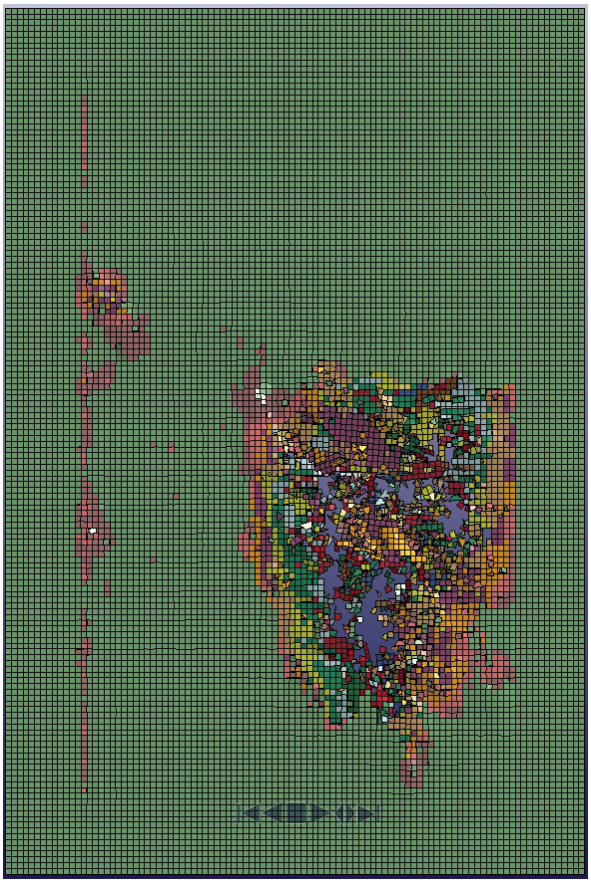

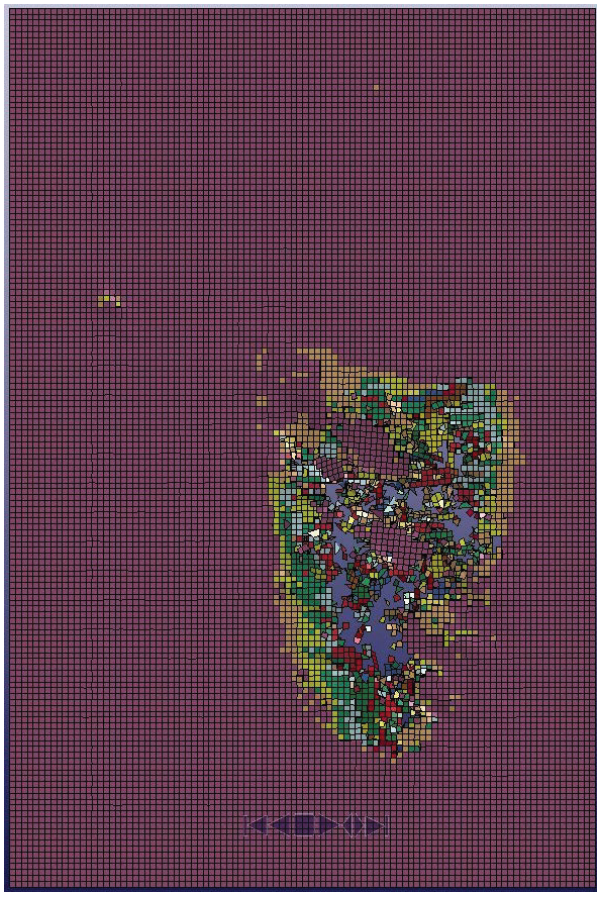

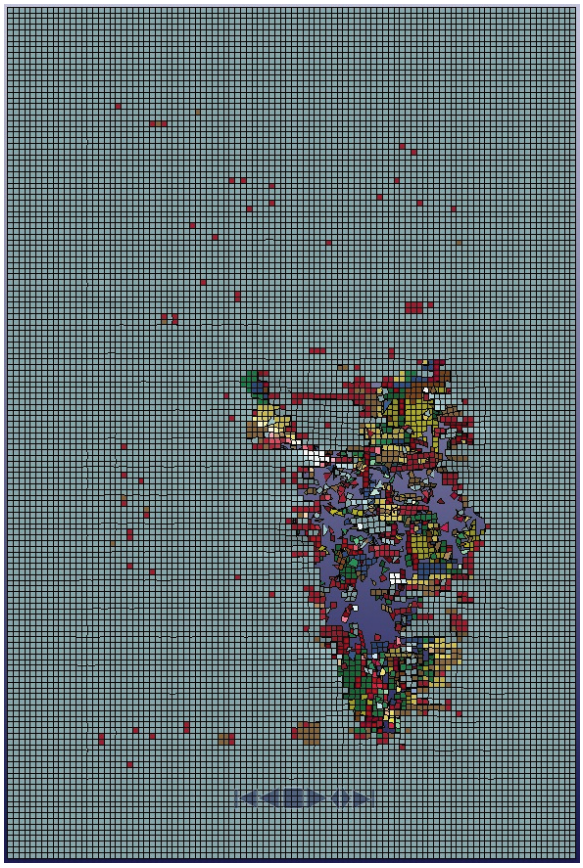

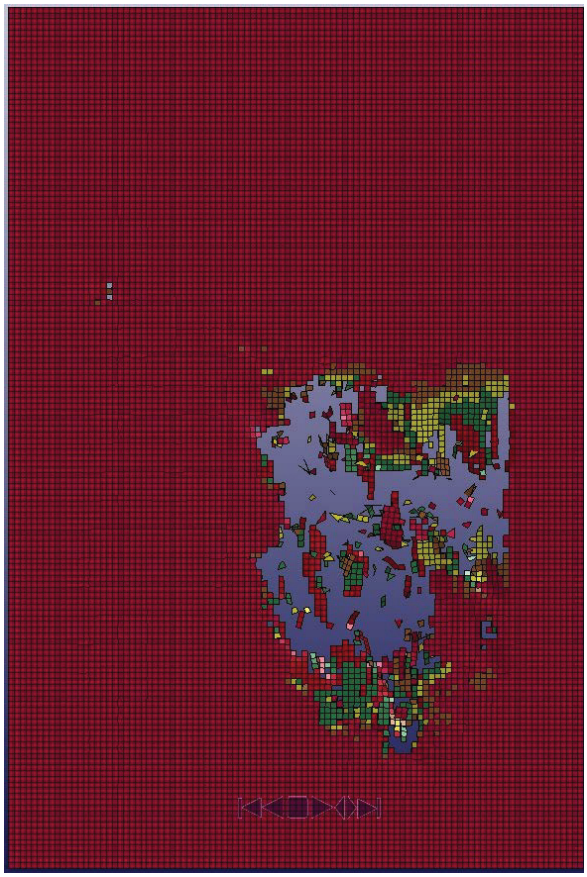

F.10: 10° Continuous Sample